Università degli Studi di Ferrara
Facoltà di Scienze Matematiche, Fisiche e Naturali
Corso di Dottorato di Ricerca in Fisica, XVIII Ciclo

# First Measurement of the Spin - Exchange collision cross section in the low Temperature Region

Tutore Interno:

Prof. PAOLA FERRETTI DAL PIAZ

Dottorando:

MARCO CAPILUPPI

Tutore Esterno:

Dr. PAOLO LENISA

Anni 2003-2005

# Contents

# Introduction

Since 1995 the HERMES experiment has been running in the HERA storage ring, at DESY Hamburg, mainly devoted to the study of the spin structure of the nucleon. At HERMES deep inelastic scattering events are produced by exploiting the 27.5 GeV electron/positron beam in combination with an internal polarized gas target. Thanks to the Sokolov-Ternov mechanism [14], the HERA beam is characterized by a self polarization, transverse to its momentum, which is turned to longitudinal at the HERMES interaction point by the employment of two spin rotators. Beside the identification of the inclusive events, the HERMES spectrometer, furnished with a dual radiator RICH detector, is capable of distinguish between pions, kaons and protons, thus allowing the semi-inclusive analysis.

Since 1996 HERMES has employed a polarized hydrogen/deuterium gas target, whose spin orientation, defined by the application of an external magnetic field, was kept longitudinal to the beam momentum till the end of 2000 and switched to transverse in 2001. In November 2005 the target has been finally removed to allow the installation of a large acceptance detector (RECOIL). The HERMES target employs a beam of nuclear polarized atoms produced by an atomic beam source which is injected into the center of the thin-walled storage cell via a side tube and the atoms then diffuse to the open ends of the cell where they are removed by a high speed pumping system. A second side tube is provided to sample the gas within the target cell. The beam emerging from this tube is analyzed with a Target Gas Analyzer (TGA) to determine its atomic fraction and a Breit - Rabi polarimeter (BRP) in order to calculate the atomic polarization.

During the two years that I spent at DESY I was responsible for the Breit - Rabi polarimeter and of the Target Gas Analyzer. I worked both on the hardware components and on the analysis of the data of the target polarization.

This thesis is divided into parts: the first one (chapter 1 - 5) is devoted to the description of the overall performance of the target and analysis of the polarization data. As this work is supposed to be the last thesis on the polarized target in HERMES, I took the chance to present not only the data for the last year but also all the data collected in the previous years to give an overall view of the target performance.

The second part of this thesis (chapter 6) is devoted to the original measurement done with the HERMES target of the value of the spin - exchange cross section in the low temperature region (40 - 100 K). This measurement, of interest in astrophysics, represents the first measurement at all in this temperature region and has been performed in between the normal runs of data taking for the HERMES experiment. It involved a complete understanding of the target and its systematics and basically summaries the knowledge acquired in many years of running.

A detailed description of each chapter is reported in the following:

- **chapter 1** is devoted to the experimental setup. A detailed description of the two detectors involved in the polarization measurement (TGA and BRP) is given;
- in **chapter 2** the treatment of the signals collected by TGA and BRP is presented;
- the **chapter 3** describes the physical fenomena happening inside the target cell as depolarization and recombination;
- in **chapter 4** the approach for the calculation of the target polarization is presented;
- **chapter 5** presents an overall summary of the performance of the HERMES target;
- in **chapter 6** the spin - exchange cross section measurement is explained in detail, and the final results for the cross section are given;
- in the **appendix** the hyperfine structure of hydrogen and deuterium as a way to understand the working principle of the HERMES target is presented.

# Chapter 1

# Experimental setup

The HERMES polarized hydrogen and deuterium target, schematically shown in fig. 1.1, consists of an atomic beam source (ABS), which injects a spin polarized beam of H or D atoms into a thin walled storage cell. A sample of gas diffuses from the middle of the cell into a Breit Rabi Polarimeter (BRP), which measures the atomic polarization, or into a Target Gas Analyzer (TGA), which measures the relative atomic and molecular content of the gas. A magnet surrounding the storage cell provides a holding field defining the polarization axis and preventing spin relaxation by effectively decoupling the magnetic moments of electrons and nucleons. The HERMES experiment was provided with longitudinally polarized hydrogen/deuterium nuclei until the end of 2000. During the HERA shutdown in 2001, the target was changed to enable measurements with transverse polarized hydrogen.

## 1.1 Target chamber

The target chamber, shown in fig. 1.2 is evacuated by two turbo-molecular pumps with a combined speed of 4400 $ls^{-1}$. During operation the chamber pressure is typically in the $10^{-7}$ mbar range due to the high gas load from the atomic beam which enters the chamber under 30° above the horizontal plane. The storage cell and its supporting cooling rails are counter-levered from the upstream[1] end flange.
A thin walled exit window downstream of the target chamber allows the scattered electrons and hadronic fragments to leave the target chamber and to be detected by the HERMES spectrometer [16]. A fixed collimator (labeled as C2) protects the storage cell from direct synchrotron light of the HERA electron beam and from electrons hitting the cell wall. Further upstream of C2 an adjustable collimator (labeled as C1) with a more narrow opening is located which is opened up during electron injection into the HERA storage ring [16].

[1]Upstream and downstream are used with respect to the HERA lepton beam direction

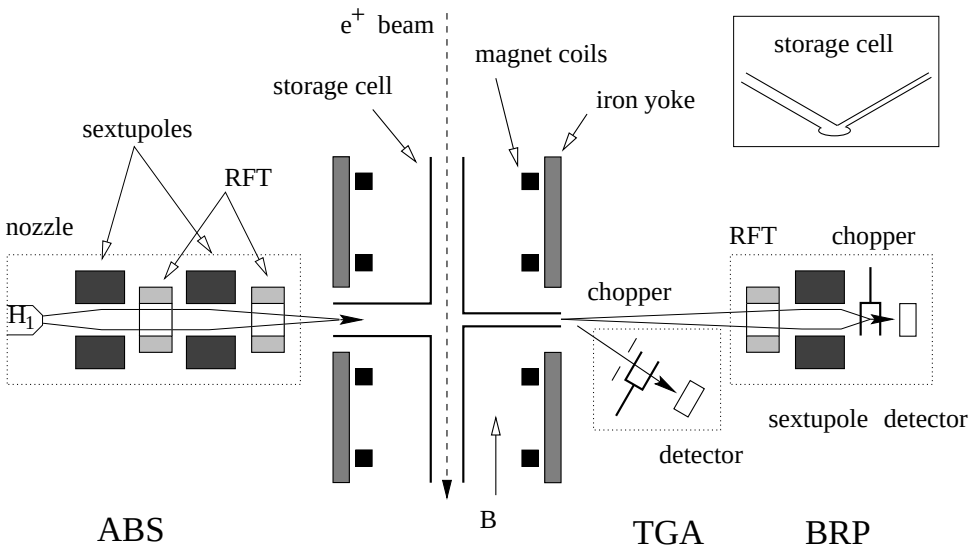


*Figure 1.1: Schematic view of the HERMES longitudinally polarized target. From left to right: Atomic Beam Source (ABS), target chamber with cell and magnet, diagnostic system composed by Target Gas Analyzer (TGA) and Breit-Rabi Polarimeter (BRP).*

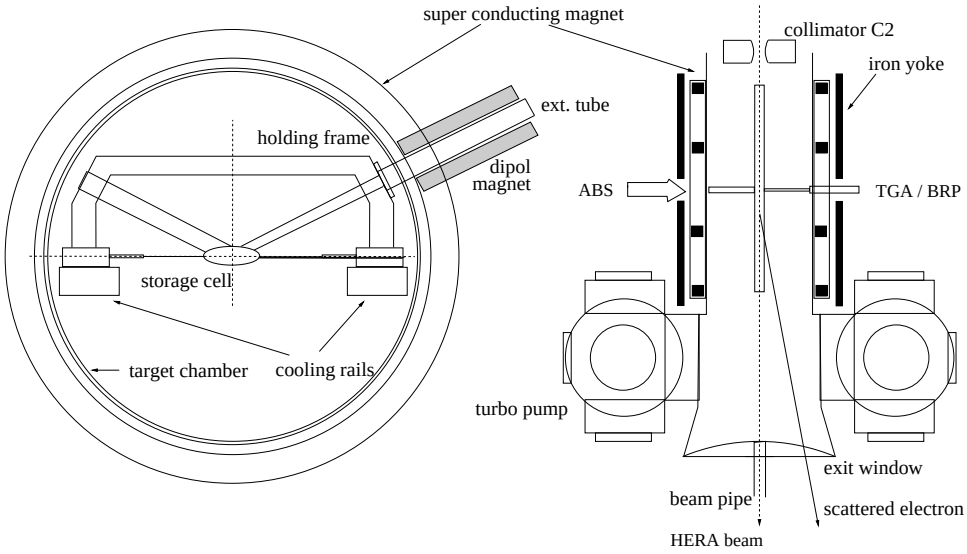


*Figure 1.2: Longitudinal target chamber and superconducting magnet viewed from downstream respect to the HERA beam direction (left) and from above (right).*

## 1.2 Longitudinal magnet

For longitudinal running the storage cell and vacuum chamber are immersed in a longitudinal field generated by a superconducting magnet. The magnet consists of four coils and an iron yoke designed to provide optimum field uniformity over the length of the storage cell while providing a central gap for the atomic beam to enter the cell. The magnetic field (up to 350 mT) provides the quantization axis for the spins of the polarized atoms in the storage cell and decoupling the spins of the nucleons and electrons. The passing HERA beam is bunched to provide high luminosity for the collider experiments H1 and ZEUS and, as discussed in sec. 3.2.3, this may induce resonant nuclear depolarization of the target gas. The induced resonances can be avoided by proper setting of the holding field as long as its homogeneity is sufficient [24]. In case of hydrogen the maximum permissible variation of the magnetic field along the storage cell is 1.5%. For the running period with deuterium gas this requirement was found to be less critical [27].

## 1.3 Transverse magnet

After the end of the longitudinal running, the HERMES target was modified to enable measurements with a hydrogen gas target in a transversally oriented magnetic holding field. The intensity of the transverse magnetic field was limited by the amount of synchrotron radiation power generated by the deflection of the beam by the target magnet (5 kW maximum), and it was decided to build a normal conducting magnet. As will be explained in sec. 3.2.3, a higher homogeneity of the transverse target magnet of $\Delta B \leq 0.15$ mT at a field value of about 300 mT was required.
The geometrical constraints imposed by the larger HERMES acceptance made it more difficult to design a magnet fulfilling the uniformity requirement. After the construction, the field uniformity was measured and improved by shimming the pole tips. At a field strength of $B$=297 mT, maximum deviations of $\Delta B_z$=0.05 mT, $\Delta B_y$=0.15 mT and $\Delta B_x$=0.60 mT within the storage cell volume have been achieved, $z$ being the longitudinal direction, $y$ the transverse and $x$ the horizontal axis. The magnet has been installed in the HERMES hydrogen target in July 2001. The strength of the transverse field vs. z is shown in the lower plot of fig. 1.3.

## 1.4 The storage cell

The HERMES storage cell [20] is made of two 75 $\mu m$ thin pure aluminum sheets which are tightly spot-welded together. It is 400 mm long and has an elliptical cross-sectioned shape of $21 \times 8.9$ mm$^2$. All the aluminum parts of the cell are coated with Drifilm [34] to minimize depolarization and recombination caused by wall collisions [35, 36, 37, 38]. The cell wall extends partly about 147 mm downstream of the cell to ensure that all scattered

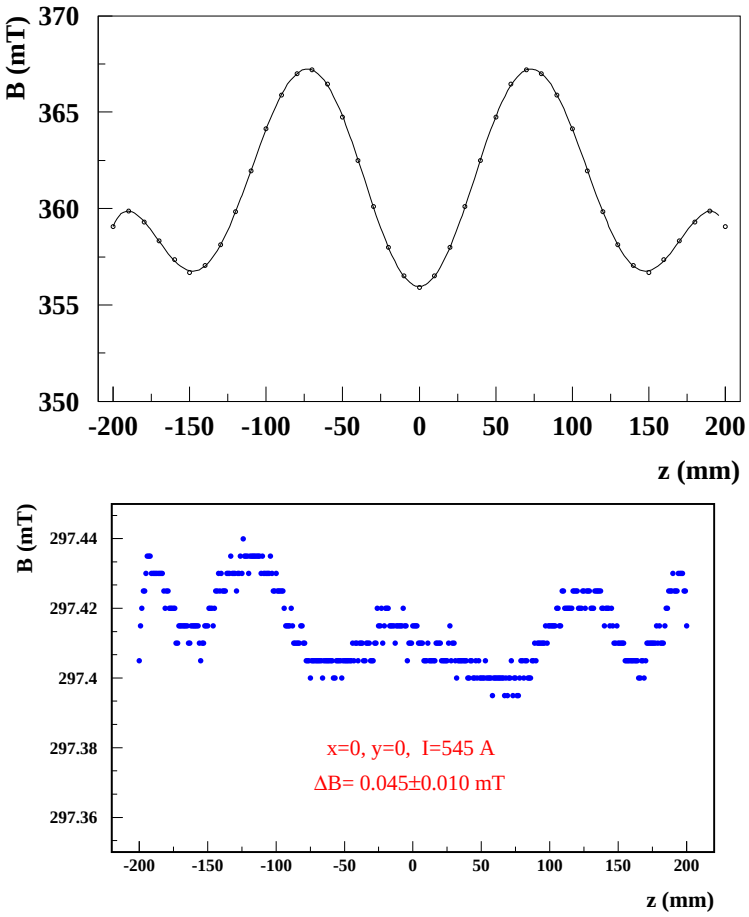


*Figure 1.3: Upper panel: field strength of the longitudinal target magnet measured along the HERA beam direction z covering the full length of the storage cell. The line shows a polynomial fit to the measurement. Lower panel: transverse magnet field uniformity measured along the z axis at the nominal field strength* $B = 297\,mT$*. Deviations of* $\Delta B_y = 0.15\,mT$ *(vert.) and* $\Delta B_x = 0.60\,mT$ *(horiz.) have been measured within the cell volume.*

| period of use | cross section $a \times b$ (mm) | conductance (l/s) |
|---|---|---|
| 05.96 - 11.99 | $29.8 \times 9.8$ | $1.45\sqrt{T/M}$ |
| 01.99 (test) | $19.8 \times 8.0$ | $0.61\sqrt{T/M}$ |
| 12.99 - now | $21.0 \times 8.9$ | $0.8\sqrt{T/M}$ |

*Table 1.1: The history of cells used by HERMES. The lengths of the major and minor axes of the ellipse are indicated by a and b; T is the temperature of the cell in K, and M is the atomic mass of the gas in amu. All the values are obtained by using the analytical formula*

particles inside the spectrometer detector acceptance pass through the same thickness of material (see fig. 1.4).
Cells with three different elliptical cross sections have been used so far. The mentioned size of $21 \times 8.9$ mm$^2$ is the one which is in use since December 1999, called the medium-sized cell. The "large-size" which was used until December 1999 had a cross section of $29 \times 9.8$ mm$^2$ and a "small-one" ($19 \times 8.0$ mm$^2$) was tested in January 1999 and found to be too small. Table 1.1 summarizes dimensions and conductances of the different cells which have been used. The conductance refers to gas injected into the cell center.
Wake field suppressors made of 100 $\mu m$ thick titanium confine the electromagnetic high frequency field of the bunched HERA beam and form an electrical "smooth" connection between the storage cell and the HERA beam pipe.
The storage cell is mounted onto cooling rails which are cooled by temperature regulated gaseous helium. The optimum operating temperature for hydrogen targets was found to be about 100 K where recombination and depolarization effects are low. Additionally, the lower conductance at this temperature leads to a higher target thickness by a factor $\sqrt{3}$ as compared to room temperature. For deuterium gas the target temperature could be decreased further to about 65 K which increased the target thickness by about 23 % compared to 100 K.
The temperature of the cooling rails is monitored at three different positions by platinum resistors. Since 1999 an additional thermocouple wire is attached to the aluminum foil close to the cell ellipse to monitor the cell temperature directly during the injection of the HERA beam when a temperature raise of about 5-10 K is usually detected. The cooling rails are connected to the target chamber flange on the upstream end. Due to thermal contraction of the cell when being cooled, the position of the cell center changes relative to the atomic beam source and the Breit-Rabi polarimeter. From room temperature down to 100 K the cell center moves by 0.9 mm. The alignment of the atomic beam source and Breit-Rabi polarimeter relative to the cell center includes an offset to compensate for this effect at the target working point.
The cell is shown along with its support flange in fig. 1.4. Two side tubes are connected to

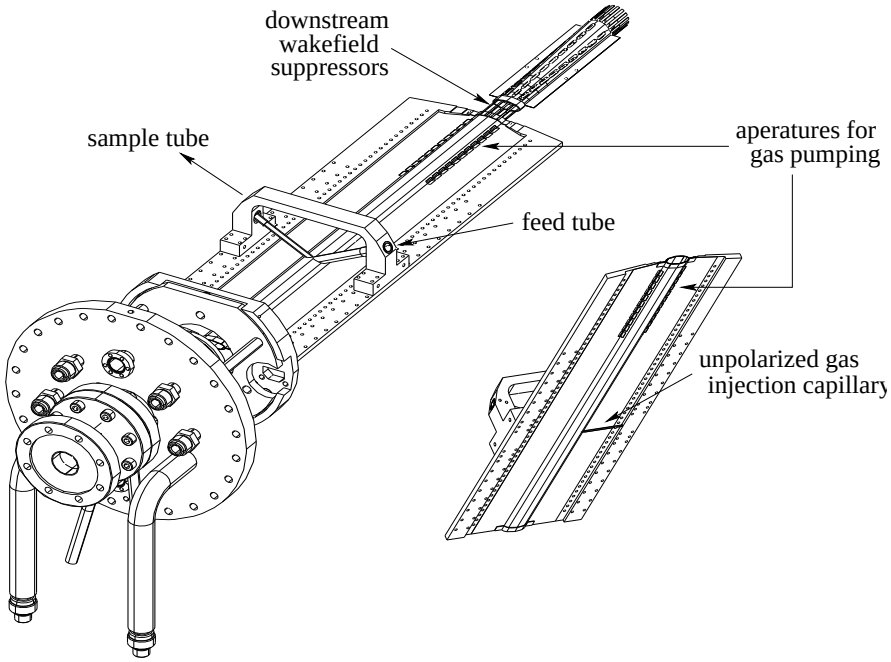


*Figure 1.4: The storage cell and its support flange.*

the beam tube, one to inject the polarized atoms through the injection tube and another, smaller one, to sample about 5% of the target gas and analyze it in the target gas analyzer and the Breit-Rabi polarimeter. The sample tube is tilted by 120° with respect to the axis of the injection tube to ensure that the sampled atoms have thermalized with the storage cell wall. A permanent dipole magnet around the extension tube outside the target chamber extends the magnetic holding field of the target magnet to prevent depolarization inside the extension tube (see fig. 1.2). A capillary near the location of the feed tube allows injection of unpolarized gas into the cell.

## 1.5 Atomic Beam Source

The atomic beam source [19] consists of a dissociator, a powerful differential pumping system, a beam forming system; a sextupole magnet system to focus atoms with $m_S = +\frac{1}{2}$ into the storage cell and adiabatic high-frequency transitions to manipulate the hyperfine population of the atomic beam. With the HERMES setup, injected fluxes of $\Phi^{ABS} \approx 6.5 \times 10^{16}$ atoms/s in case of hydrogen (2 states) and $\Phi^{ABS} \approx 4.5 \times 10^{16}$ atoms/s in case of deuterium (3 states) have been observed. These values are calculated from the density-dependent spin exchange relaxation [27] and measured for the hydrogen case, as

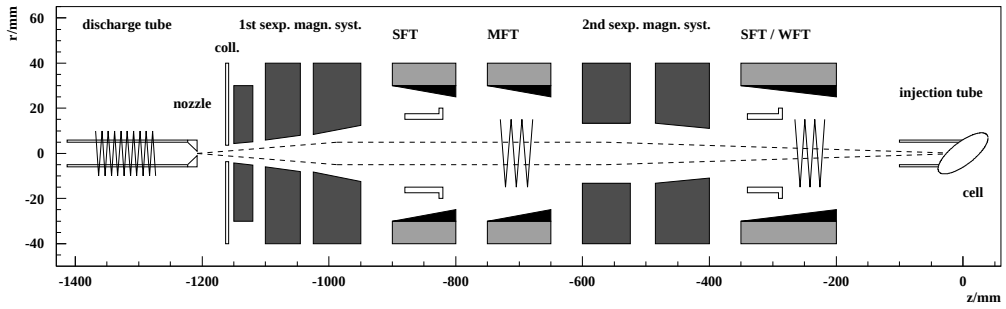


*Figure 1.5: Schematic view (from downstream of the electron beam) of the HERMES ABS with dissociator and collimator for beam formation. Two sets of sextupole magnets are located along the beam axis as are the high-frequency transitions. The axis of the ABS is tilted by* 30° *downwards with respect to the horizontal plane.*

discussed in section 6.3.4. The injected nuclear polarization $P_z^{inj}$ was constantly above 0.97 for hydrogen and above 0.91 for deuterium. A schematic picture of the ABS setup is depicted in fig. 1.5.

Pure molecular hydrogen/deuterium gas enters the dissociator from the left. The molecules are dissociated by a radio frequency discharge with a frequency of 13.56 MHz in a Pyrex tube of the dissociator reaching a degree of dissociation up to 80 % ($H_2$,$D_2$) at a throughput of about 1 mbar l $s^{-1}$ and radio frequency powers of 300 W. To maximize the stability and the degree of dissociation an amount of oxygen between 0.1 and 0.3 volume percent is added to the molecular gas.

A high degree of dissociation at higher throughput can be achieved using a recently developed microwave (MW) dissociator [39]. The microwave dissociator operates at a frequency of 2.45 GHz. With typical throughput between 1 mbar l $s^{-1}$ and 2 mbar l $s^{-1}$ and microwave powers of about 600 W a degree of dissociation higher than 80 % is achieved. The MW dissociator has been used in the year 2000 when running with deuterium while the RF dissociator has been used for the rest of the data taking.

The atomic gas flows through a conical nozzle with an opening diameter of 2 mm which is cooled to about 100 K. The water produced in the discharge then freezes at the nozzle and reduces surface recombination. The ice layer continuously thickens and slowly reduces the gas conductance of the nozzle. After typically 3-5 days of operation the pressure in the dissociator tube rises substantially to increase volume recombination in the tube, resulting in a noticeable decrease in the degree of dissociation of gas exiting the nozzle. Full recovery is achieved by slightly warming up the nozzle to remove the ice layer.

After passing the cold nozzle the gas expands into the vacuum of the dissociator chamber. A powerful differential pumping system with a total nominal pumping speed of more than 15000 $ls^{-1}$ ensures low gas flow into the HERA vacuum system.

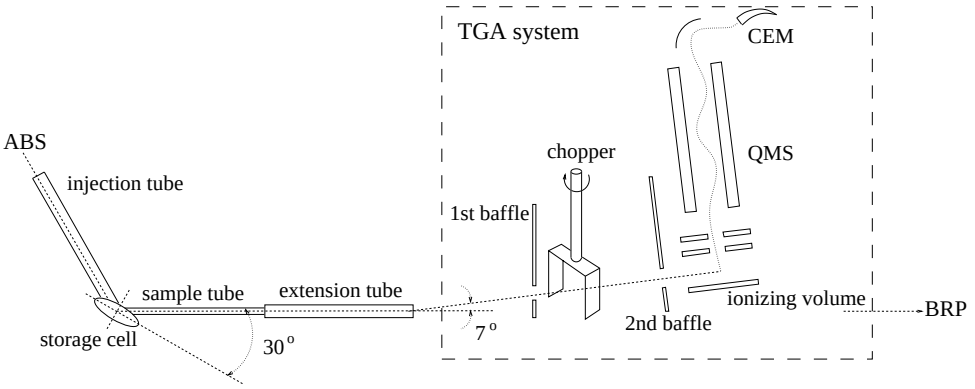


*Figure 1.6: A schematic diagram of the Target Gas Analyzer. The gas of atoms and molecules diffuses through the extension tube and is collimated by two baffles before entering the ionizing volume. The chopper is used for background subtraction*

The magnet system of the HERMES atomic beam source consists of a total of five Halbach [40] type segmented permanent sextupole magnets with a maximum poletip field of about 1.5 T. Every magnet consists of 24 segments of *Vacodym*[2]. Four high frequency transition units are available: two in between the sextupole magnets and two after the last magnet. The system provides enough flexibility that many different combination of hyperfine population can be injected into the cell. Between the sextupoles, a strong field transition (SFT) and a medium field transition (MFT) can be used simultaneously whereas the weak field transition (WFT) and the SFT after the sextupole magnets can only be used separately, because they share the coils for the static and gradient magnetic fields. The complete set of possible hyperfine populations that can be produced is shown in tab. 1.2.

## 1.6 Target Gas Analyzer

The target gas analyzer (TGA) [21] measures the atomic and the molecular content of the gas extracted from the storage cell by the sample and extension tubes.
The TGA setup, shown in fig. 1.6, consists of a pair of baffles, a chopper, a 90° off-axis quadrupole mass spectrometer (QMS) with a cross beam ionizer and a channel electron multiplier (CEM) for single ion detection.
The TGA is integrated into the vacuum system of the BRP sextupole chamber, which is served by two cryo pumps and a titanium sublimation pump, with a total pumping speed of about 7000 $ls^{-1}$. During operation, the pressure in the TGA detector is about $4{\cdot}10^{-9}$ mbar. Prior to normal operation, the TGA vacuum chamber is backed out with

[2]Vacodym is a registered trademark of Vacuumschmelze GmbH, Hanau, Germany

temperatures up to 180 °C for 48 hours. The BRP/TGA vacuum scheme is shown in fig. 1.7.
The TGA is mounted 7° off-axis with respect to the BRP, in order not to interfere with the beam entering the polarimeter. The first baffle ensures that only gas from the sample beam can reach the detector, while the second one acts as a collimator, so that no atoms

| Gas | HFT (betw. 6-poles) | HFT (after 6-poles) | Inj. States | $P_e$ | $P_z$ | $P_{zz}$ | Use |
|---|---|---|---|---|---|---|---|
| **H** | - | - | $\|1\rangle$, $\|2\rangle$ | +1 | 0 | - | Cal |
| | - | WFT 1-3 | $\|2\rangle$, $\|3\rangle$ | 0 | -1 | - | Data |
| | - | SFT 2-4 | $\|1\rangle$, $\|4\rangle$ | 0 | +1 | - | Data |
| | SFT 2-4 / MFT 2-3 | - | $\|1\rangle$ | +1 | +1 | - | Cal |
| | WFT 1-3 / MFT 1-3 | - | $\|2\rangle$ | +1 | -1 | - | Cal |
| | SFT 2-4 / MFT 2-3 | WFT 1-3 | $\|3\rangle$ | -1 | -1 | - | Cal |
| | WFT 1-3 / MFT 1-3 | SFT 2-4 | $\|4\rangle$ | -1 | +1 | - | Cal |
| | WFT 1-3, SFT 2-4 | - | *no state* | - | - | - | Cal |
| **D** | - | - | $\|1\rangle$ $\|2\rangle$ $\|3\rangle$ | +1 | 0 | 0 | Cal |
| | SFT 2-5 | WFT 1-4 | $\|3\rangle$ $\|4\rangle$ | 0 | -1 | +1 | Data |
| | SFT 3-5 | SFT 2-6 | $\|1\rangle$ $\|6\rangle$ | 0 | +1 | +1 | Data |
| | MFT 1-4 | SFT 3-5 | $\|2\rangle$ $\|5\rangle$ | 0 | 0 | -2 | Data |
| | MFT 1-4 | SFT 2-6 | $\|3\rangle$ $\|6\rangle$ | 0 | 0 | +1 | Data |
| | MFT 3-4, SFT 2-6 | - | $\|1\rangle$ | +1 | +1 | +1 | Cal |
| | WFT 1-4, SFT 2-6 | - | $\|2\rangle$ | +1 | 0 | -2 | Cal |
| | WFT 1-4, SFT 3-5 | - | $\|3\rangle$ | +1 | -1 | +1 | Cal |
| | MFT 3-4, SFT 2-6 | WFT 1-4 | $\|4\rangle$ | -1 | -1 | +1 | Cal |
| | WFT 1-4, SFT 3-5 | SFT 3-5 | $\|5\rangle$ | +1 | 0 | -2 | Cal |
| | WFT 1-4, SFT 2-6 | SFT 2-6 | $\|6\rangle$ | -1 | +1 | +1 | Cal |

*Table 1.2: Injection modes of the atomic beam source. The table shows the high frequency transition units employed ($2^{nd}$ and $3^{rd}$ column), the hyperfine states injected in the target cell and the resulting electron ($P_e$), nuclear ($P_z$) and tensor ($P_{zz}$) polarizations in the ideal case of 100 % efficient sextupole system and transition units, no depolarization inside the target cell and infinitely strong guide field. The last column clarifies the purpose of each mode (Cal: calibration, monitoring; Data: HERMES data taking). The injection modes for hydrogen and deuterium single states are listed separately. For some modes the MFT between the sextupoles has to be tuned as a WFT 1-4. The no state injection mode is only possible for hydrogen and has been operational since April 2002.*

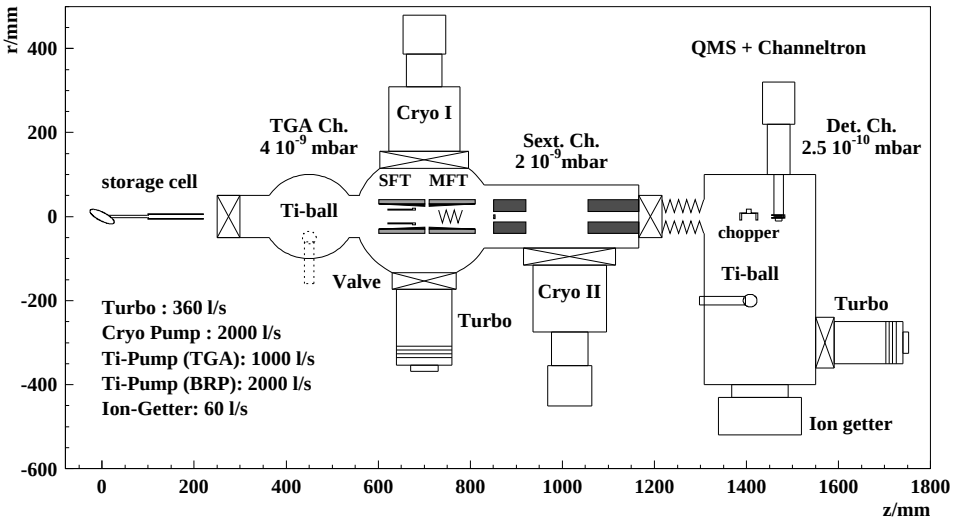


*Figure 1.7: Schematic view of the BRP/TGA vacuum system.*

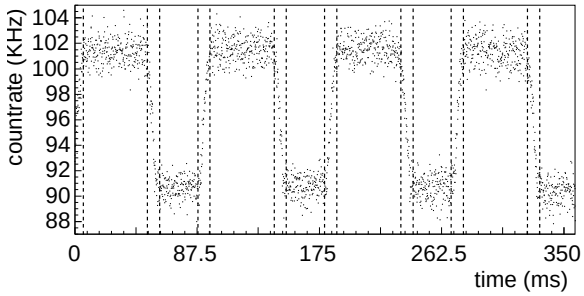


*Figure 1.8: Time spectrum of atomic count rates in the TGA. The vertical lines indicate the bin numbers corresponding to the limits between the chopper positions open, undefined and closed.*

can hit the metal parts of the ionizer and recombine. The chopper, placed between the two baffles, rotates at a frequency of 5.5 Hz, thus periodically blocking the sample beam in order to allow subtraction of the residual gas signal. Particles entering the detector are ionized by 70 eV electrons, mass filtered with the QMS, and finally detected by the CEM. The pulses are counted by a 2048 bin time resolving counter (TRC). The bin length is typically set to 175 $\mu$s so that two chopper turns are collected within the whole bin range as shown in fig. 1.8. The synchronization between chopper status and counting rate is given by a trigger signal coming from the chopper motor. The beam rate is calculated by taking the difference between the number of counts collected with the chopper open and closed.

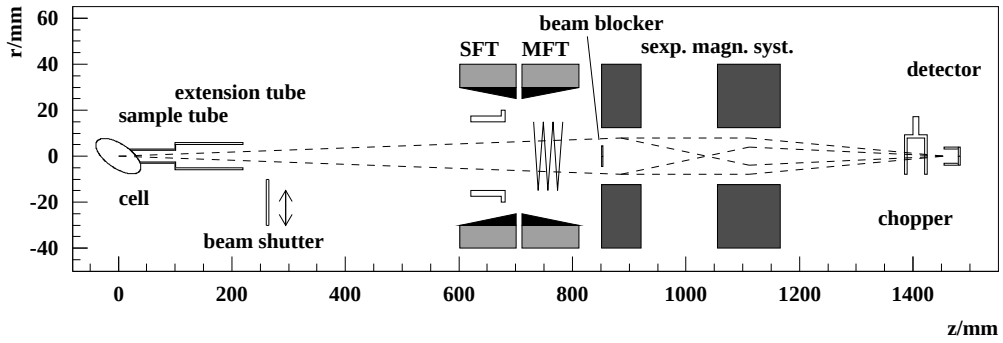


*Figure 1.9: Schematic layout of the BRP. The rf-transition units extend from z = 600 to 810 mm. The beam blocker at the entrance to the first 6-pole magnet ensures 100 % rejection of atoms with $m_s = -\frac{1}{2}$. The beam shutter is used to measure the hydrogen contribution coming from dissociative water ionization.*

## 1.7 Breit-Rabi Polarimeter

The Breit-Rabi polarimeter (BRP) [22] measures the relative populations $n_i$ of the hyperfine states of hydrogen (or deuterium) atoms contained in the sample beam. From this measurement, the absolute atomic polarization can be calculated by applying the knowledge of the target magnetic field strength.
A schematic view of the BRP is shown in fig. 1.9. The sample beam, from left to right, leaves the extension tube of the target cell encountering first two hyperfine transition units, then a sextupole magnet system and eventually the detector stage.
A differential pumping system keeps - during operation - the pressure at $2\times10^{-9}$ mbar in the sextupole chamber and at $2.5\times10^{-10}$ mbar in the detector chamber.
Two transition units are used to exchange the populations between pairs of hyperfine states: a strong field transition unit (SFT) with tilted resonator which can be tuned for both $\pi$ and $\sigma$ transitions, and a medium field transition (MFT) unit which can induce different $\pi$ transitions according to the static field strength and gradient setting used. The sextupole system, composed of two magnets, spin filters the sample beam by focusing atoms with $m_s = +\frac{1}{2}$ towards the BRP geometrical axis and defocusing atoms with $m_s = -\frac{1}{2}$ away. A 9 mm diameter beam blocker placed in front of the first sextupole magnet ensures that no atoms in $m_s = -\frac{1}{2}$ states can reach the detector. The sextupole system has been redesigned in the year 2000 in order to improve the transmission probability at the typical HERMES working temperature. The detector stage is identical to the one employed for the target gas analyzer: a cross beam ionizer, a quadrupole mass spectrometer (QMS) and a channel electron multiplier (CEM). In contrast to the TGA, only hydrogen (or deuterium) *atoms* are detected by the BRP. The chamber residual gas correction is carried out by using a chopper in the same way as described for the TGA.

An additional beam shutter, placed just after the extension tube exit, is used to measure the possible contribution of atomic hydrogen coming from the dissociation of $H_2O$ and $H_2$ ($D_2O$, DHO, $D_2$ and DH in the deuterium case) present on the vacuum chambers walls[3].

## 1.8 The unpolarized gas feed system (UGFS)

The unpolarized gas feed system is required for the unpolarized physics program of the HERMES experiment and it has been used for the absolute measurement of the target density which has been employed to extract the spin - exchange collision cross section as described in chapter 6.
Figure 1.10 shows a sketch of the UFGS. To precisely determine the flux injected into the cell the system has to be calibrated. The aim of the calibration is the measurement of the conductance of the *capillary 1*[4]. Once the conductance $C$ (l/s) of the *capillary 1* is known, the flux injected into the cell, $\Phi_{cell}$ (mbar*l/s), can be estimated with the formula:

$$\Phi_{cell} = C \cdot \Delta p \tag{1.1}$$

where $\Delta P$ (mbar) is the pressure drop in *capillary 1*, as measured by the *differential baratron*. The conductance $C$ can be measured by means of the following procedure. First of all, one or more of the three calibrated *volumes* are filled with gas. After that, all the valves below the *baratron 2* are closed so that the gas flows into the cell. The flux before *capillary 1* ($\Phi_{cap}$) is given by the formula:

$$\Phi_{cap} = -V \cdot \frac{dp_2}{dt} \tag{1.2}$$

where $V$ is the used *volume* and $p_2$ is the pressure measured by the *baratron 2*. As the pressure before *capillary 1* is given by $(p_3 - 0.5 \cdot \Delta p)$, where $p_3$ is the pressure measured by the *baratron 3*, the conductance of the *capillary* is finally given by:

$$C = \frac{\Phi_{cap}}{(p_3 - 0.5 \cdot \Delta p)} \tag{1.3}$$

The UGFS is also used to perform target calibration (rest gas calibration).

## 1.9 The luminosity monitor

Even if the lumi monitor is not a target device, it was used to determine the absolute value of the target density, as explained in sec 6.3.4.

[3]The beam shutter was installed at the beginning of the deuterium running period, in 1998. During the 1996/'97 hydrogen running period, the contribution of dissociative hydrogen ionization was taken into account by detecting the amount of masses 2 and 18 amu in addition to mass 1 amu [27].

[4]Note that, as the pressure involved are high the conductance is depending by the pressure.

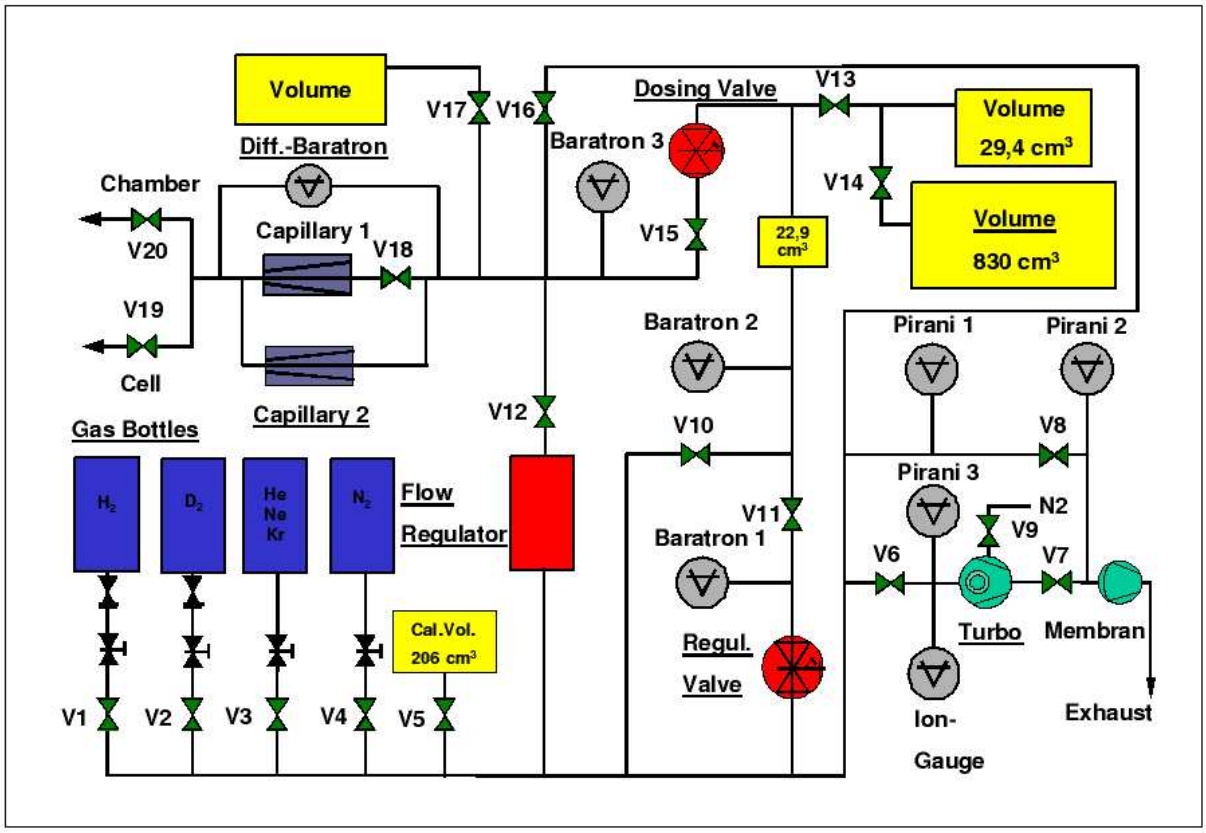


*Figure 1.10: Schematic view of the UGFS. The main elements are: the pump stand used to evacuate the system when a new gas is injected into the Hermes cell, the regulation valve used to fill the volume, the dosing valve used to select/regulate the flow, the capillary and the volume (the 22.9 $cm^3$ one) used to calibrate the system (see text), the gas bottle give the opportunity to chose over different kind of gas (Ar, Kr, Ne, $D_2$, $H_2$).*

The HERMES luminosity monitor (Lumi) [29, 30, 31, 32] is a part of the HERMES spectrometer [16] and detects the Bhabha scattering ($e^+e^- \rightarrow e^+e^-$) and the positron electron annihilation ($e^+e^- \rightarrow \gamma\gamma$) of the HERA positron beam with the electrons of the target gas under small angles. If the HERA storage ring is filled with electrons, the detected process is represented by the Moeller scattering ($e^-e^- \rightarrow e^-e^-$). The number of events is proportional to the electron density inside the storage cell and therefore to the number of nucleons in the target.
The (coincidence) countrate in the luminosity monitor $R_L$ is given by:

$$R_L = \sigma \frac{I_{beam}}{e} D_t \,, \tag{1.4}$$

where $I_{beam}$ is the HERA beam current, $e$ is the charge of the electron and $D_t$ the integrated target thickness (of electrons). $\sigma$ is the total cross section for detectable processes integrated over the detector acceptance and can be obtained by a Monte Carlo simulation. The resulting average nucleus[5] volume density $\langle\, n \,\rangle$ is then:

$$\langle\, n \,\rangle = \frac{e}{\sigma\, 2\, L} S_L \,, \tag{1.5}$$

where $L$ is the length of one wing of the storage cell ($L = 20\, cm$) and $S_L = \frac{R_L}{I_{beam}}$ is the relative Lumi countrate.
As the target density scales like $1/\sqrt{T_{cell}}$, where $T_{cell}$ is the temperature of the storage cell, one can define the normalized quantity[6]

$$\langle\, n \,\rangle_{norm} = \langle\, n \,\rangle \sqrt{\frac{T_{cell}}{100}} \tag{1.6}$$

which can be related to the target average atomic fraction, provided that the ABS performance is stable.
Besides the density measurement, the luminosity monitor can be used to determine the electron polarization of the target. This can be done by looking at the rate asymmetry for different target injection modes:

$$A = \frac{\sigma^{\uparrow\uparrow} - \sigma^{\uparrow\downarrow}}{\sigma^{\uparrow\uparrow} + \sigma^{\uparrow\downarrow}} = \frac{N^{\uparrow\uparrow} L^{\uparrow\downarrow} - N^{\uparrow\downarrow} L^{\uparrow\uparrow}}{N^{\uparrow\uparrow} L^{\uparrow\downarrow} + N^{\uparrow\downarrow} L^{\uparrow\uparrow}} \tag{1.7}$$

where $\sigma^{\uparrow\uparrow}$ ($\sigma^{\uparrow\downarrow}$) is the total polarized cross section for pairs of particles with parallel (antiparallel) spin integrated over the detector acceptance, whereas $N^{\uparrow\uparrow} L^{\uparrow\downarrow}$ ($N^{\uparrow\downarrow} L^{\uparrow\uparrow}$) is the correspondent luminosity corrected count rate.
The target electron polarization $P^T$ is related to the measured asymmetry $A$ through:

$$P^T = \frac{A}{\bar{a}_{zz}\, P_b} \tag{1.8}$$

[5]The number of electrons, in the case of hydrogen, in the target gas, is equal to the number of nuclei.
[6]The reference value $T_{cell} = 100\,\mathrm{K}$ corresponds to the working point temperature of the hydrogen target.

$P_b$ representing the beam polarization[7] measured by the two HERA e-beam polarimeters, while $\bar{a}_{zz}$ is either given by the average between the Bhabha scattering and $e^+e^-$ annihilation asymmetry factors for a positron beam, or by the Moeller scattering asymmetry factor for an electron beam. The acceptance corrected term $\bar{a}_{zz}$ can be computed numerically using the analytical expressions of cross sections and asymmetry factors or, alternatively, through a Monte Carlo simulation [33]. During "normal" data taking, the target is alternately filled with positive - hydrogen (deuterium) hyperfine states $|\,1\,\rangle$ and $|\,4\,\rangle$ ($|\,1\,\rangle$ and $|\,6\,\rangle$) - and negative - $|\,2\,\rangle$ and $|\,3\,\rangle$ ($|\,3\,\rangle$ and $|\,4\,\rangle$) - nuclear polarization, so that the polarization of the electrons is typically very close to zero and no asymmetry can be measured by the lumi. However, this possibility can be exploited during special so-called *Bhabha* or *Moeller* runs, during which the target electron polarization is flipped.

[7]The electron/positron beam of the HERA storage ring is self polarized due to the Sokolov-Ternov mechanism [14].

# Chapter 2

# Analysis of TGA and BRP signals

## 2.1 Interpretation of the TGA signals

The measured TGA atomic (molecular) signal $S_a$ ($S_m$) is proportional to the product of the *particle* flux $\Phi_a$ ($\Phi_m$) into the TGA, the mean inverse velocity of the particles $\left\langle \frac{1}{v_a} \right\rangle$ ($\left\langle \frac{1}{v_m} \right\rangle$), the ionization cross section $\sigma_a^{ion}$ ($\sigma_m^{ion}$) and the detection probability $\epsilon_a$ ($\epsilon_m$). The dependence of the signal on the emission current, which also exists, is measured and taken into account by the normalization function $f(I_{emiss})$. Taking all parameters into account one finds[1]:

$$S_{a,m} \propto f(I_{emiss})\ \sigma_{a,m}^{ion}\ \epsilon_{a,m} \left\langle \frac{1}{v_{a,m}} \right\rangle \Phi_{a,m}. \tag{2.1}$$

The total flux of H or D nucleons into the TGA, $\Phi^{TGA}$, can be related to the fluxes of particles, $\Phi_a$ and $\Phi_m$, by:

$$\Phi^{TGA} = \Phi_a + 2\Phi_m. \tag{2.2}$$

The TGA geometrical acceptance is such that detected particles have bounced, on average, more than 100 times onto the extension tube inner surface [27]. For this reason, particles entering the TGA detector have thermalized with the extension tube wall.
For thermalized atoms and molecules one has:

$$\left\langle \frac{1}{v_m} \right\rangle = \sqrt{2} \left\langle \frac{1}{v_a} \right\rangle. \tag{2.3}$$

Using eqs. (2.1), (2.2) and (2.3), it can be shown that the partial beam rates $S_a$ and $S_m$ can be combined to form the variable $S_{tot}$ which is proportional[2] to $\Phi^{TGA}$:

[1] the influence of external magnetic fringe fields of target and spectrometer magnets can be neglected as both magnets are always kept on during data taking and target calibration

[2] The factor $\sqrt{2}$ instead of 2 is related to the different average velocities of atoms and molecules.

$$S_{tot} = S_a + \kappa \sqrt{2}\, S_m \propto \Phi^{TGA}, \tag{2.4}$$

where $\kappa$ is the calibration constant of the TGA giving the relative sensitivity of the TGA for atomic and molecular beams:

$$\kappa = \frac{\sigma_a^{ion}\ \epsilon_a}{\sigma_m^{ion}\ \epsilon_m}. \tag{2.5}$$

In eq. 2.5 the $\sigma$'s are the cross-sections and the $\epsilon$'s are the combined collection and transmission efficiencies.
Eq. 2.4 applies to the case of constant extension tube temperature, $T_{ext}$, and emission current, $I_{emiss}$. Taking into account the dependence of $S_a$, $S_m$ on the measured[3] $T_{ext}$ and $I_{emiss}$ one can define a temperature and emission normalized nucleons flow rate, $\phi_{tot}$, proportional to the injected ABS intensity $\Phi_{ABS}$:

$$\phi_{tot} = \frac{S_{tot}\sqrt{T_{ext}}}{f(I_{emiss})} \propto \Phi^{TGA}. \tag{2.6}$$

The quantity $\phi_{tot}$ is a good monitor of ABS stability over time as it is independent of recombination inside the storage cell. Following eq. 2.6 one can also express normalized nucleons flow rates for atoms, $\phi_a$, and for molecules, $\phi_m$, by:

$$\phi_a = \frac{S_a\sqrt{T_{ext}}}{f(I_{emiss})} \tag{2.7}$$

$$\phi_m = \frac{\sqrt{2}\kappa S_m\sqrt{T_{ext}}}{f(I_{emiss})}. \tag{2.8}$$

The degree of dissociation of the sample beam, defined as the fraction of nucleons in atoms relative to all nucleons entering the TGA, is given by

$$\alpha^{TGA} = \frac{\phi_a}{\phi_a + \phi_m} = \frac{S_a}{S_a + \sqrt{2}\,\kappa\ S_m}. \tag{2.9}$$

The degree of dissociation $\alpha^{TGA}$, also called atomic fraction, is displayed by the TGA roughly once per minute.

[3] A thermocouple on the extension tube was first installed at the beginning of 1999. In the 1997 analysis, the extension tube temperature has been derived using the expression $T_{ext}(T) = T_0 + \frac{300-T_0}{300}T$, where $T_0$ is a constant and T is the measured cell temperature in K.

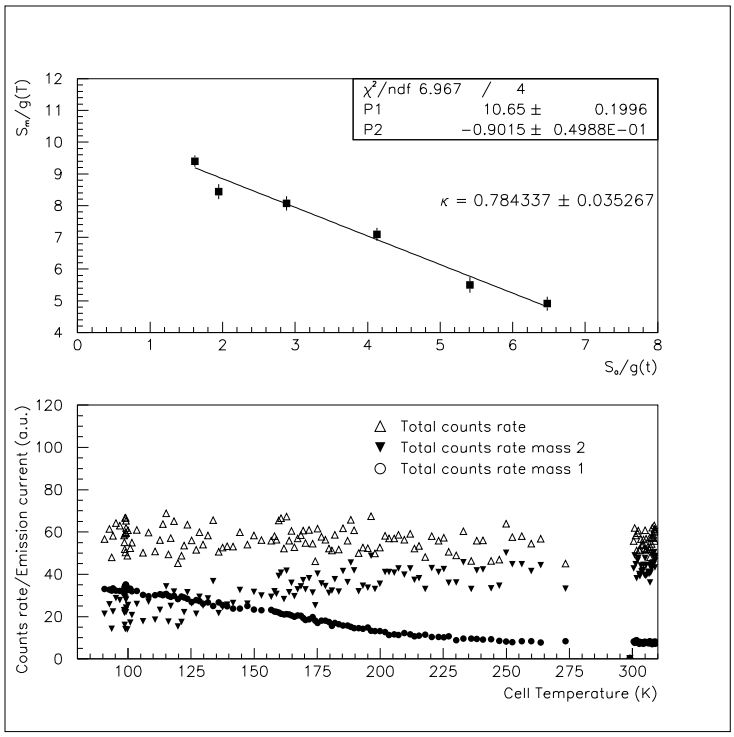


*Figure 2.1: The upper plot shows the molecular count rates versus the atomic one during the cell cooling down, normalized by the temperature function. The lower plot shows the counts rate versus the temperature. The total count rates are corrected by the $\kappa$ value derived from the fit and are constant on the whole range.*

## 2.2 The calibration of the TGA

The purpose of the TGA calibration is to determine the relative sensitivity $\kappa$ defined by eq. 2.5. The calibration can be performed by varying the relative amount of atoms and molecules at a constant injected ABS total flux:

$$\phi_{tot} = \phi_a + \phi_m = const. \tag{2.10}$$

Using the relations (2.7) and (2.8), one can write

$$\frac{\partial\left(\frac{S_m}{g(T)\, f(I_{emiss})}\right)}{\partial\left(\frac{S_a}{g(T)\, f(I_{emiss})}\right)} = -\frac{1}{\sqrt{2}\,\kappa}, \tag{2.11}$$

where the minus sign reflects the fact that an increase in $\phi_m$ must correspond to a decrease of $\phi_a$. Hence a fit over the normalized molecular signal, $\phi_m$ as function of the normalized atomic one, $\phi_a$ results in a straight line with a slope of $-\frac{1}{\sqrt{2}\,\kappa}$ as shown in figure 2.1.
Because the recombination process in the HERMES target is strongly temperature dependent, a variation of the atomic fraction can be obtained in a controllable way by changing the temperature of the storage cell.
This happen, for example, when at the beginning of the data taking period, a new storage cell is mounted.

| target/year | $\kappa$ |
|---|---|
| $H_{\|\|}(1997)$ | $0.551 \pm 0.026$ |
| $D_{\|\|}(2000)$ | $0.861 \pm 0.024$ |
| $H_{\perp}(2002)$ | $0.55 \pm 0.05$ |
| $H_{\perp}(2005)$ | $0.78 \pm 0.04$ |

*Table 2.1: Summary of the values of TGA calibration constant k for the years 1997-2005.*

A second possibility is to take advantage of an accidental beam loss in the region of the HERMES target which might temporarily change the surface property of the cell and cause a sharp drop of $\alpha^{TGA}$ followed by a slow recovery. This beam loss calibration method does not require any knowledge about the temperature correction function $g(T_{ext})$. The measured values for $\kappa$ are reported in tab. 2.1.
A detailed description about the TGA performance and its calibration can be found in ref. [21].

## 2.3 Interpretation of BRP signals

The atomic signal detected by the BRP depends on the hyperfine population in the sample beam, on the transmission probabilities of the sextupole system and on the setting of the transition units. For a stable storage cell temperature, the transmission of the magnetic system is fixed. On the contrary, the transition units can be switched on and off, changing the intensity of the beam reaching the detector. The BRP signal can be described by the following expression:

$$S_i = c \sum_a \left( \sum_b \sigma_b T^i_{ab} \right) I_a, \tag{2.12}$$

where $I_a$ is the sample beam intensity (in atoms/s) of the atoms in hyperfine state $|\, a \,\rangle$, $T^i_{ab}$ describes the exchange of hyperfine states by the transition unit[4] $i$, $\sigma_b$ is the sextupole transmission probability for state $|\, b \,\rangle$, and $c$ is a proportionality factor[5]. The goal of these measurements is to determine the four (six) sample beam intensities, $I_a$, for the hydrogen (deuterium) sample beam. Summing eq. 2.12 over index $b$ one obtains:

$$S_i = c \sum_a M_{ia} I_a, \tag{2.13}$$

where the *measurement matrix* $M_{ia}$ includes information concerning transmission probabilities and RF-transition efficiencies.

[4]If both units are working, the matrix $T^i$ has to be replaced by $A = \prod_i T^{(i)}$

[5]The expression (2.12) simplifies into $S_{off} = c \sum_a \sigma_a I_a$ in case that no transition unit is switched on.

Assuming that $M_{ia}$ is known, one can solve the system of equations (2.13) for $I_a$ if, during a given ABS injection status, the BRP transition units are operated in at least four (six) different modes in case of hydrogen (deuterium).
The solution is given by

$$I_a = c^{-1} \sum_i R_{ai} S_i, \tag{2.14}$$

where[6] $R = M^{-1}$. The total sample beam intensity, $I_{tot}$, is obtained by the taking the sum over all hyperfine states:

$$I_{tot} = \sum_a I_a. \tag{2.15}$$

Finally, the relative hyperfine populations $n_a$ are given by normalizing the intensities $I_a$:

$$n_a = \frac{I_a}{I_{tot}}. \tag{2.16}$$

The polarization of the atoms in the sample beam can now be calculated from the target magnetic field strength, as expressed by the following vectorial forms for hydrogen and deuterium, respectively:

$$(P_e, P_z)^T = M_P^H (n_1, n_2, n_3, n_4)^T \tag{2.17}$$
$$(P_e, P_z, P_{zz})^T = M_P^D (n_1, n_2, n_3, n_4, n_5, n_6)^T, \tag{2.18}$$

where the matrices $M_P^H$ and $M_P^D$ contain the target holding field strength. e.g. for hydrogen:

$$\mathbf{M_P^H} = \begin{pmatrix} -1 & a & 1 & -a \\ 1 & -a & -1 & a \end{pmatrix}, \tag{2.19}$$

where a $= \frac{\chi}{\sqrt{1+\chi^2}}$, $\chi = B/B_c$, $B_c = 50.7$ mT.
The statistical errors of the measured signals $S_i$ are represented by the diagonal covariance matrix $C_S$. Hence, the covariance error matrix $C_I$ of the intensities $I_a$ is given by:

$$C_I = R C_S R^T = \left(M^T C_S^{-1} M\right)^{-1}. \tag{2.20}$$

The sum over all the elements of $C_I$ gives the statistical error $\Delta I_{tot}$ of the total intensity $I_{tot}$:

[6] If the number of collected signals is larger than the number of unknowns, one has to use the *pseudo-inverse* matrix $R = (M^T G_S M)^{-1} M^T G_S$, where $G_S$ is the inverse covariance matrix of the measured signals. This procedure is equivalent to a fit of the intensities $I_a$ to the signals $S_i$.

$$\Delta I_{tot} = \sum_{ab} (C_I)_{ab}. \tag{2.21}$$

The covariance matrix $C_N$ of the hyperfine populations $n_a$ is

$$(C_N)_{ab} = \sum_{cd} \left( \frac{\partial n_a}{\partial I_c} \right) (C_I)_{cd} \left( \frac{\partial n_b}{\partial I_d} \right), \tag{2.22}$$

while the covariance error matrix of the polarization vector can be calculated in the following way:

$$C_P = M_P^{H,D} C_N \, (M_P^{H,D})^T. \tag{2.23}$$

From $C_P$ one can extract the statistical error of the polarization measurement.
During normal running conditions, the entire automated procedure to measure and calculate the polarization vectors and their uncertainties lasts roughly 60 s (90 s) for hydrogen (deuterium), resulting in a statistical uncertainty of about $\pm 0.013$ for hydrogen. For deuterium the statistical uncertainty is about $\pm 0.031$ for positive and $\pm 0.022$ for negative nuclear polarization. After an optimization of the BRP sextupole system, and an increase in the diameter of the sample tube, the statistical error of a 60 s measurement was reduced to less than 0.5 %.

## 2.4 The BRP calibration

In the previous section it has been shown that the atomic polarization can be calculated from the measured BRP signals assuming the knowledge of the measurement matrix $M_{ia}$. This includes the efficiencies of the transition units and the transmission probabilities of the sextupole system for different hyperfine states. The procedure used to determine these parameters is called BRP calibration.
The basic idea of the calibration measurement is to make the system of equations (2.13) over determined so that additional parameters like efficiencies or sextupole transmissions can be extracted through a fit to the data. Due to the fact that the transition units can be combined in several possible ways, the amount of signals which can be collected during a polarization measurement exceeds the number of hyperfine states $N_{hfs}$. Yet, the number of unknowns which can be determined in this way is still less than the total number of parameters. The problem can be overcome by cycling this measurement through different (total number $N_{ABS}$) injection modes (see tab. 1.2) so that an adequate number of signals can be collected.

| BRP-Signal | Name | MFT-RF | MFT | SFT-RF | SFT |
|---|---|---|---|---|---|
| OFF | off | OFF | OFF | OFF | OFF |
| SFT 1-4 | s14 | OFF | OFF | ON | 1-4 |
| SFT 2-4 | s24 | OFF | OFF | ON | 2-4 |
| MFT 1-3 | m13c14 | ON | 1-3 | OFF | 1-4 |
| MFT 1-3 | m13c24 | ON | 1-3 | OFF | 2-4 |
| MFT 2-3 | m23c14 | ON | 2-3 | OFF | 1-4 |
| MFT 2-3 | m23c24 | ON | 2-3 | OFF | 2-4 |
| MFT 1-3/SFT 1-4 | m13s14 | ON | 1-3 | ON | 1-4 |
| MFT 1-3/SFT 2-4 | m13s24 | ON | 1-3 | ON | 2-4 |
| MFT 2-3/SFT 1-4 | m23s14 | ON | 2-3 | ON | 1-4 |
| MFT 2-3/SFT 2-4 | m23s24 | ON | 2-3 | ON | 2-4 |

*Table 2.2: Possible switching modes of the BRP transition units for hydrogen running. During a calibration measurement all signals are collected, while for a polarization measurement only a subset of them is chosen.*

### 2.4.1 The transition efficiencies

The BRP contains two transition units, a strong field (SFT) and a medium field (MFT) one. The SFT can drive two transitions for hydrogen ($|\,1\,\rangle \leftrightarrow |\,4\,\rangle$ and $|\,2\,\rangle \leftrightarrow |\,4\,\rangle$) and five for deuterium. The efficiencies of the SFT transitions in case of hydrogen are called $\varepsilon_{s14}$ and $\varepsilon_{s24}$. The MFT is a multiple step transition unit which can drive two sub-transitions for hydrogen ($|\,1\,\rangle \leftrightarrow |\,2\,\rangle$ and $|\,2\,\rangle \leftrightarrow |\,3\,\rangle$[7]) and three for deuterium. For hydrogen the MFT is tuned either as a $|\,1\,\rangle \leftrightarrow |\,3\,\rangle$ (which is achieved by applying the $|\,1\,\rangle \leftrightarrow |\,2\,\rangle$ and $|\,2\,\rangle \leftrightarrow |\,3\,\rangle$ transitions sequentially) or as a $|\,2\,\rangle \leftrightarrow |\,3\,\rangle$ only. In the latter case the MFT unit is tuned to avoid the $|\,1\,\rangle \leftrightarrow |\,2\,\rangle$ sub-transition. Although nearly zero, the residual $|\,1\,\rangle \leftrightarrow |\,2\,\rangle$ efficiency for the $|\,2\,\rangle \leftrightarrow |\,3\,\rangle$ tune of the MFT has to be taken into account.
Due to the limited space available for the BRP equipment, there is a cross talk between the two BRP transition units when both static fields are switched on, so that the tuning of the MFT is influenced by the SFT field, whereas the SFT is not influenced by the (low) MFT field. The MFT efficiencies have to be measured separately depending on the SFT setting, as they depend on the exact static field. This leads, for hydrogen, to an increase in the number of MFT efficiencies from four to eight. The different MFT efficiencies are identified by means of the subscripts $C14$ (for SFT 1-4 static field on) or $C24$ (SFT

[7]The order of the sub-transitions depends on the sign of the gradient field which is, in the HERMES BRP, negative [27].

2-4 static field on) and by the subscripts r13 or r23 which indicate the particular sub-transition being considered. For example, the notation $\varepsilon_{m13r23c24}$ represents the efficiency of the transition MFT 1-3, step 2-3, tuned together with the static field of the SFT 2-4. The total number of efficiencies $N_{eff}$ is 10 for hydrogen and 41 in case of deuterium. The number $N_{BRP}$ of possible BRP signals related to different transition states is 11 for hydrogen (as shown in tab. 2.2) and 29 for deuterium.
If the ABS is operated in $N_{ABS}$ different injection modes, and the BRP transition units switch through all possible $N_{BRP}$ states, the total number of collected signals is $N_s = N_{ABS}\,N_{BRP}$. In this way, recalling eq. (2.13), one obtains a system of $N_s$ equations containing $N_u = N_{eff} + N_{ABS}\,N_{hfs}$ unknowns[8], where $N_{hfs} = 4\,(6)$ in case of hydrogen (deuterium). The system can be solved if $N_f = N_s - N_u \geq 0$, where $N_f$ is counting the degrees of freedom and is given by

$$N_f = N_s - N_u = (N_{BRP} - N_{hfs})\,N_{ABS} - N_{eff}. \tag{2.24}$$

In such a case, both the hyperfine state intensities $I_a$ and the transition efficiencies $\varepsilon$ can be determined. For hydrogen, the calibration measurement makes use of 7 ABS injection modes, resulting in $N_f = 39$. In case of deuterium two possible options have been developed, one with 5 ABS modes ($N_f = 74$) and the other with 6 ($N_f = 97$).
The solution of the system is carried out by applying a Runge-Kutta method as explained in [22]. The resulting covariance matrix $C_x$ has the form

$$C_x = \begin{pmatrix} C_\varepsilon & C_{\varepsilon,I} \\ C_{I,\varepsilon} & C_I \end{pmatrix}, \tag{2.25}$$

where $C_\varepsilon$ contains uncertainties and covariances of the efficiencies and is used to calculate the systematic uncertainty of the polarization measurement. The resulting systematic uncertainty induced by the determination of the transition efficiencies of the order of 1.5 %.
Tab. 2.3 and 2.4 summarizes the transition efficiency measurements performed in 1997 and 2004 respectevly with hydrogen. The efficiencies of the transitions for deuterium running can be found in ref. [22].

### 2.4.2 The sextupole transmissions

In the previous section it has been shown how the efficiencies $\varepsilon_i$ of the BRP transition can be measured, assuming a priori knowledge of the sextupole transmissions $\sigma_n$ for different hyperfine states. The attempt to fit both $\varepsilon_i$ and $\sigma_n$ within the same algorithm fails. Nevertheless, the transmission probabilities can be determined by splitting the fitting procedure in two steps, as shown below.

[8] During the evaluation of the transition efficiencies, the sextupole system transmissions probabilities are assumed to be constant.

| Name | MFT | SFT | Efficiency (%) | Error (%) |
|---|---|---|---|---|
| $\varepsilon_{s14}$ | - | 1-4 | 99.3 | 1.34 |
| $\varepsilon_{s24}$ | - | 2-4 | 101.0 | 1.03 |
| $\varepsilon_{m13r12c14}$ | 1-3 | 1-4 | 101.0 | 1.03 |
| $\varepsilon_{m13r23c14}$ | | | 98.6 | 1.41 |
| $\varepsilon_{m23r12c14}$ | 2-3 | 1-4 | -1.0 | 1.13 |
| $\varepsilon_{m23r23c14}$ | | | 94.9 | 1.23 |
| $\varepsilon_{m13r12c24}$ | 1-3 | 2-4 | 99.9 | 0.42 |
| $\varepsilon_{m13r23c24}$ | | | 90.3 | 0.82 |
| $\varepsilon_{m23r12c24}$ | 2-3 | 2-4 | 0.0 | 1.10 |
| $\varepsilon_{m23r23c24}$ | | | 97.4 | 1.04 |

*Table 2.3: BRP transition unit efficiencies measured during the 1997 hydrogen running fixing the sextupole transmission ratio to $r_{21} = 1.029$. Each efficiency is shown along with an explanation of the MFT and SFT static field setting.*

| Name | MFT | SFT | Efficiency (%) | Error (%) |
|---|---|---|---|---|
| $\varepsilon_{s14}$ | - | 1-4 | 99.9 | 0.1 |
| $\varepsilon_{s24}$ | - | 2-4 | 99.6 | 0.1 |
| $\varepsilon_{m13r12c14}$ | 1-3 | 1-4 | 99.6 | 0.2 |
| $\varepsilon_{m13r23c14}$ | | | 98.8 | 0.2 |
| $\varepsilon_{m23r12c14}$ | 2-3 | 1-4 | 2.2 | 0.1 |
| $\varepsilon_{m23r23c14}$ | | | 97.8 | 0.2 |
| $\varepsilon_{m13r12c24}$ | 1-3 | 2-4 | 99.5 | 0.2 |
| $\varepsilon_{m13r23c24}$ | | | 98.8 | 0.2 |
| $\varepsilon_{m23r12c24}$ | 2-3 | 2-4 | 0.0 | 0.1 |
| $\varepsilon_{m23r23c24}$ | | | 96.2 | 0.1 |

*Table 2.4: BRP transition unit efficiencies measured during the 2004 hydrogen running fixing the sextupole transmission ratio to $r_{21} = 1.007$. Each efficiency is shown along with an explanation of the MFT and SFT static field setting.*

In the BRP setup (fig. 1.9), atoms with $m_S = -\frac{1}{2}$ are either defocused or stopped by the beam blocker, having therefore zero transmission probability ($\sigma_3 = \sigma_4 = 0$ for hydrogen and $\sigma_4 = \sigma_5 = \sigma_6 = 0$ for deuterium). Moreover, due to the normalization (eq. 2.16), only ratios of transmission probabilities are required for measuring the hyperfine populations. Thus, the remaining required parameters are $\sigma_2/\sigma_1$ for hydrogen and $\sigma_2/\sigma_1$ and $\sigma_3/\sigma_1$ for deuterium.
The Stern-Gerlach force of the sextupole magnets is weaker for hydrogen atoms in state $|\,2\,\rangle$ compared to state $|\,1\,\rangle$ for magnetic fields B of the order or less than the hydrogen critical field $B_c = 50.7$ mT, near the axis of the sextupole system. Thus near-axis atoms in hyperfine states $|\,1\,\rangle$ and $|\,2\,\rangle$ will experience a different transmission efficiency and the transmission ratio $r_{12} = \sigma_1/\sigma_2$ is expected to exceed unity by a small amount. Due to the smaller hyperfine coupling of deuterium, $B_c = 11.7$ mT, the deviation from unity of the ratio $\sigma_2/\sigma_1$ and $\sigma_3/\sigma_4$, is expected to be significantly smaller than for hydrogen. Ray tracing calculations [19] show that the deviation is in fact negligible. From these consideration it follows that the only transmission ratio that needs to be measured is $r_{21} = \sigma_2/\sigma_1$ for hydrogen.
From the BRP calibration the transition efficiencies are extracted as a function of the parameter $r_{21}$. The transmission ratio can thus be evaluated by minimizing the $\chi^2$ of the calibration results. As the transmission probability of the sextupole system depends on the velocity distribution of the atomic sample, the storage cell temperature $T_{cell}$ has to stay constant over the calibration measurement. This procedure applied to a calibration measurement taken at $T_{cell}$ =95 K has produced the following result [22]:

$$\frac{\sigma_2}{\sigma_1}\Big|_{95\,K} = 1.0290 \pm 0.0015 \tag{2.26}$$

The small error of the measured ratio is neglected in the calculation of the systematic uncertainty of the polarization measurement.
The potential cell temperature dependence of the transition efficiencies can be neglected as the velocity distribution of the sample is fixed by the BRP sextupole system. Therefore, a polarization measurement performed collecting at least one signal more than the minimum required number (as is always the case) can be used to fit the ratio $r_{21}$ for different cell temperatures.
A more detailed description of the BRP calibration and performance can be found in ref. [22].

# Chapter 3

# Processes occurring inside the Storage Cell

Inside the storage cell, the atoms of the target may experience several interactions which have an influence on the average target polarization $P^T$. Their complete understanding is therefore fundamental for the reduction of the systematic error of the target polarization. In this section an overview of the different processes will be given, while a quantitative estimation of the various contributions for the different running periods of the HERMES target can be found in chapter 5. The processes are divided into two categories: recombination processes and spin relaxation processes.

Recombination and relaxation by wall collisions are surface effects whereas spin exchange collisions and resonant interaction of beam and target gas happen in the gas storage cell volume. The experimental conditions of the target are chosen such that these unwanted effects are suppressed as much as possible. It should be noted that spin relaxation can be studied and monitored with good statistics by means of BRP, whereas the residual polarization after recombination can only be studied using scattering process like deep inelastic scattering (DIS) with very low rate.

## 3.1 Recombination Processes

The atoms which are injected into the HERMES storage cell may recombine to molecules keeping partly their nuclear polarization or not. Recombination [23] can in principle take place either on the storage cell walls (surface recombination) or in the gas phase (volume recombination). At the low gaseous densities of the HERMES target volume recombination is negligible. On the cell walls two types of processes with surface catalysis of recombination can be distinguished which are expected to result in different residual nuclear polarization:

- the Langmuir-Hinselwood (L-H) process, where the two adsorbed, thermalized atoms react with each other;

- the Eley-Rideal (E-R) process, where an atom from the gas phase reacts directly with an absorbed atom [42].

The residual polarization of the surface atoms recombining through the E-R mechanism in the cell has been measured with the HERMES spectrometer, making use of a well known DIS asymmetry. The result has been presented in Ref. [25] and it will be discussed in section 5.2.
Since the storage cell temperature usually is kept below 140 K, a small amount of water originating from the dissociation in the atomic beam source freezes on the surface and grows into an ice layer on top of the Drifilm surface. The presence of water is important since water is known to inhibit hydrogen or deuterium recombination. The most likely reason for this is that the chemical binding energy of an hydrogen atom in water (H-OH) of 498 kJmol$^{-1}$ is higher than in a hydrogen molecule (435.99 kJ/mol). The same applies for the case of deuterium, where the bond strength of D-OD is higher than the one of D-D bonds. New storage cell coatings are hydrophobic and the growth of the ice layer is affected by the continuous irradiation of the storage cell surface by the HERA beam which changes the chemical structure of the surface causing the surface to become less hydrophobic. In addition, synchrotron photons cause water molecules to desorb from the cell wall. The ice coverage of the cell surface is thus determined by the radiation dose collected by the surface coating. It has been observed that during the running the amount of recombination in the cell gradually decreases thanks to the water effect, as shown in figure 3.1.
A detailed description of the recombination studies performed on the HERMES storage cell can be found in Ref. [23].

## 3.2 Spin relaxation

Three different spin relaxation mechanisms of atoms can in principle be observed to occur in the HERMES target as they cause a change in the hyperfine population inside the storage cell. One relaxation process takes place on the wall of the storage cell. Another is due to two-body spin-exchange collisions of atoms in the gas phase. Since this process is the main subject of this thesis, it will be explained in details in chapter 6. In the third mechanism the high frequency field associated with the HERA beam can cause a depolarization in the target atoms under certain conditions [24]. Spin relaxation of atomic hydrogen by wall or spin exchange collisions with different types of wall coatings has been under study already for many years in the context of a hydrogen maser for low holding fields [17]. For the HERMES target further studies of the magnetic field dependence of spin relaxation as well as studies of the temperature dependence and of the density

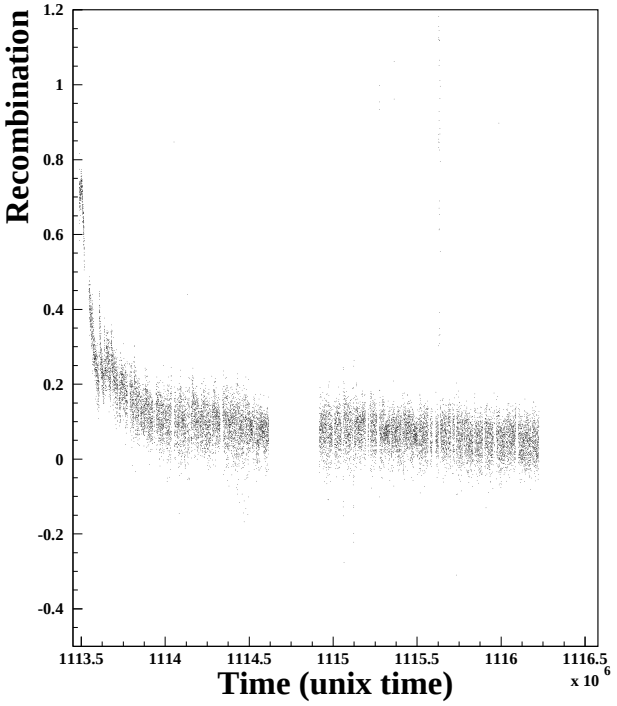


*Figure 3.1: The 10th of April 2005 the target cell was exchanged. Here is shown the recombination behavior once the temperature reached the operational value of 100 K. The Unix time indicate that to build up the ice coverage it took three weeks.*

dependence of the transition spectra have been carried out [27, 47, 48, 49, 50]. The results of these studies are summarized in the following sections

### 3.2.1 Wall relaxation

The atoms injected by the atomic beam source experience some hundreds of wall collisions during their diffusion process through the storage cell. An attractive Van-der-Waals potential between the storage cell wall and a diffusing atom causes the atom to be physisorbed, i.e. to stay for a certain time close to the surface until it is desorbed again. The mean residence time on the wall $\tau_s$ is described by the Arrhenius equation:

$$\tau_s = \tau_0 \, e^{\left(\frac{E_b}{kT}\right)}, \tag{3.1}$$

where $\tau_0$ is the high temperature limit of $\tau_s$, $E_b$ and $T$ are the adsorption energy and temperature respectively, and $k$ is the Boltzmann constant. During the time an adsorbed atom stays on the wall ($\approx 10^{-10}$ s for the HERMES cell), the magnetic moment of its unpaired electron interacts with magnetic moments on the surface by means of a dipolar coupling and/or with other unpaired electrons through exchange interaction [35, 36, 37, 38].

Depending on the surface type, temperature and magnetic field one can define a probability that the atom leaves the wall in a certain hyperfine state. This is described by means of transition probabilities $W_{jk}$ which represents the probability to find an atom in state

$|\,k\,\rangle$ that has been in state $|\,j\,\rangle$ prior to the wall collision.
The theoretical description and the calculation of the transition probability matrix for the HERMES target can be found in [27].

### 3.2.2 Master equation for the description of the spin relaxation process

The different relaxations due to wall collisions and spin exchange collisions cannot be treated separately. After the interaction with the surface during a wall collision the atom in the gaseous phase interacts through spin exchange collision and, at the next wall collision, interacts again with the surface. Since the atoms are constantly exposed to both interactions, an appropriate description is given by a so called *master equation* for the absolute population $N_i$ of the hyperfine state $|\,i\,\rangle$ [27, 47]:

$$\frac{dN_i}{dt} = \frac{1}{\tau_d}(N_i^{inj} - N_i) + \frac{1}{\tau_f}\sum_k W_{jk}N_k + \frac{1}{\tau_{se}}\sum_{jk} M_{jk}^i N_j N_k \tag{3.2}$$

The first part of eq. 3.2 represents the incoming outgoing flux, the third the wall relaxation and the last term the spin exchange relaxation. The effect of recombination is not included in this formula.
In eq. 3.2 three time constants appear: $\tau_d$ (the diffusion time) is the mean occupation time of atoms within the storage cell, $\tau_f$ is the mean time of flight between two wall collisions and $\tau_{se}$ is the mean time between two spin exchange collisions. For times that are large compared to $\tau_d$ the hyperfine population converges toward a dynamical equilibrium (*steady state*). The steady state population is of practical interest, because the BRP requires a stable hyperfine population for a polarization measurement.
The solution of the linear algebraic equation system 3.2 in the steady state has been solved directly in the case of hydrogen or with the help of a numerical iteration algorithm in the case of deuterium [27].
As an example of the application of eq. 3.2, fig. 3.2 represents the measured hyperfine population as a function of the magnetic field for hydrogen and a fit to the data using the solutions of eq. 3.2. A holding field higher than 300 mT is requested to have sizable polarization for the case of two injected states.

### 3.2.3 Bunch field induced depolarization

The beam current of the HERA electron storage ring is bunched with time $\tau_{bunch}$ between two adjacent bunches of 96.1 ns. Typically, most of the 220 RF buckets are filled, so that the bunch frequency is given by:

$$\nu_{bunch} = \frac{1}{\tau_{bunch}} = 10.42\,\text{MHz}. \tag{3.3}$$

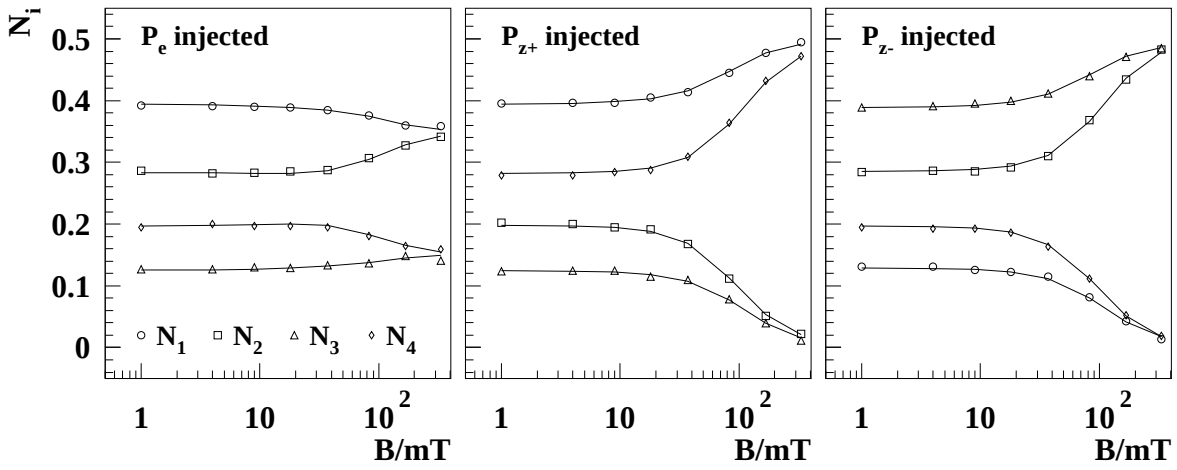


*Figure 3.2: Measured hyperfine population vs. magnetic field for hydrogen for the different injection modes. The measured values are given by symbols, while the lines show a fit using the solutions of eq.3.2*

A large number of harmonics contributes to the induced magnetic high frequency field close to the HERA beam, because the bunches are very short. The transition frequency between two hyperfine states $|\,i\,\rangle$ and $|\,j\,\rangle$ is given by:

$$\nu_{ij} = \frac{E_i(B) - E_j(B)}{h}. \tag{3.4}$$

If at a certain holding field B $\nu_{ij}$ matches one of these harmonics, resonant depolarization occurs. The location of the beam-induced resonances is shown in fig. 3.3. Bunch field induced depolarization at the HERMES target has been studied in case of hydrogen [24, 50] and deuterium [27] for the longitudinal orientation of the target holding field (before 2001). During this time the observed $\pi$ ($\Delta m = \pm 1$) transitions were sufficiently well separated so that at the working point (335 mT) no beam induced depolarization could be found. In the case of the transverse target operating since October 2001, both $\sigma$ ($\Delta m = 0$) and $\pi$ ($\Delta m = \pm 1$) transitions are allowed because the oscillating field surrounding the HERA beam has components both parallel and perpendicular to the static holding field. The spacing between two nearby induced resonances is narrower than in the longitudinal case (only 0.37 mT difference in the magnetic holding field at B = 0.3 T) and a higher homogeneity in the holding field is therefore needed (see fig. 3.3).
Thus, a field intensity for which beam resonant depolarization can be completely suppressed does not exist. A pair of additional correction coils mounted directly near the storage cell has been installed for the 2003 running to reduce the effect of resonant depolarization as much as possible.

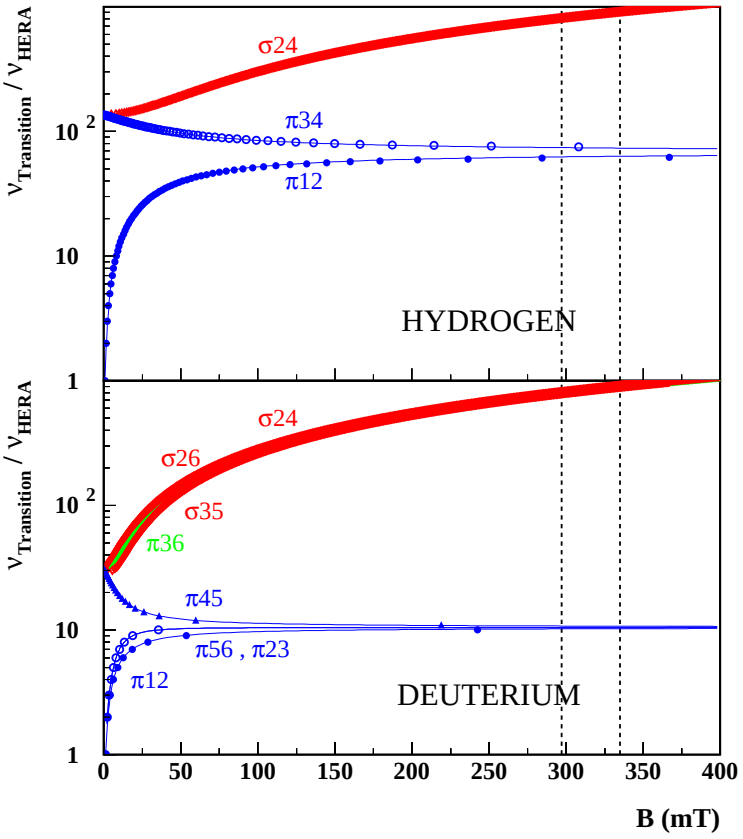


*Figure 3.3:*
*Possible beam induced nuclear depolarizing resonances in the HERMES target. The frequency difference between pairs of hyperfine states whose transitions lead to nuclear depolarization are plotted as a function of the holding field. The frequency values are normalized to* $\nu_{HERA} = 10.42\,MHz$. *The symbols, representing the resonance conditions, are clearly distinguishable for the* $\pi$ *transitions, while they overlap with each other in case of* $\sigma$ *and* $\pi\,|\,3\rangle \leftrightarrow |\,6\rangle$ *transitions, which are separated by a difference in the intensity of the holding field* $\Delta B_T$ *of only 0.37 mT. The dashed lines represent the working point of the transversely (left) and longitudinally (right) polarized targets.*

# Chapter 4

# Target polarization

The average polarization of the nucleons in the target $P^T$ is a fundamental parameter of the HERMES experiment. The problem is to relate the measured polarization of the atoms in the sample beam with the density-weighted average polarization of the nuclei in the cell. The definition of the target polarization involves different terms which mainly account for two effects:

- Presence of molecules in the cell, both unpolarized from the residual gas of the scattering chamber and/or directly injected from the ABS, and polarized molelcules coming from recombination of polarized atoms on the cell surface.

- Relaxation and recombination effects in the storage cell leading to an inhomogeneous distribution of the atomic fraction and of the atomic polarization.

The average target polarization $P^T$ as seen by the electron beam is defined by the following equation:

$$P^T = \alpha_0 \alpha_r P_a + \alpha_0 (1 - \alpha_r) \beta P_a, \tag{4.1}$$

where $\alpha_0$ represents the initial fraction of nucleons in atoms as injected by the ABS (or atomic fraction in absence of recombination), $\alpha_r$ denotes the fraction of nucleons in atoms surviving recombination during their way through the storage cell, $\beta = P_m/P_a$ stands for the ratio of the polarization of the molecules $P_m$ produced by recombination relative to the polarization of the atoms $P_a$. The knowledge of $\beta$ for the experimental conditions at the HERMES experiment will be discussed in Sec. 4.2.
The values for $\alpha_0$, $\alpha_r$ and $P_a$ are calculated using the measurements of the TGA and BRP combined with the various calibrations. As both detectors measure the properties of a sample of the target gas, it is necessary to relate the results to a corresponding value averaged along the storage cell. This is achieved by evaluating the sampling corrections $c_\alpha$ [26]:

| Term | | Meaning |
|---|---|---|
| $P^T$ | | density averaged polarization in the cell |
| $\alpha_0$ | | atomic fraction in the absence of recombination within the cell |
| $\alpha_r$ | $= c_\alpha \alpha_r^{TGA}$ | fraction of atoms surviving recombination in the cell |
| | $c_\alpha$ | sampling correction for the atomic fraction |
| | $\alpha_r^{TGA}$ | measured atomic fraction in the sample beam |
| $(1-\alpha_r)$ | | fraction of atoms recombining in the cell |
| $P_a$ | $= c_P P_a^{BRP}$ | polarization of atoms in the cell |
| | $c_P$ | sampling correction for the atomic polarization |
| | $P_a^{BRP}$ | measured polarization of atoms in the sample beam |
| $\beta$ | $= P_m/P_a$ | relative nuclear polarization of recombined atoms |

*Table 4.1: Meaning of the different terms contained in eq. 4.1.*

$$\alpha_r = c_\alpha \alpha_r^{TGA} \tag{4.2}$$

and $c_P$

$$P_a = c_P P_a^{BRP}. \tag{4.3}$$

The sampling corrections and their systematic uncertainties are functions of the measured values of $\alpha_r^{TGA}$ and $P_a^{BRP}$, respectively. The functions depend on the geometry of the storage cell, its surface properties and the detector acceptances. They are calculated with the help of Monte Carlo simulations of the stochastic motion of particles in the storage cell, where the history of these particles is stored and analyzed. Another possibility is to calculate sampling corrections analytically by describing the diffusion process of the target gas inside the storage cell with the use of a one-dimensional diffusion equation. The issue has been addressed in Ref. [26] and will be discussed here in Sec. 4.4.
The different terms entering the definition of the average polarization are summarized in tab. 4.1.

## 4.1 Determination of the quantities $\alpha_r$ and $\alpha_0$

In order to calculate the target polarization following eq. 4.1, it is necessary to separate the atomic fraction that would be seen by the HERA electron beam if no cell wall recombination were to occur ($\alpha_0$), and the fraction of the initially injected atoms that survive wall recombination, as seen by the HERA electron beam ($\alpha_r$). The measured quantity $\alpha^{TGA}$ can also be factorized in two terms and can be written as (see eq. 2.9):

$$\alpha^{TGA} = \frac{\phi_a}{\phi_a + \phi_m} = \alpha_0^{TGA} \alpha_r^{TGA} \tag{4.4}$$

As long as dissociative ionization can be neglected the only source of atomic flux $\phi_a$ into the gas analyzer is the flux originating from the atomic beam source. The molecular flux $\phi_m$ on the contrary may come from three different sources:

- Undissociated molecules ballistically injected by the ABS. Since the efficiency of the dissociator is around 80 %, a certain amount of molecules passes through the nozzle towards the polarizing stage, affected by neither the sextupole magnets or the transition units. Although the majority of these molecules hits the vacuum chamber wall and is pumped away, a small amount enters into the storage cell via the injection tube. These unpolarized molecules present a triangular density distribution along the cell axis, with the maximum density at the center of the cell.

- Rest gas in the target chamber. These molecules mainly originate from the recombination of atoms that have left the storage cell and have thermalized on the vacuum chamber walls. This molecular component is clearly unpolarized and results in a constant density inside the storage cell.

- Atoms that recombine into molecules after entering the cell. As explained in section 1.4, the cell material and temperature are optimized in order to limit the depolarization and recombination effects in the target atomic gas. Nevertheless, atoms can stick on the cell surface and recombine and the resulting molecules may carry a residual nuclear polarization.

Hence, the normalized total molecular flow rate $\phi_m$ can be decomposed in the following way:

$$\phi_m = \phi_{bal} + \phi_{rg} + \phi_r \tag{4.5}$$

where $\phi_{bal}$, $\phi_{rg}$ and $\phi_r$ represent the ballistic, the rest gas and the recombination components, respectively.
To separate between polarized and unpolarized molecules we rewrite the two factors in eq. 4.4 by using the different contributions defined in eq. 4.5:

$$\alpha_r^{TGA} = \frac{\phi_a}{\phi_a + \phi_r}, \tag{4.6}$$

and

$$\alpha_0^{TGA} = \frac{\phi_a + \phi_r}{\phi_a + \phi_r + \phi_{bal} + \phi_{rg}}. \tag{4.7}$$

The separation of the total molecular flowrate into the single components is accomplished by means of standard *target calibrations* which are usually performed between two HERA electron fills, when the HERMES spectrometer is not taking data.

The rest gas contribution ($\phi_{rg}$) to the molecular flux is linearly proportional to the pressure in the target chamber. The constant of proportionality is determined by injecting into the target chamber increasing quantities of hydrogen (deuterium) molecules with a controlled flow system and by measuring the corresponding TGA count rates.
The ballistic flux contribution ($\phi_{bal}$) can be measured by varying the atomic flux of the injected beam while keeping the molecular flux constant. The atomic flux is changed by using the hyperfine transitions to select either 1 or 2 (or 3 in the case of deuterium) hyperfine states. Since the recombination probability inside the cell is independent of the injected beam intensity, the quantity $\phi_{bal}$ can be extracted. Equation 4.5 is then solved for the remaining molecular flux $\phi_r$.
A detailed description of how these calibrations are performed has been given in Ref. [21]. Once the molecular contributions $\phi_{rg}$, $\phi_{bal}$ and $\phi_r$ are extracted one can determine $\alpha_r^{TGA}$ using eq. 4.6 and thus $\alpha_r$ using eq. 4.2.
The term $\alpha_0$ can be determined without referring to additional sampling corrections. It should be noted that all the $\phi_i$ terms in eq. 4.7 are nucleon fluxes, but $\alpha_0$ is related to nucleon densities in the cell as seen by the HERA beam. In the limiting case of small cell wall recombination, the densities of atoms and molecules arising from $\phi_a$, $\phi_{bal}$ and $\phi_r$ are triangular. In contrast, the rest gas $\phi_{rg}$ has a constant density along the cell and must be weighted by another factor of 2. Additionally, $\phi_{bal}$ and $\phi_{rg}$, having double atomic mass, represent a target thicker by a factor $\sqrt{2}$ for the same TGA flux then atoms. Finally, the terms $\phi_a$ and $\phi_r$ are coupled. An increase in $\phi_r$ is offset by a decrease in $\phi_a$ so that $\phi_a + \phi_r =$ constant. Nevertheless the target density from the nucleons depends on $\alpha_r$ according the term $d = \sqrt{2}/(1 + (\sqrt{2} - 1)\alpha_r)$. Combining the above considerations gives:

$$\alpha_0 = \frac{d(\phi_a + \phi_r)}{d(\phi_a + \phi_r) + \sqrt{2}\phi_{bal} + 2\sqrt{2}\phi_{rg}}. \tag{4.8}$$

## 4.2 Relative polarization of nuclei in recombined atoms ($\beta$)

As mentioned in the previous sections, a certain amount of polarized hydrogen or deuterium atoms may recombine in the storage cell. A direct measurement of the remnant polarization contained in the molecules is not possible at HERMES, as the Breit-Rabi polarimeter can measure the atomic polarization only. The atomic recombination is a temperature dependent surface mediated process [23, 27]. Hence, measurements of the nuclear polarization of recombined atoms using storage cells of different materials and/or with different coatings [51, 52] are not directly applicable to the HERMES case. Without any information about the molecular polarization $\beta$ of nucleons in molecules (or molecular polarization in short) one has to apply in eq. 4.1 the conservative assumption $0 \leq \beta \leq 1$. Recently, a set of data taken in 1997 at higher cell temperature (260 K instead of the

nominal 100 K) could be used to measure $\beta$ for hydrogen at that temperature, resulting in $\beta^{260K} = 0.68 \pm 0.09_{stat} \pm 0.06_{syst}$ [25]. This result can be used as an upper limit for $\beta$ at 100 K ($\beta^{100K}_{high}$) under the following assumptions. The main mechanism responsible for recombination at 100 K and 260 K is the same (i.e. the E-R mechanism). At 100 K, the recombination probability is larger than at 260 K (the atoms impinging from the volume have less kinetic energy to overcome the activation barrier). Thus, the residence time of chemically adsorbed atoms on the surface at 100 K is greater than at 260 K and their possible polarization cannot exceed the value measured at 260 K. This results in $\beta^{100K}_{high} = 0.83$.
The lower limit for $\beta^{100K}$ ($\beta^{100K}_{low}$) can be derived from a simple argument. By assuming that the nucleon spins are not affected by the recombination process, the nuclear polarization of the molecule at the time of its formation ($P^0_m$) can be evaluated by taking the average value of the polarization of an atom coming from the volume ($P_a$) and one resident on the surface ($P_s$). The theoretical lower limit for $\beta^{100K}$ can then be inferred by supposing that atoms sticking on the cell surface are totally depolarized ($P^{100K,low}_s = 0$) and applying the equation:

$$\beta^{100K}_{low} = \frac{P^{100K,low}_m}{P^{100K}_a} = \frac{P^{100K}_a + P^{100K,low}_s}{2} \frac{1}{P^{100K}_a}. \tag{4.9}$$

The result is $\beta^{100K}_{low} = 0.5$. A factor of 0.9 takes the collisional depolarization of the molecules on the walls into account [25, 52], ending in $\beta^{100K}_{low} = 0.45$.
Hence, the range of $\beta^{100K}$ can be limited to

$$0.45 \leq \beta^{100K} \leq 0.83. \tag{4.10}$$

The final value and error of $\beta^{100K}$ is therefore given by:

$$\beta^{100K} = 0.64 \pm 0.19 \tag{4.11}$$

## 4.3 Injected atomic polarization

An important parameter for the exact evaluation of the target polarization is the injected atomic polarization $P^{inj}_a$ (i.e. the atomic polarization in absence of depolarization), as it enables the decoupling of the different spin-relaxation effects. The injected polarization for each ABS operating mode (tab. 1.2) can be calculated if the transmission probabilities of the sextupole system and the efficiencies of the adiabatic transition units are known. The sextupole transmission probabilities for hydrogen and deuterium have been calculated using a Monte Carlo simulation and the results are given in Ref. [19]. The efficiencies of the transitions of the ABS can be extracted by measuring the magnetic field dependence of the spin relaxation processes and by fitting the data with a theoretical model referred to as *'master equation'* which is described in Section 4.2.3 and given by eq. 3.2.

For the HERMES data, the important ABS injection modes are those (two hyperfine states) having a large positive or negative nuclear polarization, $P_{z+}$ and $P_{z-}$ respectively, and, in case of deuterium, the two additional positive and negative tensor polarization ($P_{zz+}$ and $P_{zz-}$) modes (see tab. 1.2).
For hydrogen, only two transitions after the sextupole system are used: the SFT 2-4 for $P_{z+}$ and WFT 1-3 for $P_{z-}$. Therefore, the injected polarizations are directly given by the transition efficiencies whose values have been calculated in Ref. [27] with a technique mentioned and cross-checked using a more direct method based on the symmetry of the spin relaxation processes for the two injection modes. In case of deuterium, several transition units are used to provide the four polarizations, some of which are located between the two sextupole subsystems. Hence, the injected polarizations have to be calculated taking into account the transition efficiencies as well as the transmission probabilities for atoms whose hyperfine state gets changed between the two subsystems.
The calculated polarization for the hydrogen and deuterium beams injected into the target are summarized in tab. 4.2. The degree of nuclear polarization injected by the ABS when running with deuterium is substantially lower than for hydrogen. The reason is that, due to the higher number of hyperfine states, the deuterium nuclear polarization can only be achieved by using the transition units located between the two magnetic subsystems, resulting in an incomplete separation of states.

## 4.4 Sampling Corrections

The sampling correction functions $c_\alpha(\alpha_r^{TGA})$ and $c_P(P_a^{BRP})$ depend strongly on the distribution of recombination and wall relaxation probabilities per wall collision along the storage cell. If the storage cell has not yet been exposed to the HERA beam, one can assume that the recombination and wall relaxation probabilities are constant over the entire surface of the storage cell, or, at least, that microscopic inhomogeneities by differ-

| Mode | Hydrogen | Deuterium |
|---|---|---|
| $P_{z+}^{inj}$ | $97.26 \pm 0.05$ | $87.78 \pm 0.07$ |
| $P_{z-}^{inj}$ | $-97.38 \pm 0.07$ | $-89.50 \pm 0.10$ |
| $P_{zz+}^{inj}$ | - | $96.22 \pm 0.38$ |
| $P_{zz-}^{inj}$ | - | $-177.30 \pm 0.61$ |

*Table 4.2: Estimated polarizations for the hydrogen and deuterium atomic beams injected by the ABS into the target. All values are multiplied by 100. The quoted errors take only the uncertainty of the ABS efficiencies into account. The values refer to the polarization of injected gas with 0.3 T guide field. Note that, due to the standard way of defining it, the maximum achievable negative tensor polarization is -200.*

ent types of surface sites are equally distributed. Under normal operating conditions no influence of the HERA beam on the target performance has been observed. Nevertheless certain distinct incidents affecting the cell have been found, when the beam tuning was not optimum or the HERA beam was accidentally lost near the HERMES target region. Possible mechanisms by which the HERA beam could affect the surface properties of the storage cell include:

- desorption of surface coating by a synchrotron radiation flash;
- bombardment of the storage cell walls with charged particles leading to radiation damage;
- chemical reactions of ionized hydrogen or deuterium radicals with the cell surface;
- redistribution of the ice layer on the storage cell by RF heating due to the wake fields;
- contamination of the storage cell surface by sputtered material from the collimator upstream of the target.

Since the exact effect of the HERA beam on the surface properties is unknown, every realistic distribution of recombination and wall relaxation probabilities has to be considered when evaluating the sampling corrections. It is therefore convenient to distinguish certain scenarios of special interest.

- **Homogeneous cell (HC):** the natural assumption when the cell has not been exposed to the HERA beam. The calculated sampling corrections set an upper limit for $\alpha_r$ and $P_a$ for any given values of $\alpha_r^{TGA}$ and $P_a^{BRP}$, respectively.
- **Homogeneous beam tube (HBT):** the beam tube is homogeneously affected by the beam, while the side tubes are unaffected.
- **Inhomogeneous beam tube (IBT):** beam tube is inhomogeneously affected by the beam, while the side tubes are unchanged. This scenario does not lead to a single sampling correction, but it can be used to calculate a lower limit for $\alpha_r$ and $P_a$ for any given values of $\alpha_r^{TGA}$ and $P_a^{BRP}$, respectively.

A model for calculating the sampling corrections has been developed in Ref. [27] which is based on a parameter $\gamma_r(\gamma_d)$, the recombination (spin-flip) probability during a wall collision. If these probabilities were constant and equal for the beam and sample tubes, the sampling corrections would only depend on their geometry. This is actually the case for a freshly installed cell, whose Drifilm coating is known to be intact and uniform.
In all scenarios it is assumed that the relation $\gamma_r^{ST} \leq \gamma_r^{BT}$ holds at any time for the recombination probabilities in the sample tube, $\gamma_r^{ST}$, and beam tube, $\gamma_r^{BT}$. The validity

of this hypothesis is proven by the data [27, 41]. Numerical calculations of the sampling corrections for the "large cell" have been performed using a molecular flow simulation, complemented by analytical calculations based on the one-dimensional diffusion equation [27].
The sampling correction $c_P$ has to be subdivided into two different terms, one for the wall collisions and a second one for spin exchange relaxation, as the two processes have to be treated in different ways. This can be done by defining the depolarization factors $\pi_{wd} = 1 - \Delta P_a^{wd}$ (wall collisions) and $\pi_{se} = 1 - \Delta P_a^{se}$ (spin exchange relaxation) so that, for low spin relaxation, one has:

$$\frac{P_a}{P_a^{BRP}} \equiv c_P \simeq \frac{\pi_{wd}\,\pi_{se}\,P_a^{inj}}{\pi_{wd}^{BRP}\,\pi_{se}^{BRP}\,P_a^{inj}} \tag{4.12}$$

As the spin exchange relaxation occurs in the gas phase, this process is not affected by any change of the cell surface properties, so that the relation between $\pi_{se}$ and $\pi_{se}^{BRP}$ has to be independent from any of the listed scenarios. Moreover, since calculations have shown that $\pi_{se} \simeq \pi_{se}^{BRP}$ [27], one can conclude that the sampling correction $c_P$ is determined by the wall depolarization only:

$$c_P = \frac{P_a}{P_a^{BRP}} \simeq \frac{\pi_{wd}}{\pi_{wd}^{BRP}} \tag{4.13}$$

As an example in fig. 4.1 the effect of the calculated sampling corrections for the "large cell" used in the 1996-97 running with hydrogen is shown. During data taking the measurements of $\alpha_r^{TGA}$ and $\pi_{wd}^{BRP}$ are almost always well above 0.9, so that linear approximations for the sampling corrections can be used:

$$\alpha_r = \bar{a} + (1 - \bar{a})\,\alpha_r^{TGA} \;\; = \;\; \alpha_r^{TGA} + \bar{a}\,(1 - \alpha_r^{TGA}) \tag{4.14}$$

$$\pi_{wd} = \bar{b} + (1 - \bar{b})\,\pi_{wd}^{BRP} \;\; = \;\; \pi_{wd}^{BRP} + \bar{b}\,(1 - \pi_{wd}^{BRP}) \tag{4.15}$$

The values $\bar{a}$, for recombination, and $\bar{b}$, for depolarization, are obtained by taking the average between the two extreme scenarios and assigning them systematic errors $\Delta\bar{a}$, $\Delta\bar{b}$ which are set equal to the differences between the average value and the extremes (see the dotted lines in fig. 4.1).

## 4.5 Evaluation of the systematic error

After having determined all the single terms of eq. (4.1), $P^T$ can be expressed as a function of the measured quantities. It is convenient to write the target polarization in the following way:

$$P^T = \alpha_0\,(\alpha_r + (1 - \alpha_r)\,\beta) P_a = \alpha_{tot} \cdot P_a. \tag{4.16}$$

where the term $\alpha_{tot}$ is called *effective* atomic fraction.

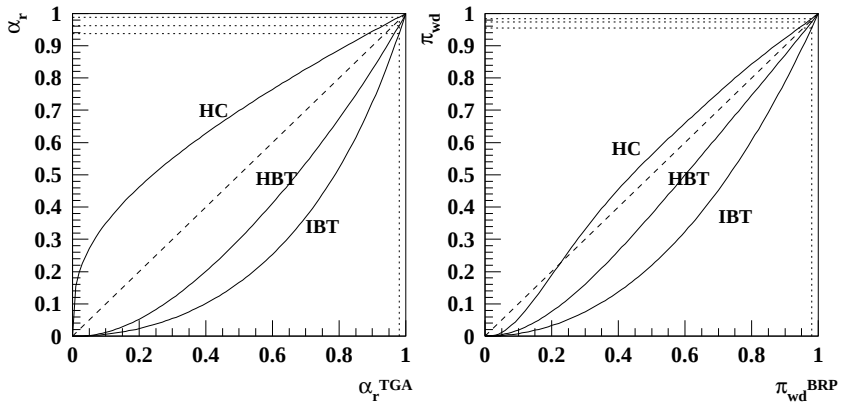


*Figure 4.1: Correlation between the values measured by the TGA or BRP detectors and their corresponding density weighted average values in the storage cell. The left figure shows the range for recombination, the right picture shows the range for wall depolarization. Acceptable uncertainties of $\alpha_r$ and $\pi_{WD}$ can only be achieved with $\alpha_r^{TGA}$ and $\pi_{WD}^{BRP}$ close to unity. The uncertainty grows rapidly with increasing recombination or depolarization respectively.*

### 4.5.1 Error of the effective atomic fraction $\alpha_{tot}$

Combining equations (4.16), (4.14) and (4.6), $\alpha_{tot}$ can be expressed by

$$\alpha_{tot} = \frac{\phi_a + (\bar{a}\,(1-\beta)+\beta)(\phi_m - \phi_{bal} - \phi_{rg})}{\phi_a + \phi_m + (\sqrt{2}-1)\phi_{bal} + (2\sqrt{2}-1)\phi_{rg}}. \tag{4.17}$$

The systematic uncertainty of $\alpha_{tot}$ is determined by the measured flow rates $\phi_a$, $\phi_m$, $\phi_{bal}$ and $\phi_{rg}$ and their errors as well as the values and uncertainties of $\beta$, $\bar{a}$ and the TGA calibration constant $\kappa$. With the matrix $T$ defined by

$$T = \left( \frac{\partial \alpha_{tot}}{\partial \phi_i}, \ldots, \frac{\partial \alpha_{tot}}{\partial kappa} \right), \tag{4.18}$$

and the diagonal covariance matrix $C$ of all calibration constants, the systematic uncertainty $\Delta_{sys}\alpha_{tot}$ is given by

$$\Delta_{sys}\alpha_{tot} = \sqrt{TCT^T}. \tag{4.19}$$

The matrix $T$ contains 10 independent derivatives, i.e. for $\kappa$, $\bar{a}$, $\beta$ and the terms related to the ballistic flux and rest gas calibrations (7 additional terms as described in Ref. [21]).

### 4.5.2 Error of the atomic polarization $P_a$

Combining equations (4.12) and (4.15), and using the approximation:

$$\pi_{se}^{BRP} \simeq \frac{1}{1+\Delta(P_a^{se})^{BRP}}, \tag{4.20}$$

the formula for the average atomic polarization $P_a$ can be written in the following way

$$P_a = P_a^{BRP} + \bar{b}\,(\pi_{se}\,P^{inj} - P_a^{BRP}) \simeq P_a^{BRP} + \bar{b}\left(\frac{P^{inj}}{1+\Delta P_a^{se}} - P_a^{BRP}\right). \tag{4.21}$$

For the calculation of the systematic uncertainty $\Delta_{sys}\,P_a$, the important error sources to be included are $\Delta\bar{b}$ and $\Delta_{sys}\,P_a^{BRP}$[1]. As a result, one finds:

$$\Delta_{sys}P_a = \left((1-\bar{b})^2(\Delta_{sys}P_a^{BRP})^2 + (1-\pi_{wd})^2\pi_{se}^2(P^{inj})^2\Delta\bar{b}^2\right)^{1/2}. \tag{4.22}$$

During the analysis one typically averages over a large dataset, so that the statistcal uncertainty of the polarization measurement $\Delta_{sta}\,P_a$ is negligible.

[1]The uncertainties on $\Delta P_{se}$ and on $P_a^{inj}$ are negligible.

# Chapter 5

# Performance

In the present section an overview is given about the target performance in the running period 1996-2005 will be given by analyzing distinct periods for each different target:

- 1997 for the longitudinal hydrogen target;
- 2000 for the longitudinal deuterium target;
- 2002 for the transverse hydrogen target;
- 2003/2004 for the transverse hydrogen target;
- 2005 for the transverse hydrogen target;

## 5.1 Longitudinal hydrogen running in 1997 (March 1997 - October 1997)

The upper plot in fig. 5.1 shows the atomic fraction $\alpha^{TGA}$ measured by the target gas analyzer during the 1997 running period. The atomic (nuclear) polarization measured by the BRP is plotted in the lower half of fig. 5.1. Aside from startup problems, the target performance was relatively smooth. Unfortunately, a severe HERA beam loss close to the HERMES region occurred at a certain point (left line), resulting in a change of the cell surface properties. After this bad event, it was decided to collect a set of data at higher temperature ($T_{cell} = 260\,\mathrm{K}$ instead of the nominal value $T_{cell} = 100\,\mathrm{K}$) in order to measure the $\beta$ parameter (see Ref. [25]). At the end of this period, the storage cell was exchanged (middle line). Also the second cell experienced a beam dump (right line) which produced a small hole in the cell wall.
For these reasons during the analysis, the 1997 dataset has been divided into four periods during which the cell surface condition was assumed to be constant. For each period, specific studies have been performed to limit the errors on $\alpha_r$ and $P_a$ [41].

For the entire running period with hydrogen, we quote a luminosity-weighted average value for the target polarization of $P^T_{z+} = -P^T_{z-} = 0.852 \pm 0.033$ and a density of $7.6 \times 10^{13}$ nucl./cm$^2$ . The latter number has been derived from a method exploiting the density dependence of spin exchange collisions [27].

## 5.2 Longitudinal deuterium running in 2000 (January 2000 - October 2000)

Over the eight month of deuterium running in 2000, the HERMES target operated under very stable conditions. The atomic beam source, equipped with a microwave dissociator, experienced only one major failure which hardly affected the data taking. Neither the scattering chamber, nor the TGA/BRP vacuum system had to be opened, leading to constant amounts of residual gas in the storage cell as well as stable efficiencies of the detectors monitoring the target. There was no need to replace the storage cell, as its performance in terms of atomic recombination and nuclear depolarization was always excellent. The reason for such good behavior can be found both in a particularly fortunate Drifilm coating and in the limited damage caused by a very well tuned electron beam, i.e. no unwanted beam losses in the vicinity of the target.
The outstanding performance of the HERMES target in this period is well represented in fig. 5.2 (note the change in scale compared to fig. 5.1). The stable behavior of the cell surface in terms of atomic recombination is demonstrated in the upper plot of fig. 5.2, where the atomic fraction measured by the target gas analyzer is plotted. The lower plot shows the nuclear polarization. In the period between January and June 2000, the target was operated with only positive and negative states of nuclear vector polarization. From July on, a new injection mode combining vector and tensor polarization $P_{z+}$, $P_{z-}$, $P_{zz+}$ and $P_{zz-}$ was established in order to perform the first measurement of the tensor-polarized structure function $b^d_1$.

The average values for the four polarization states used in 2000 are the following:

$$P^T_{z+} = +0.851 \pm 0.029 \quad (5.1)$$
$$P^T_{z-} = -0.840 \pm 0.026 \quad (5.2)$$
$$P^T_{zz+} = +0.891 \pm 0.027 \quad (5.3)$$
$$P^T_{zz-} = -1.656 \pm 0.049 \quad (5.4)$$

Note that only the systematic uncertainty is quoted as the statistical uncertainty is negligible in comparison. The differences between the systematic uncertainties originate from the injection mode dependent systematic error of the atomic polarization.
The measured target density for this period, measured by means of the spin-exchange collision relaxation method, is $2.1 \times 10^{14}$ nucleons/cm$^2$.

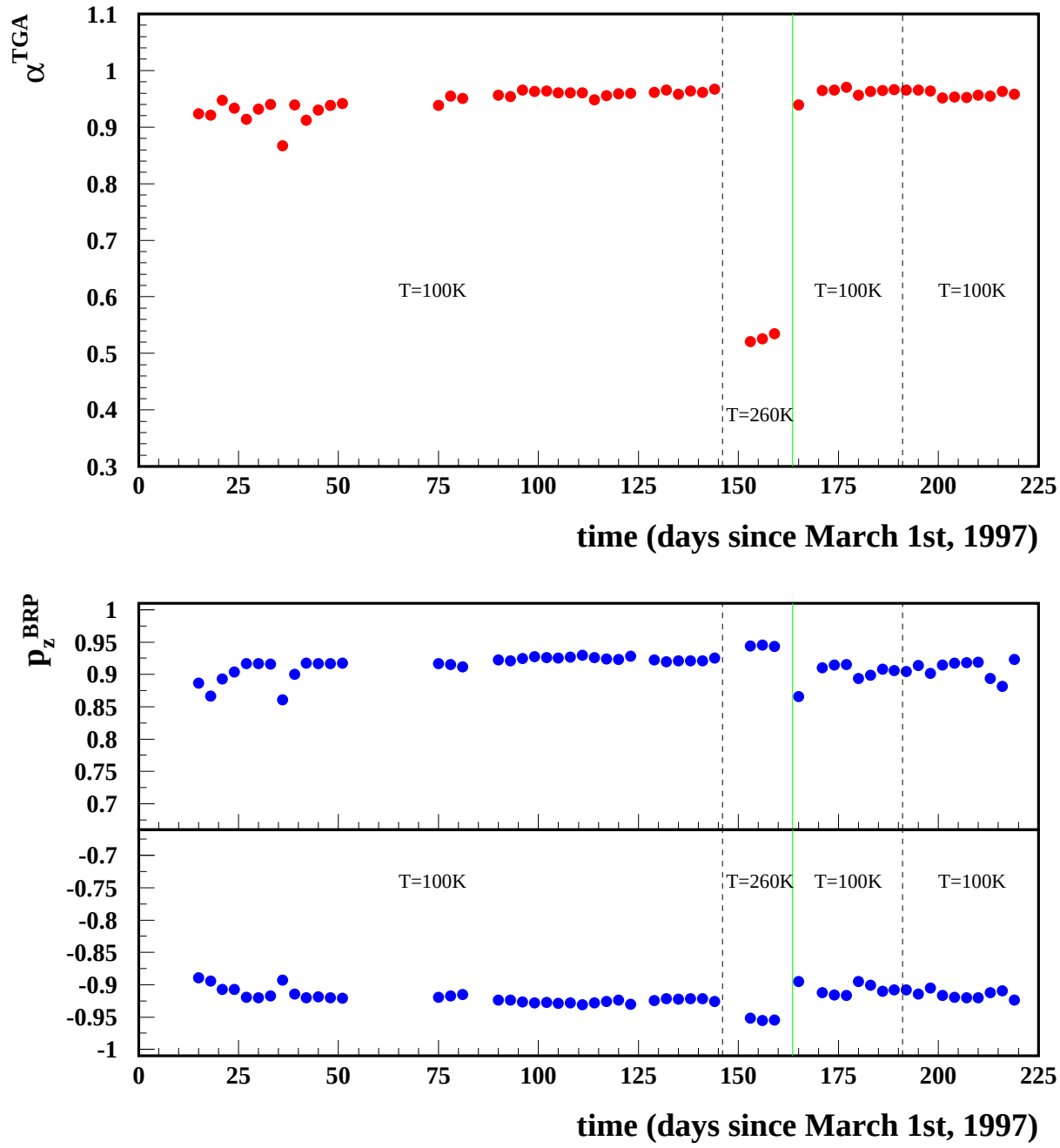


*Figure 5.1: The TGA (above) and BRP (below) measurements for the entire 1997 data taking period. The vertical dashed lines indicate HERA beam loss events which affected the cell surface properties, and the solid line indicates the replacement of the target cell.*

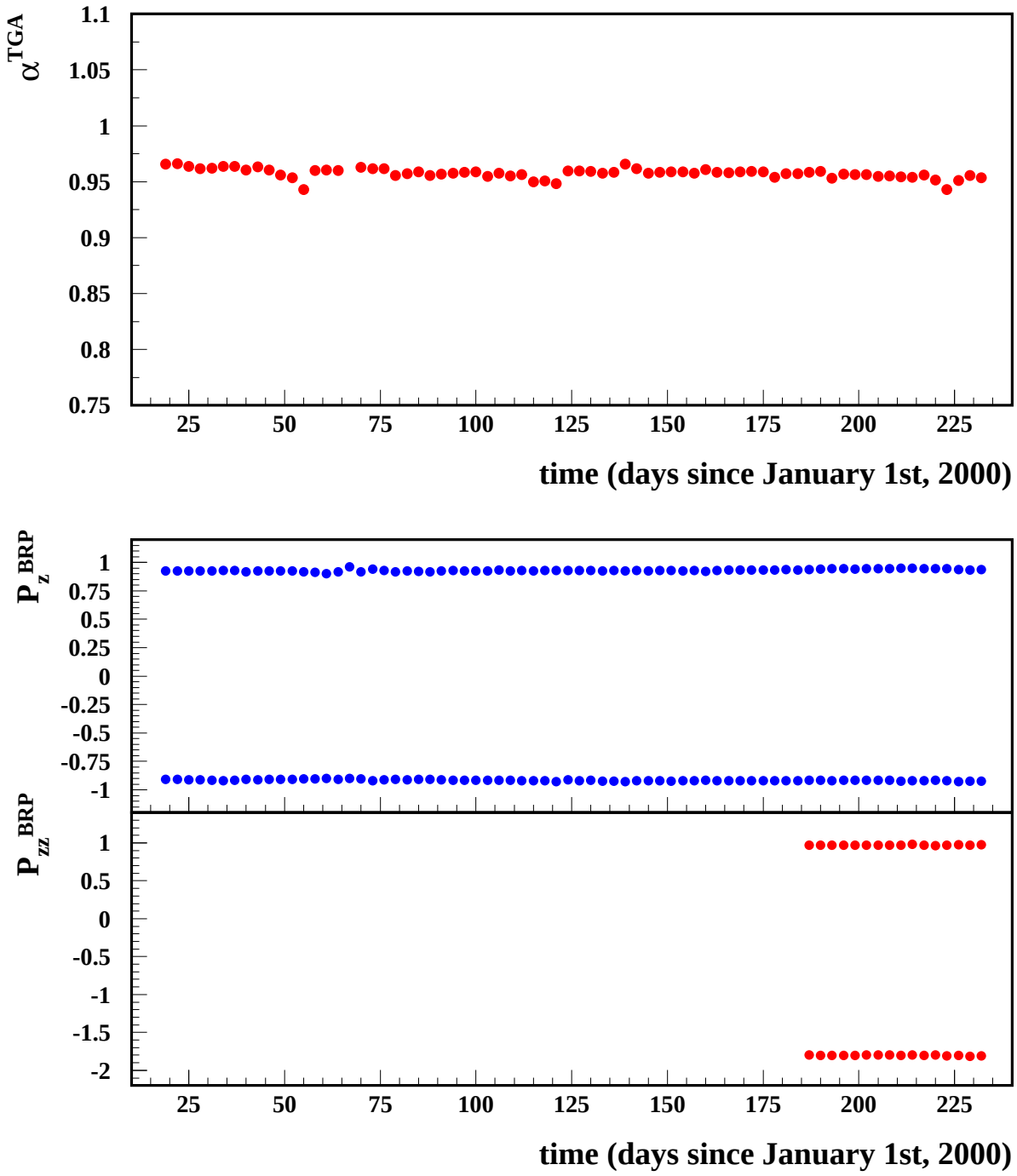


*Figure 5.2: Atomic fraction, $\alpha^{TGA}$ upper plot, and vector/tensor polarization, $P^{BRP}$ lower plots, measured by TGA and BRP respectively during the year 2000 running period. Each symbol represents data averaged over a 72 hours bin. The absolute bin averaged values are always above 0.9. The tensor polarization (lower plot) was employed from July on.*

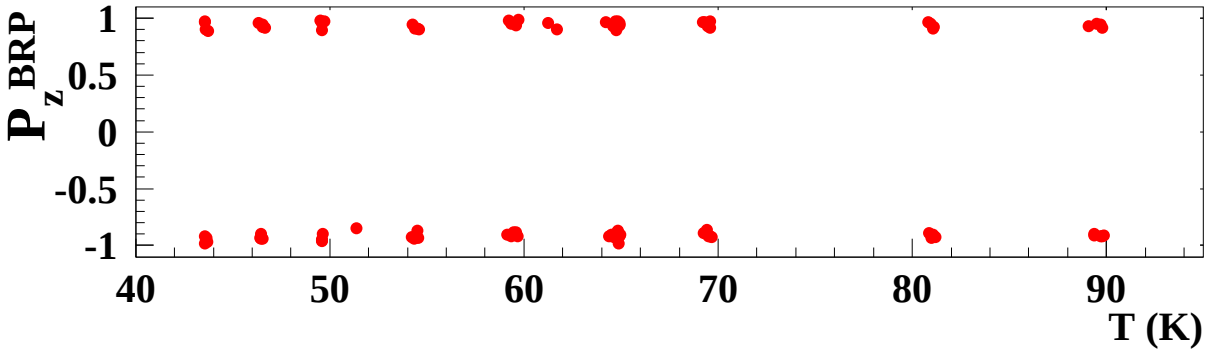


*Figure 5.3: Nuclear vector polarization $P_z^{BRP}$ as function of the cell temperature T measured in August 2000. No dependence on the temperature is observed. The operating temperature of the target during data collection was 60 K.*

### 5.2.1 Spin relaxation

The spin-flip probability per wall collision $\gamma_z$ is proportional to $\tau_s^2$, $\tau_s$ being the mean residence time: $\tau_s = \tau_0\, e^{\left(\frac{E_b}{kT}\right)}$ (see eq. 3.1). Therefore $\gamma_z$ depends on the wall temperature $T$. In other words: if $P_a^{BRP}$ does not change with $T$, wall depolarization effects are vanishingly small within the experimental errors. In fig. 5.3, a scan of the cell temperature down to very low temperatures is shown. The result indicates that no wall depolarization occurs. As a consequence, for the deuterium target the sampling correction for nuclear depolarization equals unity ($c_P = 1$), so that:

$$P_a = P_a^{BRP}. \tag{5.5}$$

Moreover, the calculated depolarization due to spin exchange collision resulted in $\Delta P_a^{se} = 0.3\,\%$. As in 2000 spin relaxation can be neglected completely, the polarization injected by the ABS equals the measured BRP value:

$$P_a^{inj} \simeq P_a^{BRP}. \tag{5.6}$$

### 5.2.2 Recombination

Although the atomic recombination is a strongly temperature dependent process, no variation of the measured atomic fraction $\alpha^{TGA}$ over a very wide temperature range around the working point $T_{cell} = 60\,\mathrm{K}$ was ever observed during the whole year. Figure 5.4 (upper plot) reports a cell temperature scan performed in August. (For comparison a temperature scan performed with hydrogen in 1997 is also shown in the lower plot of the same

figure). Additionally the measurement of the fraction of atoms surviving recombination, $\alpha_r^{TGA}$, yielded the following average value:

$$\alpha_r^{TGA} = 0.997 \pm 0.014, \tag{5.7}$$

confirming that within the measured uncertainty no evidence was found for contributions from recombined molecules. Therefore, for the deuterium data taking period in 2000 both the sampling correction $c_\alpha$, and the impact of the uncertainty on $\beta$ are negligible.

## 5.3 Transverse hydrogen running in 2002 (August 2002 - February 2003)

During the 2002-2003 data taking period the HERMES transversely polarized hydrogen target worked in a very stable way. On the other hand, the poor performance of the HERA beam did not allow a detailed study of the bunch induced depolarization. Nevertheless, by scanning the target magnetic field a working point has been established where the loss of polarization due to the field non-uniformity was limited to 1.5 % at the highest available beam currents (25 mA). The average target polarization, $(P_{z+}^T - P_{z-}^T)/2$, during the 2002 data taking period was $0.783 \pm 0.041$. This value is lower than that reported for the longitudinal hydrogen target (Section 6.1) mainly due to the lower applied target holding field.
The stability of the transverse target operation during the 2002 running period is illustrated in fig. 5.5. The target density in this running period measured via spin-exchange collision was $1.1 \times 10^{14}$ nucl./cm$^2$.

## 5.4 Transverse hydrogen running in 2003/2004 (October 2003 - June 2004)

Between Febrary 2003 and October 2003, there was a long shut-down and during this time a new target cell was installed.
The target performance was since the beginning very good. From fig. 5.6 one can see, how the value of the polarization is costant and high; up to the end of the year the average polarization was $0.795 \pm 0.033$. The reason for such good behavior can be found both in a particulary fortunate Drifilm coating and in the limited damage caused by a very well tuned electron beam, i.e. no unwanted beam losses in the vicinity of the target.
The same target cell was in also during the whole 2004 data taking period. In April 2004 the target-cell was warmed up and the beam-line vented in order to allow the alignment of the DVC chambers back to their original location. The warming up to room tempereture the target cell implies the complete loss of the ice layer covering the cell surface and inhibiting nuclear depolarization as well as atomic recombination. It took almost 2

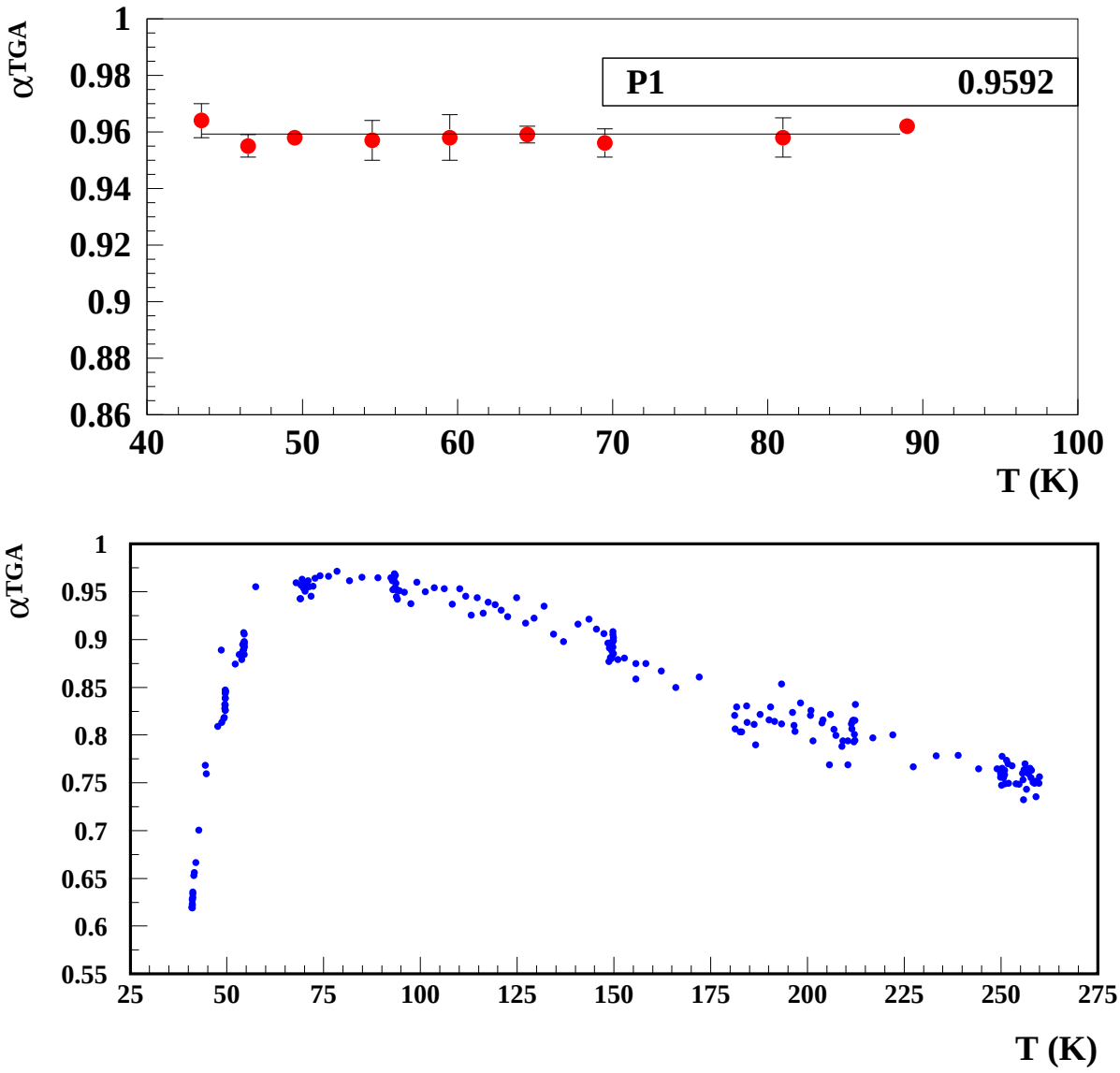


*Figure 5.4: Upper plot: measured atomic fraction as a function of the cell temperature for $T_{cell} < 100\,K$ for the deuterium running in 2000. No dependence on the temperature can be seen. The working point during data taking was set to $T_{cell} = 60\,K$. For comparison a temperature scan with hydrogen taken in 1997 is shown in the lower plot.*

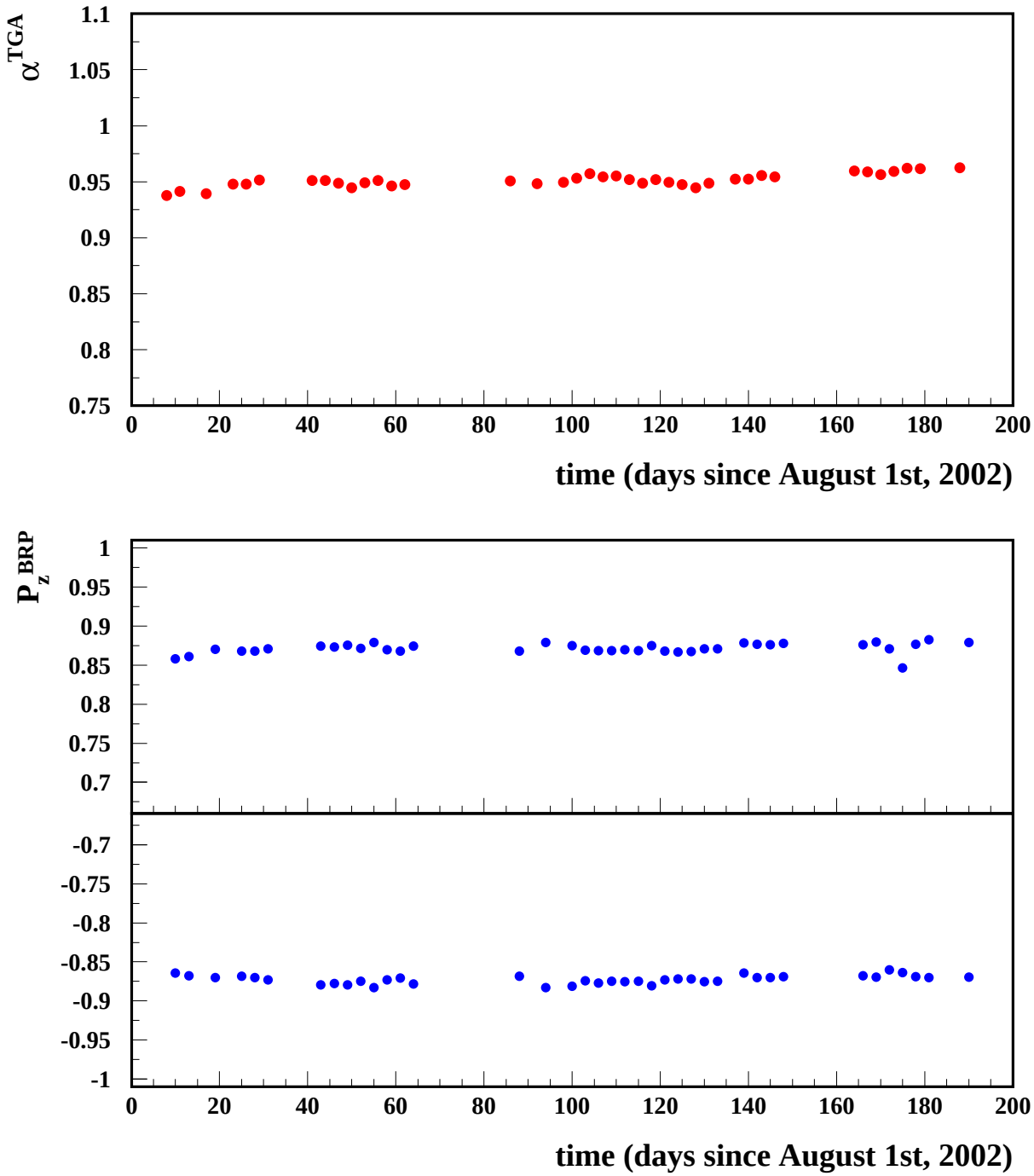


*Figure 5.5: The TGA (above) and BRP (below) measurements for the 2002/03 data taking period.*

| Years | Target | $DIS/milion$ |
|---|---|---|
| 1996-97 | $H_{\|\|}$ | 3.5 |
| 1998-2000 | $D_{\|\|}$ | 10.2 |
| 2001-2005 | $H_{\perp}$ | $\approx 6$ |

*Table 5.1: Deep inelastic scattering events collected with the different polarized targets. The number are given in millions.*

mounths to have the previous value of the polarization.
In figure 5.6 is reported the polarization over the 2004. For the first period the polarization is costant to the value $0.777 \pm 0.039$, just after the venting the polarization is dropped to $0.648 \pm 0.090$ and slowly recoverd.

## 5.5 Transverse hydrogen running in 2005 (January 2005 - November 2005)

In November 2004 HERA changed from positron to electron. Due to technical problems the data acquisition started only the $1^{st}$ of January 2005. During the time between the installation and the start of the data taking, the target cell experienced a lot of warming up due to problems with the cryo system. The performance of the target were compromised so that in April 2005 it was decided to exchange target cell. The different behaviour between the two cell emerges from figure 5.7.
After the usual time to reach the standard operation the second cell performed in a very stable way. The period of data taking with the second cell was caracterized by a beam dump and for this reason diveded in two period, as reported in figure 5.7. During the second period a mistake by an operator caused a partial venting of the target chamber which damaged the cell coating and effected the performace of the target for one week[1] the performance of the target were lower than usual for a week.

## 5.6 Resume'

Table 5.2 and 5.3 summarize averaged values for the target properties during the various running periods.

[1]This happened when, by mistake the ABS was vented. The interlok closes the separation valve between the ABS and the target chamber in case the pressure into the ABS is too high. If the ABS is vented the interlok has a delay of few milliseconds to close the valve, and this is enough to blow away the ice coating. Note that the pressure into the target chamber when the ABS is operational is $10^{-7} mbar$, the ABS is normally vented to atmosferic pressure (1013 mbar) by flowing $N_2$

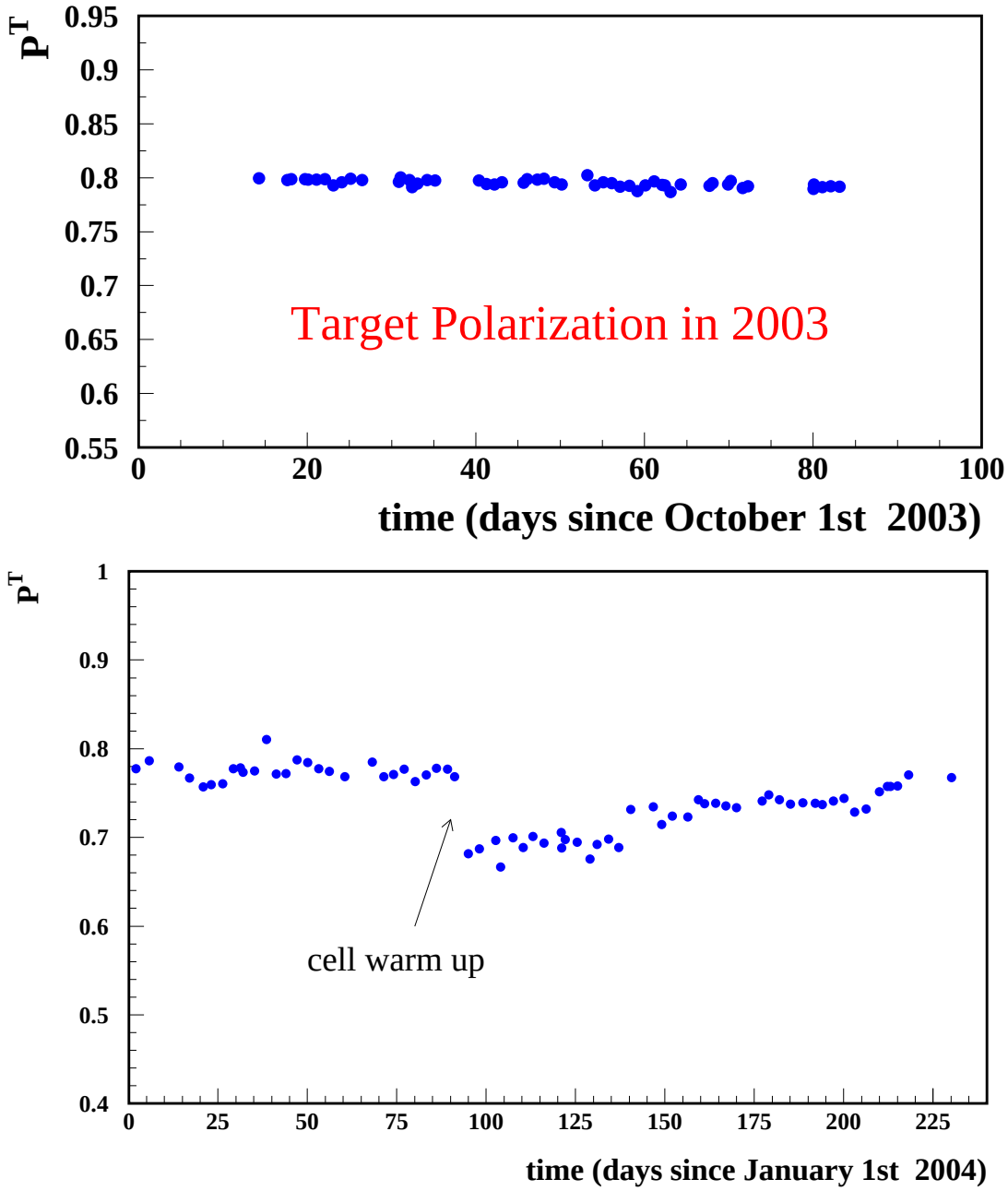


*Figure 5.6: Upper plot: the final value of polarization for the 2003/04 data taking period. Lower plot: the final value of polarization for the 2004 data taking period. The drop of the polarization after 92 days is due to the venting of the cell. The point indicate that the polarization was constant to the value of 0.777 for all this period.*

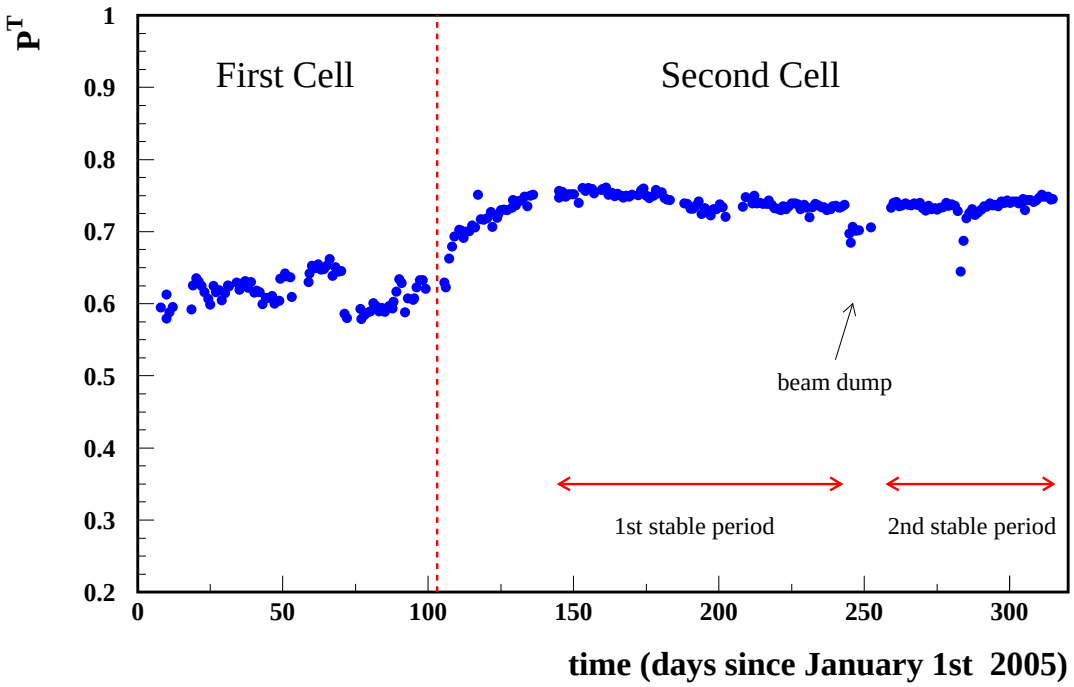


*Figure 5.7: The final value of polarization for the 2004/05 data taking period.*

| target/year | $H_{\|\|}(1997)$ | $D_{\|\|}(2000)$ |
|---|---|---|
| $P_t$ | $0.851 \pm 0.033$ | $0.845 \pm 0.028$ |
| $\Delta\alpha_r$ | 0.055 | **0.003 (absent)** |
| $\Delta P_{SE}$ | 0.035 | $\leq 0.001$ |
| $\Delta P_{WD}$ | 0.02 | $\leq 0.01$ |
| $\Delta P_{BI}$ | **absent** | **absent** |
| $t$ $(10^{14} nucl/cm^2)$ | 0.7 | 2.1 |
| FOM $(P_t^2 t)$ | 0.5 | 1.5 |

*Table 5.2: Summary of the HERMES target performance in the years 1997 and 2000. The tabulated values are averaged over the respective running periods. For a complete description for each period see into the text.*

| target/year | 10/2003<br>03/2004 | 04/2004<br>07/2004 | 01/2005<br>04/2005 | 04/2005<br>11/2005 |
|---|---|---|---|---|
| $P_t$ | $0.786 \pm 0.036$ | $0.721 \pm 0.059$ | $0.62 \pm 0.09$ | $0.73 \pm 0.06$ |
| $\Delta\alpha_r$ | **absent** | **absent** | *0.24* | 0.035 |
| $\Delta P_{SE}$ | 0.035 | $\leq 0.001$ | 0.055 | 0.055 |
| $\Delta P_{WD}$ | 0.055 | *0.12* | *0.17* | *0.12* |
| $\Delta P_{BI}$ | $\leq 0.01$ | $\leq 0.01$ | $\leq 0.01$ | $\leq 0.01$ |
| $t$ $(10^{14} nucl/cm^2)$ | 1.1 | 1.1 | 1.1 | 1.1 |
| FOM $(P_t^2 t)$ | **0.7** | 0.6 | *0.4* | 0.6 |

*Table 5.3: Summary of the HERMES target performance in the years 2003, 2004 and 2005. The tabulated values are averaged over the respective running periods. For a complete description of each data taking period see text.*

A comparison between the longitudinally polarized hydrogen and deuterium target leads to the following conclusions. At the same guide field, in case of deuterium the spin exchange and wall relaxation processes are suppressed by a factor $(B_C^H/B_C^D)^2 \simeq 20$ compared to hydrogen. The positive and negative $P_z$ values for hydrogen coincide very well, while for deuterium there is a clear difference. This is due to the higher number of efficiencies and transmissions involved.

From the table it is possible to deduce the departures from the optimal performance like the amount of recombination ($\Delta\alpha_r = 1 - \alpha_r$), and the depolarization due to the different depolarizing mechanisms: spin-exchange collisions ($\Delta P_{SE}$), wall-depolarization ($\Delta P_{WD}$) and beam-induced fields ($\Delta P_{BI}$). The target density integrated over the cell length or areal density $t$ is also shown together with a relative factor of merit (FOM) which takes into account both the polarization and the density. It is worthwhile to mention again that in 1997 the target cell had a larger cross-section (29 mm $\times$ 9.8 mm) implying a higher conductance and a correspondingly lower density (about 40 %). The table also illustrates once more the optimal performance of the $D_{||}$ target in 2000. For this target no recombination ($\Delta\alpha_r = 0$) and no depolarization phenomena ($\Delta P_{WD} = \Delta P_{SE} = \Delta P_{BI} = 0$) have been observed. This excellent behavior has to be attributed to the lower critical field of deuterium (11.7 mT) compared to hydrogen (50.7 mT), and to an improvement in the knowledge and preparation of the cell surface coating. The improved surface coating is also responsible for the better performance of the 2002 $H_\perp$ target compared to the 1997 $H_{||}$ target, as far as the amount of recombination is concerned.

On the other hand, in 2002, due the higher density obtained and the higher number of wall collisions, spin-relaxation effects are more important causing a loss in polarization of about 11 %, thus limiting the gain in the factor of merit with respect to the 1997 running due to the increase in density. This indicates how an enhancement in the figure of merit of the target might be obtained by increasing the holding field proportionally

with the density, in order to limit the spin relaxation effects. The number of deep inelastic scattering events (after data quality cuts) collected with the different polarized targets is given in tab. 5.1.

# Chapter 6

# Measurement of spin-exchange collision cross section in the low temperature region

## 6.1 Introduction

The first studies on the cross section of the spin-exchange collision process have been performed in connection to astrophysics [66]. The interstellar space is filled with extremely tenuous clouds mainly composed by hydrogen. The hyperfine state of an hydrogen atom in the ground state can be changed by a collision with another atom. Switching from the triplet to the singlet configuration an hydrogen atom emits radio-waves with the characteristic frequency of 1420 MHz: tuned to this frequency radio telescopes have mapped the distribution of neutral hydrogen in the space.
Although a few theoretical papers devoted to the calculation of the spin-exchange collision cross section have been published [66, 68, 70], till now only one measurement have been performed [75]. The measurement agrees quite well with the theoretical estimation in the temperature range between 80 K and 363 K, where the cross section is almost constant.
The present chapter describes the measurement which has been performed by the HERMES target in between the normal running devoted to the data taking of the HERMES spectrometer.
Previously to the work which will be presented here, no measurement existed in the temperature region below 80 K where the cross section is predicted to show a strong temperature dependence. The HERMES target offered unique experimental conditions to extend the measurement of the spin-exchange collision cross section down to the temperature of 40 K:

a) it has the possibility to change the hydrogen temperature in the range between 40 K and 100 K, by varying the temperature of the storage cell;

| $\sum_i m_F$ | Hydrogen |
|---|---|
| 2 | $\|1\rangle,\|1\rangle$ |
| 1 | $\|1\rangle,\|2\rangle \leftrightarrow \|1\rangle,\|4\rangle$ |
| 0 | $\|1\rangle,\|3\rangle \leftrightarrow \|2\rangle,\|4\rangle \leftrightarrow \|2\rangle,\|2\rangle \leftrightarrow \|4\rangle,\|4\rangle$ |
| $-1$ | $\|2\rangle,\|3\rangle \leftrightarrow \|3\rangle,\|4\rangle$ |
| $-2$ | $\|3\rangle,\|3\rangle$ |

*Table 6.1: Pairs of hyperfine states of hydrogen, for which spin exchange collisions are allowed by angular momentum conservation.*

b) it offers the chance of injecting in the cell any desired combination of hyperfine states allowing to select the most sensible to the effect of the spin-exchange collision;

c) it allows the detection of the population of the hyperfine states present in the cell and to directly measure the amount of depolarization induced by the spin-exchange collision;

d) finally, fundamental for a quantitative estimation of the cross-section, it gives the possibility to determine with high precision the absolute gas density inside the storage cell.

The chapter is organized as follows: after a brief description of the theoretical calculation of the spin-exchange collision cross section in sec. 6.2, section 6.3 will resume the issue of spin-relaxation in a storage cell and present the principle of the measurement. The final results and the conclusions will be presented in section 6.4

## 6.2 Theoretical estimations of the spin-exchange collision cross section

The hyperfine states of two atoms colliding with each other in the gas phase can be modified via interaction between the electron spins [66]. The initial spin state of the separated atoms can be expressed as a superposition of singlet and triplet electronic spin state of the molecule, multiplied by the nuclear spin functions. The effect of a collision is to bring a relative phase shift, $\phi_{ts}$, between the amplitude of the singlet component and the amplitudes of the triplet components of the electron spin function. The phase shift $\phi_{ts}$ can be expressed by:

$$\phi_{ts} = \int \frac{V_t - V_s}{\hbar} \cdot dt \tag{6.1}$$

where $V_t$ is the energy of the triplet ('repulsive') electronic state, $V_s$ is the energy of the singlet ('attractive') state, and the integration extends over the whole duration of the

collision. The phase shift $\phi_{ts}$ depends both on the impact parameter $b$ and the energy of the incident particle. At a given energy the total spin exchange cross section is given by:

$$\sigma_{se} = 2\pi \int_0^\infty sin^2(\frac{1}{2}\phi_{ts})b \cdot db = \pi \int_0^\infty (1 - cos\phi_{ts})b \cdot db \tag{6.2}$$

The first calculation was made by Purcell and Field in 1956 [66] who, by using the potential curves calculated by Hirschfelder in 1954 [67], obtained the results shown in figure 6.1 (dotted line). In 1972 Allison performed the same calculation, using new potential energy curves [69], and introducing the energy of the electron - nucleon coupling. In fact depending on the colliding atoms, the total parity of the system can be $-1$ or 1. The spin-exchange process is then described by two different cross section:

- $\sigma^-$ when the parity of the system is $-1$;
- $\sigma^+$ when the parity of the system is 1;

A later calculation was performed in 1985 by Swenson, Tupa and Anderson [70]: they used different potential curves [71]. All the calculation are plotted in figure 6.1.

## 6.3 Measurement with the HERMES Target

### 6.3.1 Principle of the Measurement

In the collision between two atoms in the gaseous phase the total angular momentum is conserved and the sum of the magnetic quantum numbers $m_F$ before and after have to be the same:

$$\Delta \sum_i m_F = 0. \tag{6.3}$$

Table 6.2 reports the allowed hyperfine transitions for any given pair of colliding hydrogen atoms. One can see for example that if an initial population of the gas consists only of pure states $|\,1\,\rangle$ or $|\,3\,\rangle$ in case of hydrogen, no relaxation by means of spin exchange is possible. Reminding the definition of nuclear polarization (see appendix A, formula A.17) one can see that the collisions between atoms can drive a loss of nuclear polarization of the atoms themselves. In the case of the HERMES target a dedicated device was available for the direct measurement of the atomic polarization: the Breit-Rabi polarimeter. By detecting the amount depolarization caused by spin-exchange collision it has been possible to derive the cross-section.

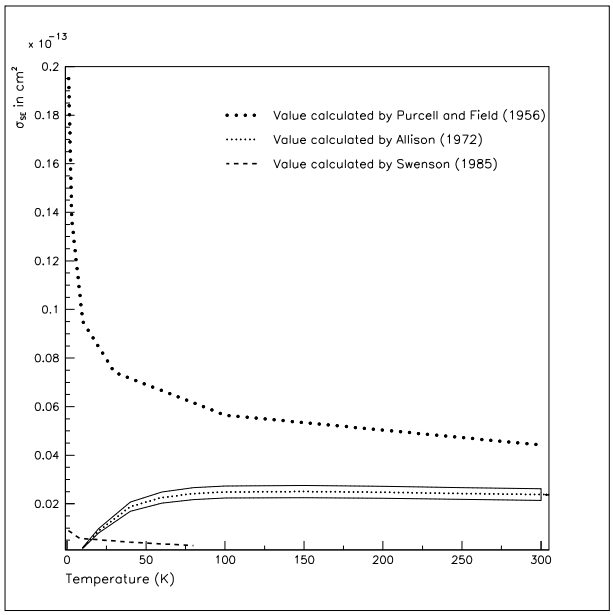


*Figure 6.1: Theoretical calculation. The two line for the Allison calculation are the errors given by the author for this calculation.*

| Injected | Collision | $\Delta P_z$ | $\sigma_{se}$ |
|---|---|---|---|
| $\|1\rangle, \|4\rangle$ | $\|1\rangle, \|1\rangle$ | no | $\sigma^+$ |
| | $\|1\rangle, \|4\rangle$ | $\surd$ | $\sigma^-$ |
| | $\|4\rangle, \|4\rangle$ | $\surd$ | $\sigma^+$ |
| $\|2\rangle, \|3\rangle$ | $\|3\rangle, \|3\rangle$ | no | $\sigma^+$ |
| | $\|2\rangle, \|3\rangle$ | $\surd$ | $\sigma^-$ |
| | $\|2\rangle, \|2\rangle$ | $\surd$ | $\sigma^+$ |

*Table 6.2: Pairs of hyperfine states of hydrogen, for which spin exchange collisions are allowed by angular momentum conservation.*

Ref. [27] shows that the loss of polarization caused by the spin exchange collision in a storage cell can be linked to the spin exchange cross section by the equation:[1]:

$$\sigma_{se} = \frac{\sqrt{2}\Delta P_{se} \cdot (1 + x^2)}{L_d \langle n \rangle (1 - 2\Delta P_{se})} \tag{6.4}$$

where $\Delta P_{se}$ is the loss of nuclear polarization by spin exchange collision, $x$ is the ratio between the holding field and the hydrogen critical field, $L_d$ is the diffusion length, $\langle n \rangle$ is the average density of the target.
In the following we will explain how all the terms in the formula 6.4 have been derived.

[1] A detailed explanation can be found in appendix D of [27]. The basic assumption used to derive this equation are:

- high holding field;
- absence of wall depolarization;

| $H_2$ Flow $sccm$ | Dissociator Power $Watts$ | Density $atoms/cm^3$ |
|---|---|---|
| 80 | 300 | $3.61 \cdot 10^{12}$ |
| 55 | 200 | $3.03 \cdot 10^{12}$ |
| 45 | 100 | $1.96 \cdot 10^{12}$ |

*Table 6.3: Changing the flow of $H_2$ and the power of the dissociator it was possible to obtain different target density. The HERMES working point is setted to have the higher density. The measurement done to obtain the value of the density is shown in sec. 6.3.4*

### 6.3.2 Measurement of $\Delta P_{se}$

One of the problems to be faced in the measurement of the depolarization caused by spin-exchange collision was the contemporary presence of two relaxation processes: in fact, besides the spin-exchange mechanism, also the wall collision relaxation is active in the cell. The contribution $\Delta P_{se}$ coming from spin - exchange collision has been decoupled from the effect of the wall-collisions by making use of their different density dependence. In particular, while the relaxation due to spin-exchange is density dependent, the contribution to the depolarization by wall-relaxation it is not. In the measurement the target density has been varied by changing the flux injected by the ABS (tab. 6.3): by interpolating the measured polarization with a straight - line and extrapolating the polarization for zero density, the amount of gas depolarization caused by spin - exchange collisions could be inferred.
Figure 6.2 shows the variation of the nuclear polarization as a function of the ABS flux. The net depolarization caused by spin - exchange collision ($\Delta P_{se}$) can be written in the following way:

$$\Delta P_{se} = \frac{(P^{BRP})_0 - (P^{BRP})_1}{P_z^{inj}} \tag{6.5}$$

where $(P^{BRP})_1$ is the atomic polarization measured at nominal density, and the $(P^{BRP})_0$ is the extrapolated polarization for zero density. As mentioned in 4.3 and show in tab. 4.2 the injected polarization are $0.9726 \pm 0.0005$ for $P_z^+$ and $-0.9738 \pm 0.0007$ for $P_z^-$.
To measure $\Delta P_{se}$ the injected hyperfine state were $|1\rangle + |4\rangle$ and $|2\rangle + |3\rangle$, which represent the $P_z^+$ and $P_z^-$ respectively. Table 6.2 shows which kind of collisions are possible depending on the injected states.
This kind of operation was repeated for four different temperatures (40 K, 60 K, 80 K, 100 K). Two complete sets of measurements have been taken. An additional measurement has been taken at 40 K (tab. 6.7).
As a change in the temperature effects the recombination inside the cell, (see on figure 6.3), all the measurement have been corrected by the measured atomic fraction $\alpha_r^{TGA}$, before the fit procedure.

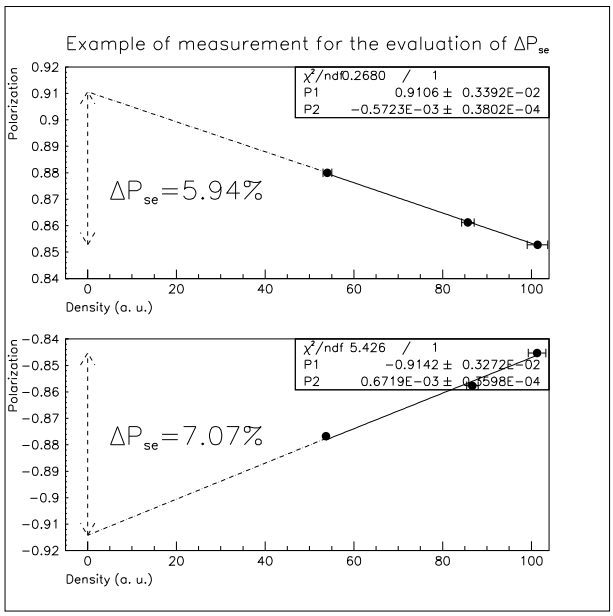


*Figure 6.2: Changing the density (abscissa axis), the nuclear polarization measured (ordinate axis) is different. $(P^{BRP})_0$ is the polarization at zero density. $(P^{BRP})_1$ is the polarization at the higher density and the difference normalized by the nuclear polarization injected is $\Delta P_{se}$. For more detail see the text.*

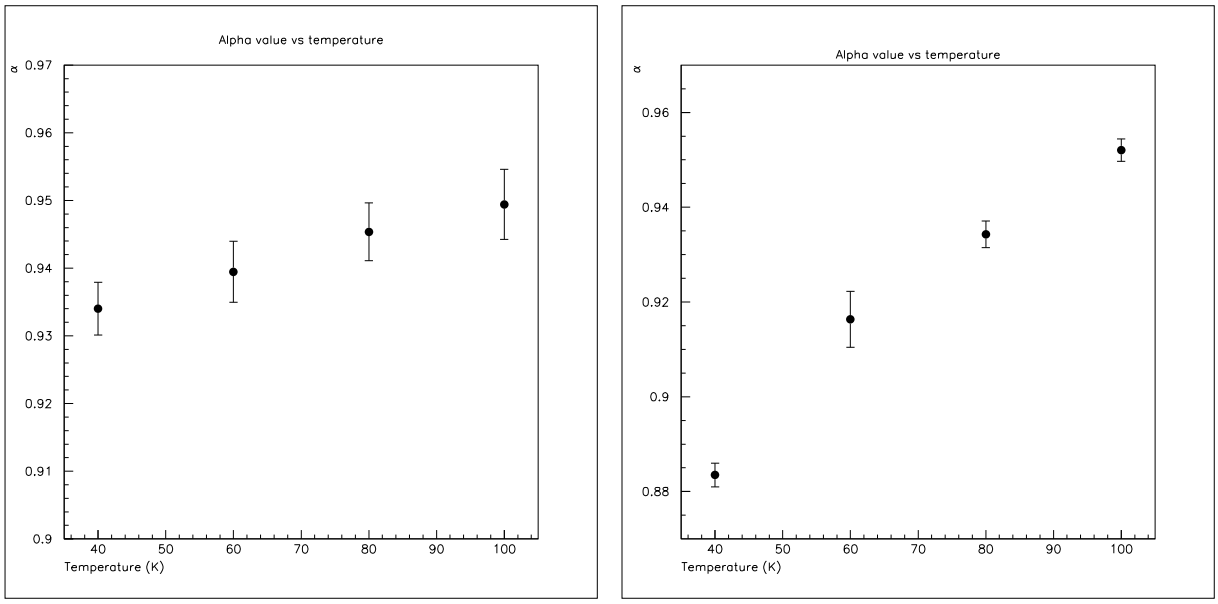


*Figure 6.3: $\alpha$ behavior versus temperature, for the two sets of measurements. The right plot shows a stronger temperature dependence on $\alpha$ this is due by the fact that this set was taken after the beam dump experienced by the cell. 5.7*

### 6.3.3 Molecular Flow Monte Carlo simulations

The simulations presented here have been performed by using a tracking Monte-Carlo program, (B. Braun's McGadyn code [28]) , which has already been used to model processes in the HERMES target cell. The program tracks single particles through a structure with a defined geometry (such as an elliptical storage cell). After each wall collision, the particle is desorbed from the surface with a cosine distribution, and the next collision point is calculated, assuming that the particle moves in a straight line between collisions.

#### Diffusion Length $L_d$

In this work the McGadyn code was used to evaluate the diffusion length of the particles inside the cell ($L_d$ in the formula 6.4). The diffusion length is defined as the integral path from the beginning (the injection tube) up to the end (the extension tube) 6.4.
In [27], using a sample of Deuterium, it was proved that the diffusion length measured and the simulated one by means of the Monte Carlo, differ by less than 0.2%.
To obtain the distribution shown in figure 6.5, 10 millions of particles have been generated and tracked along the cell geometry. Only 5.43% of the generated particles passed through the extension tube.
The plot can be interpreted with reference to the cell geometry as follows:

- no particles have diffusion length shorter than 20 cm, this is exactly the distance given by the sum of injection tube+sample tube+ cell size;
- after that till to the maximum the distribution reflects the Maxwell - Boltzmann thermal distribution of the particles;
- from the maximum to the end it is the diffusive part of the distribution which is the part of interest for the evaluation of the diffusion length.

In order to extract the value of the diffusion length, a fit was performed on the last part of the distribution showed in 6.5. The function used is reported in 6.6 where the coefficients A, B and C are respectively a normalization factor, an offset and the diffusion length. From the fit a value for the diffusion length of (4232.20 $\pm$ 5.99) cm has been determined.

$$y = A \cdot e^{\frac{-x+B}{C}} \tag{6.6}$$

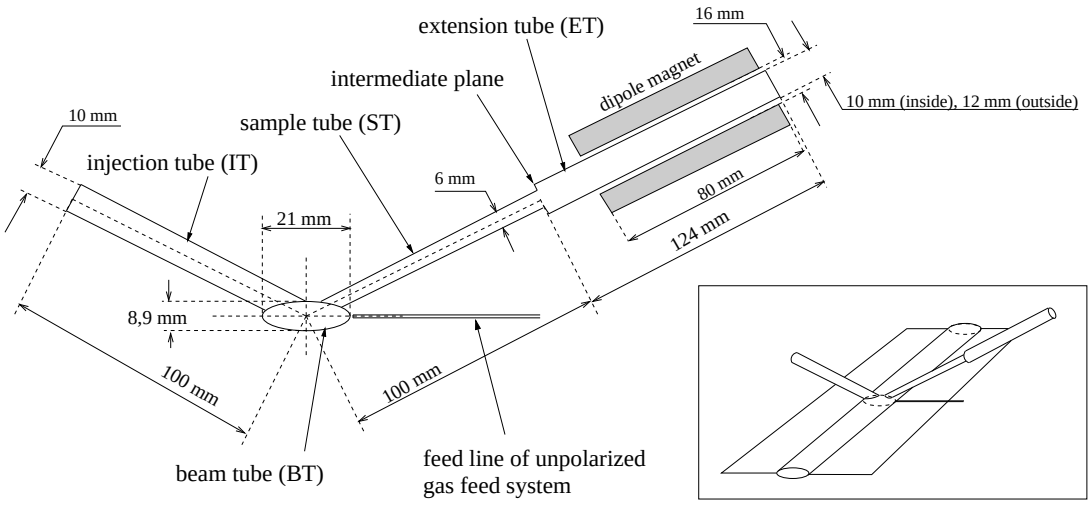


*Figure 6.4: Detailed cell geometry used for the Monte Carlo simulations, with quotation.*

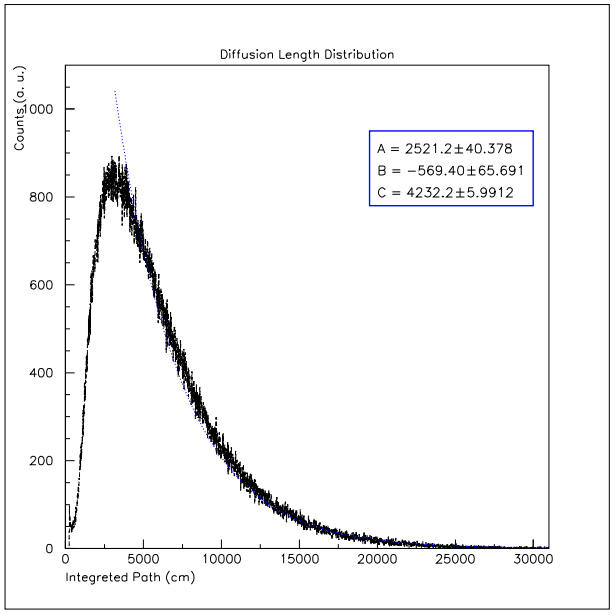


*Figure 6.5: Distribution of the diffusion length obtained by Monte - Carlo simulation generating 10M particles. The black line is the fit using the equation 6.6, for details see text.*

| | $\eta$ | $A$ $cm^2$ | $C$ $cm^3/s$ |
|---|---|---|---|
| *Injection tube* | 0.109 | 0.785 | 3103 |
| *Sample tube* | 0.072 | 0.283 | 738 |
| *Extension tube* | 0.093 | 0.785 | 2646 |
| **Half** *beam tube* | 0.052 | 1.467 | 2765 |

*Table 6.4: All the elements present in equation 6.7 are reported in the table, where the value of the conductance of each element is calculated at 100 K.*

### Cell Conductance

In order to precisely determine the target density an accurate knowledge of the cell conductance is requested. As the available analytical formula for the calculation of the conductances have low precision ($> 10\%$) a Monte Carlo code has been used to evaluate the cell conductance. In particular, the already mentioned McGadyn code, was used also for this purpose.
To simulate the conductance of a vacuum duct, the basic assumptions are [79]:

- the flow is steady;
- the distribution of the position and angle at which a particle enters the pipe at an opening is independent of the flow in other parts of the system;
- the molecules in the pipe move independently of each other, i. e., there are no intermolecular collision in the pipe.

With these assumptions the particles can be traced individually from the entrance to the exit. For the HERMES geometry the entrance is the *injection tube*, the exits are the two ends of the cell and the *extension tube*.
The transmission probability $\eta$ has been computed dividing the number of particles exiting through the ends aperture by the total number generated at the entrance. The conductance $C$ of the pipe is then given by:

$$C = \frac{\eta\, v}{4} A, \tag{6.7}$$

$v$ is the thermal velocity of the gas and $A$ the cross section of the pipe.
To calculate the conductance of the HERMES cell, the transmission probability of each elements was calculated. The *extension tube* and the *sample tube* were added in series to obtain the equivalent conductance, and then added in parallel to the *injection tube* and the two half part of the *beam tube*:

$$C^{Tot} = 2 \cdot C^{BeamTube} + C^{Inj.Tube} + \frac{C^{Ext.Tube} \cdot C^{Sam.Tube}}{C^{Ext.Tube} + C^{Sam.Tube}} \approx 9110 cm^3/s \tag{6.8}$$

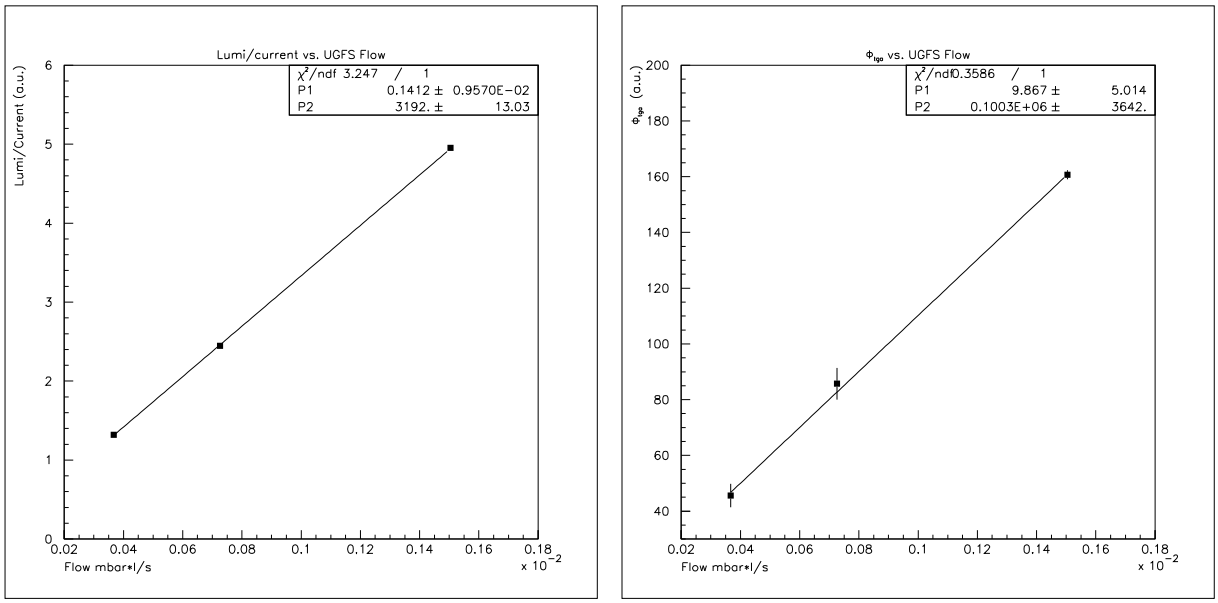


*Figure 6.6: On the **left**. Relationship between the Lumi value (a. u.) and the $H_2$ flow in mbar*l/s. On the **right**. Relationship between the TGA counts rate (normalized by the emission current) and the $H_2$ flow in mbar*l/s.*

### 6.3.4 Measurement of Target density $\langle n \rangle$

In order to derive an absolute value for the spin-exchange cross section, it is necessary to precisely determine the target density. As a direct measurement of the ABS atomic flux was not possible, an indirect measurement by means the calibrated UGFS flux has been performed. The equipment used in the measurement of the target density is constituted by the following devices (see chapter 1 for a complete description):

- the UGFS, which allows to inject into the storage cell a calibrated flux;
- the luminosity monitor (lumi), whose rates are proportional to the target density;
- the target gas analyzer, which counts the relative amount of hydrogen molecules and atoms inside to the cell and whose total rates are also proportional to the target density.

In the first part of the measurement lumi and TGA rates have been calibrated by injecting 3 known $H_2$ molecular fluxes by the UGFS. In the second stage the ABS flux have been derived by making use of the previously calibrated lumi and TGA rates.
With the ABS atomic flux also a small amount of molecules is injected, this had to taken also into account. As the molecules move with a velocity which is a factor $\sqrt{2}$ slower than

the atoms their contribution to the target density is a factor $\sqrt{2}$ higher. This means that the target density and therefore the lumi rates, for a constant total amount of H atoms in the cell, depend on the atomic fraction $\alpha$.
The lumi rates measured feeding the cell with the ABS (atoms + molecules), have been corrected for the atomic fraction $\alpha$ according to the formula:

$$lumi_{corrected} = \frac{lumi}{current}\sqrt{2}\,\alpha + (1-\alpha)\,\frac{lumi}{current} \tag{6.9}$$

The first and second term on the right side of equation 6.9 represent the atomic and molecular contributions respectively[2].
In figure 6.7 the rates measured by the luminosity monitor using the ABS (empty circle) corrected with equation 6.9 are reported in the same plot together with the ones measured filling the cell with the calibrated UGFS.
The ABS flux resulted

$$\Phi_{ABS} \quad = \quad (9.10 \pm 0.13) * 10^{-4} \quad mbar * l/s \tag{6.10}$$

in standard condition (temperature $273.15K$ and a pressure of $1013atm$) the volume occupated by a mole of gas is $22.41l$.

$$\frac{9.1 \cdot 10^{-4}\,(mbar \cdot l \cdot s^{-1}) \cdot 273}{1013(mbar) \cdot 22.41(l \cdot mol^{-1}) \cdot 100} = 1.09 \cdot 10^{-7}\frac{mol}{s} \tag{6.11}$$

where STP temperature has been normalized to the cell temperature ($100K$). Taking into account that in a mol there are $6.02 \cdot 10^{23}$ particles we obtain

$$\Phi_{ABS} \quad = \quad (6.57 \pm 0.09) * 10^{16} \quad atoms/s \tag{6.12}$$

By using the value for the cell conductance determined in section 6.3.3 the average density in the cell can be derived by using the formula:

$$\langle\, n \,\rangle = \frac{\Phi^{ABS}}{2\,C^{tot}} \tag{6.13}$$

[2]Note that the value of $\alpha$ during this measurement was 0.977±0.009

| Q (mbar*l/s) | Total counts rate/$I_{emiss}$ | Lumi/Current (a. u.) | ABS density |
|---|---|---|---|
| $0.367 * 10^{-3} \pm 0.001 * 10^{-3}$ | $46 \pm 4$ | $1.319 \pm 0.006$ | 0.5*ABS |
| $0.726 * 10^{-3} \pm 0.005 * 10^{-3}$ | $86 \pm 7$ | $2.446 \pm 0.008$ | 1*ABS |
| $1.503 * 10^{-3} \pm 0.001 * 10^{-3}$ | $161 \pm 2$ | $4.952 \pm 0.013$ | 2*ABS |

*Table 6.5: Values obtained injecting three different density of gas with the UGFS, Q is the flow out-coming to the UGFS, the total counts rate are the rate detected by the TGA, ABS density is the setting of the ABS during this measurement*

| Q (mbar*l/s) | Total counts rate/$I_{emiss}$ | Lumi/Current (a. u.) | ABS density |
|---|---|---|---|
| $9.10 * 10^{-4} \pm 0.13 * 10^{-4}$ | $101.3 \pm 0.9$ | $2.165 \pm 0.006$ | $\surd$ |
| $9.10 * 10^{-4} \pm 0.13 * 10^{-4}$ | $101.3 \pm 0.9$ | $3.04 \pm 0.04$ | corrected by $\alpha_r$ |

*Table 6.6: Flow out-coming the ABS estimated by comparison the value obtained with the UGFS*

$$\langle n \rangle = (3.61 \pm 0.18) * 10^{12} atoms/cm^3 \tag{6.14}$$

As the cell conductance has been evaluated at 100 K, to obtain the value of the density also for the other temperatures, one has to scale the given conductance according to:

$$C_T = C_{100}\sqrt{\frac{T}{100K}} \tag{6.15}$$

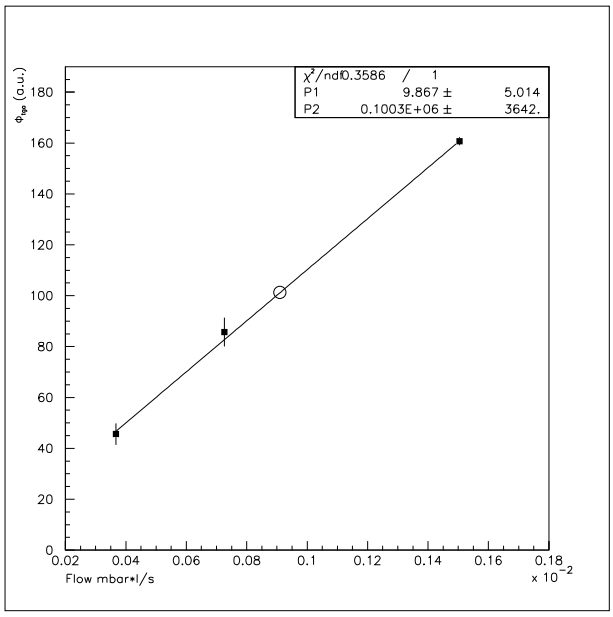


*Figure 6.7: The TGA count rates vs. the flow (in mbar*l/s) with the ABS value (open circle, where the size of the point is bigger than the error). All the errors are only statistic.*

| Temperature K | First set $\sigma_{se}$ $10^{-16}\,cm^2$ | Second set $\sigma_{se}$ $10^{-16}\,cm^2$ | Third set $\sigma_{se}$ $10^{-16}\,cm^2$ | **Final value** $\sigma_{se}$ $10^{-16}\,cm^2$ |
|---|---|---|---|---|
| 40 | $21.8 \pm 2.3$ | $19.0 \pm 0.9$ | $20.4 \pm 2.3$ | $19.6 \pm 3.4$ |
| 60 | $20.1 \pm 1.0$ | $19.9 \pm 1.4$ | *no* | $20.1 \pm 2.2$ |
| 80 | $24.5 \pm 1.4$ | $24.0 \pm 1.2$ | *no* | $24.2 \pm 2.2$ |
| 100 | $22.5 \pm 2.3$ | $26.9 \pm 1.9$ | *no* | $25.7 \pm 3.6$ |

*Table 6.7: Cross section values for each temperature with the statistic error at for every set of measurement*

The spin exchange collision measurement have been performed without beam and consequently the lumi could not be used to monitor the target density during the measurement. Instead of these the TGA rates have been used.

## 6.4 Final Results $\sigma_{se}$

With all the elements described up to now it is possible calculate the spin exchange cross section by the formula 6.4.
The results for the spin exchange cross section obtained at the different temperature for the measurements performed are reported in table 6.7, the only measurement performed three time was at 40 K.
The reported errors are the total ones: both statistic and systematic. The systematic error for each measurement was taken as the half difference between the value of cross section obtained injecting $P_z^+$ and $P_z^-$. In fact the ABS is flipping continuously the state of polarization injected. If the value of the cross section obtained, injecting $P_z^+$ or $P_z^-$ is different may this has been attributed to systematics of the experimental setup. For this reason the half difference was taken as a systematic error for each measurement. Other terms present in formula 6.4 that contribute to the total error are:

- the fit procedure 0.5 %
- density measurement 5.0%

To obtain the final value, the set of measurement has been averaged with a weighted average.
The plot of figure 6.8 shows the value for the spin - exchange cross section obtained in this work, versus the temperature. The results are shown together with the other experimental existing data (triangular point [75]) and the average of the two cross section calculated by Allison [68].

$$\sigma_{av} = \frac{1}{2}\sigma^{-} + \frac{1}{2}\sigma^{+} \tag{6.16}$$

The agreement, between the experimental data and the theoretical calculation, on an extended range of temperature, is in the error.
In the plot of figure 6.9, the experimental data obtained in this work are compared with three theoretical calculation. The calculation that better describes the experimental data is the Allison one.

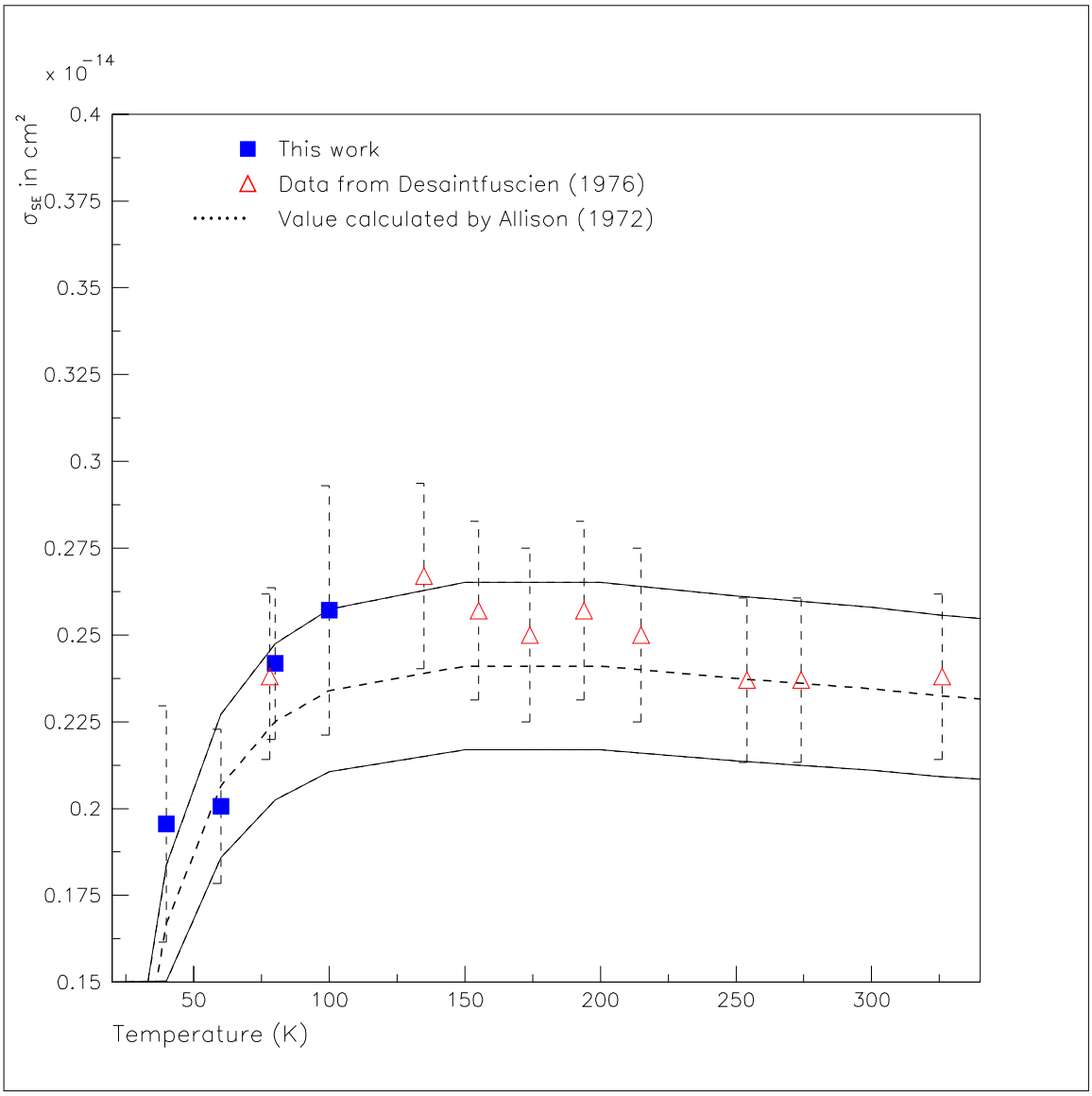


*Figure 6.8: The experimental data for the spin exchange collision cross section are compared with the theoretical calculation made by Allison. The value of the cross section obtained with the HERMES target are shown with squared point, the triangular ones was measured by [75] in 1976.*

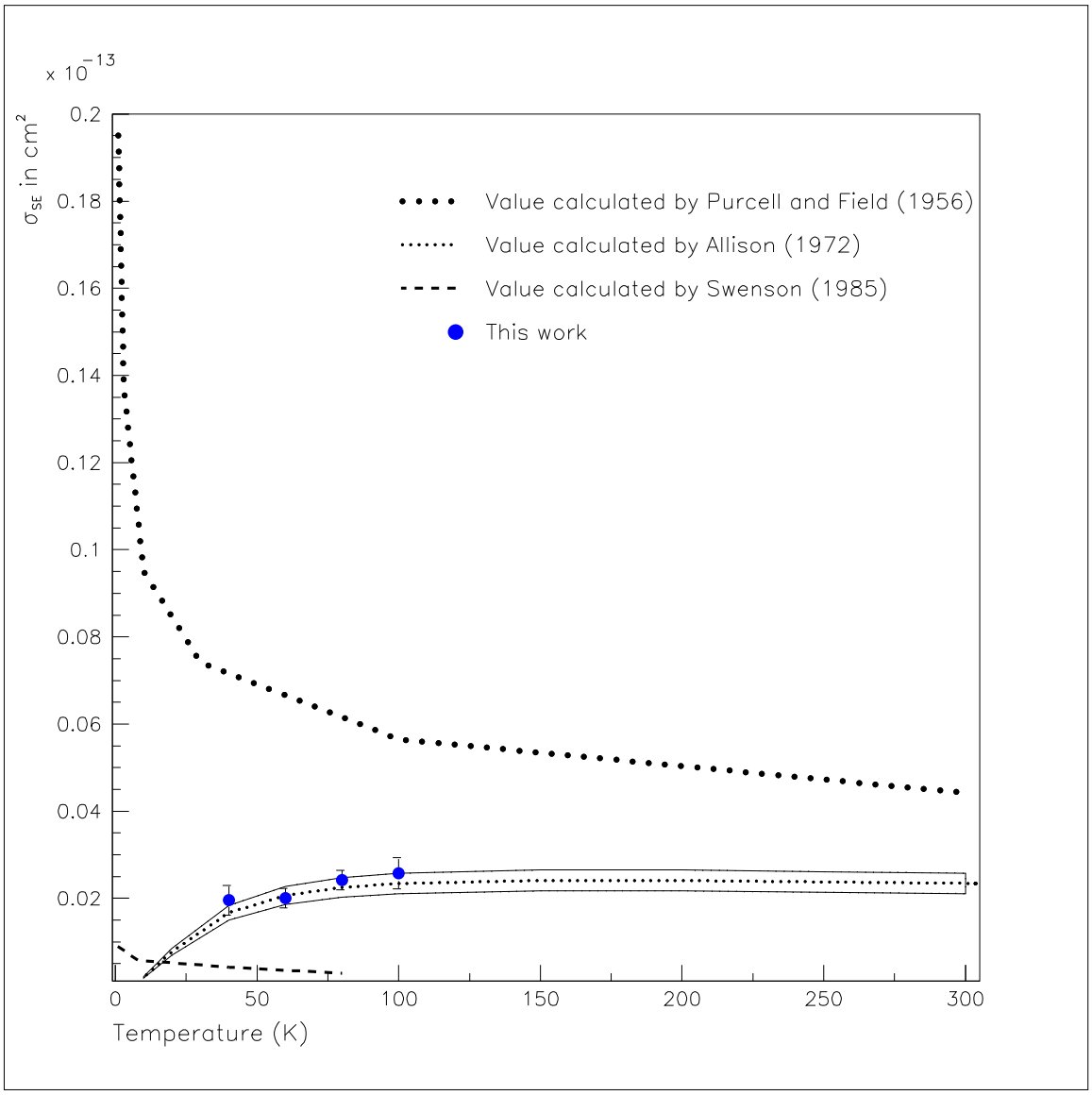


*Figure 6.9: General overview on the experimental data and the theoretical calculations.*

# Conclusions

In the first part of this work the performance of the HERMES polarized H/D target for the whole period of data taking (1997 - 2005) has been shown. Even if the different targets showed different characteristics all of them provided almost all the time high polarization ($> 75\%$) and low systematic errors ($3 - 4\%$) for all the running period. In ten years of running a total amount of about 20 millions double polarized Deep Inelastic Scattering events have been collected by the HERMES spectrometer. Among these, the $H_\perp$ events collected in 2002 - 2005 are the first sample of this kind ever taken.

In the second part of this thesis the measurement of the spin - exchange collision cross section has been presented. Three different theoretical calculations have been compared with the experimental data. All the authors foreseen a strongly dependent cross - section for temperature below 80 K.
The only experimental data existing in literature, previously to this work, pointed out that for the temperature range (100 - 300 K) the best model reflecting the data is the Allison one. The experimental results obtained with the HERMES target are the first in the low temperature region (40 - 100 K) and they are in good agreement with the other experimental data and with the same Allison's calculation.

# Appendix A

# Hyperfine Structure

The knowledge of hydrogen and deuterium hyperfine structure is essential for the understanding of the HERMES polarized target. First of all, the target polarization is achieved and measured by selecting particular hyperfine states through the Stern-Gerlach separation and by exchanging their populations via hyperfine transitions. Furthermore, potential processes of spin relaxation can be explained in terms of the same transition's mechanism. This is particularly true for the case of the resonant depolarization induced by the HERA electron bunched beam.
After a survey over the basics of the static hyperfine structure of hydrogen and deuterium, the central part of the chapter is devoted to the theory of hyperfine transitions.

## A.1 The solution of the static Hamiltonian

The hyperfine structure of the hydrogen/deuterium atom in the ground state $1S_{1/2}$ can be derived from a Hamilton operator describing the coupling between the spin of the electron $\mathbf{S}$ and spin on the nucleus $\mathbf{I}$ and the additional interactions of the magnetic moments with an external magnetic field $\mathbf{B}$:

$$\mathcal{H} = A_{H,D}\mathbf{S}\cdot\mathbf{I} + \frac{g_S\mu_B}{\hbar}\mathbf{S}\cdot\mathbf{B} - \frac{g_I\mu_N}{\hbar}\mathbf{I}\cdot\mathbf{B} \tag{A.1}$$

The constant $A_{H,D}$ contains information about the coupling strength between $\mathbf{S}$ and $\mathbf{I}$ for hydrogen and deuterium respectively. The quantity $\mu_B = \frac{e\hbar}{2m_e c}$ ($\mu_N = \frac{e\hbar}{2m_p c}$) is the Bohr (nuclear) magnet on relating the spin $\mathbf{S}$ ($\mathbf{I}$) to the magnetic moment $\boldsymbol{\mu}_\mathbf{e}$ ($\boldsymbol{\mu}_\mathbf{I}^{p,d}$ for proton and deuteron respectively) through $\frac{\boldsymbol{\mu}_\mathbf{e}}{\mu_B} = g_S\mathbf{S}$ ($\frac{\boldsymbol{\mu}_\mathbf{I}^{p,d}}{\mu_N} = g_I\mathbf{I}$), where $g_S = -2.0023$ ($g_I^p = 5.5857$, $g_I^d = 0.8574$) is the electron (proton, deuteron) gyro-magnetic factor.
In case of hydrogen the coupling $\mathbf{F} = \mathbf{S}\cdot\mathbf{I}$, where $S = I = \frac{1}{2}$, originates a singlet state with total spin $F = 0$ and a triplet with $F = 1$ ($m_F = \pm 1, 0$). In case of deuterium $I = 1$, so that a doublet $F = \frac{1}{2}$ ($m_F = \pm\frac{1}{2}$) and a quadruplet $F = \frac{3}{2}$ ($m_F = \pm\frac{3}{2}, \pm\frac{1}{2}$)

are produced by the spin-spin coupling. The energy difference between the two levels is known as *hyperfine splitting* $E_{HFS}^{H,D}$ for hydrogen and deuterium respectively.
The presence of an external magnetic field $\mathbf{B}$ introduces the additional couplings $\mathbf{S}\cdot\mathbf{B}$ and $\mathbf{I}\cdot\mathbf{B}$. This leads to the splitting of the non-singlet states and the consequent generation of four defined energy levels for hydrogen and six for deuterium.

### A.1.1 Hydrogen

The Hamiltonian (A.1) can be written as follows:

$$\mathcal{H} = A_H\hbar^2\left[\frac{\mathbf{S}\cdot\mathbf{I}}{\hbar^2} + \frac{\mathbf{B}}{B_C^H}\cdot\left(\frac{\mathbf{S}}{\hbar} - \varepsilon_H\frac{\mathbf{I}}{\hbar}\right)\right] \tag{A.2}$$

where $B_C^H = \frac{A_H\hbar^2}{g_S\mu_B} = 50.7\,\mathrm{mT}$ is the so-called *critical field*, whereas $\varepsilon_H = \frac{g_I\mu_N}{g_S\mu_B} = 1.5\cdot 10^{-3} \ll 1$.
In the representation $|\,\mathbf{S}^2,\mathbf{I}^2;m_S,m_I\,\rangle$ (where $m_S$ and $m_I$ refer to the operators $S_z$ e $I_z$), a basis for the Hamilton operator is given by:

$$|\uparrow+\rangle \quad , \quad |\uparrow-\rangle \quad , \quad |\downarrow-\rangle \quad , \quad |\downarrow+\rangle \tag{A.3}$$

where the arrow refers to the electron and the sign to the nuclear spin. The spin-spin coupling term in A.2 can be written as

$$\mathbf{S}\cdot\mathbf{I} = I_zS_z + \frac{1}{2}(I_+S_- + I_-S_+) \tag{A.4}$$

where $I_\pm = I_x \pm iI_y$ and $S_\pm = S_x \pm iS_y$. Taking into account that $S_z = I_z = \pm\frac{\hbar}{2}$, one can write A.4 in the following matrix representation:

$$\mathbf{S}\cdot\mathbf{I} = \frac{\hbar^2}{4}\begin{pmatrix} 1 & 0 & 0 & 1 \\ 0 & -1 & 0 & 2 \\ 0 & 0 & 1 & 0 \\ 0 & 2 & 0 & -1 \end{pmatrix} \tag{A.5}$$

For the terms of A.2 representing the interactions with the external magnetic field, one has:

$$\mathbf{S}\cdot\mathbf{B} = S_zB_z + \frac{1}{2}S_+(B_x - iB_y) + \frac{1}{2}S_-(B_x + iB_y) \tag{A.6}$$

and correspondingly

$$\mathbf{I}\cdot\mathbf{B} = I_zB_z + \frac{1}{2}I_+(B_x - iB_y) + \frac{1}{2}I_-(B_x + iB_y) \tag{A.7}$$

In case of a static magnetic field along the $z$ direction, $\mathbf{B} = (0, 0, B)$ and defining the variable $x = \frac{B}{B_C^H}$, the matrix representations of (A.6) and (A.7) are:

$$\frac{\mathbf{B}}{B_C^H} \cdot \mathbf{S} = \frac{\hbar}{2} \begin{pmatrix} x & 0 & 0 & 0 \\ 0 & x & 0 & 0 \\ 0 & 0 & -x & 0 \\ 0 & 0 & 0 & -x \end{pmatrix} \tag{A.8}$$

and

$$\frac{\mathbf{B}}{B_C^H} \cdot \mathbf{I} = \frac{\hbar}{2} \begin{pmatrix} x & 0 & 0 & 0 \\ 0 & -x & 0 & 0 \\ 0 & 0 & -x & 0 \\ 0 & 0 & 0 & x \end{pmatrix} \tag{A.9}$$

The static Hamiltonian $\mathcal{H}_0^{st}$ can now be completely represented by the following matrix form:

$$\mathcal{H}_0^{st} = \frac{A_H \hbar^2}{4} \begin{pmatrix} 1 + 2x(1 - \varepsilon_H) & 0 & 0 & 0 \\ 0 & -1 + 2x(1 + \varepsilon_H) & 0 & 2 \\ 0 & 0 & 1 - 2x(1 - \varepsilon_H) & 0 \\ 0 & 2 & 0 & -1 - 2x(1 + \varepsilon_H) \end{pmatrix} \tag{A.10}$$

Since the matrix (A.10) is not diagonal, the basis (A.3) does not represent a set of eigenstates of (A.2). The diagonalization of (A.10) can be performed by means of an orthogonal transformation:

$$\mathcal{H}_1^{st} = U_0^T \mathcal{H}_0^{st} U_0 \tag{A.11}$$

where the orthonormal matrix $U_0$ is given by

$$U_0 = \begin{pmatrix} 1 & 0 & 0 & 0 \\ 0 & \cos\theta & 0 & -\sin\theta \\ 0 & 0 & 1 & 0 \\ 0 & \sin\theta & 0 & \cos\theta \end{pmatrix} \tag{A.12}$$

The so-called *mixing angle* $\theta$ depends on $x = \frac{B}{B_C}$ and can be derived from the following relations:

$$\begin{aligned} \cos\theta &= \sqrt{\tfrac{1}{2}(1 + \cos 2\theta)} & \qquad \sin\theta &= \sqrt{\tfrac{1}{2}(1 - \cos 2\theta)} \\ \cos 2\theta &= \tfrac{x(1+\varepsilon_H)}{\sqrt{x^2(1+\varepsilon_H)^2+1}} & \qquad \sin 2\theta &= \tfrac{1}{\sqrt{x^2(1+\varepsilon_H)^2+1}} \end{aligned} \tag{A.13}$$

The eigenenergies of $\mathcal{H}_1^{st}$ are:

$$\begin{aligned} E_1 &= \tfrac{E_{HFS}^H}{4}\big(1 + 2x(1 - \varepsilon_H)\big) & \qquad E_3 &= \tfrac{E_{HFS}^H}{4}\big(1 - 2x(1 - \varepsilon_H)\big) \\ E_2 &= \tfrac{E_{HFS}^H}{4}\big(-1 + 2\sqrt{x^2(1 + \varepsilon_H)^2 + 1}\,\big) & \qquad E_4 &= \tfrac{E_{HFS}^H}{4}\big(-1 - 2\sqrt{x^2(1 + \varepsilon_H)^2 + 1}\,\big) \end{aligned} \tag{A.14}$$

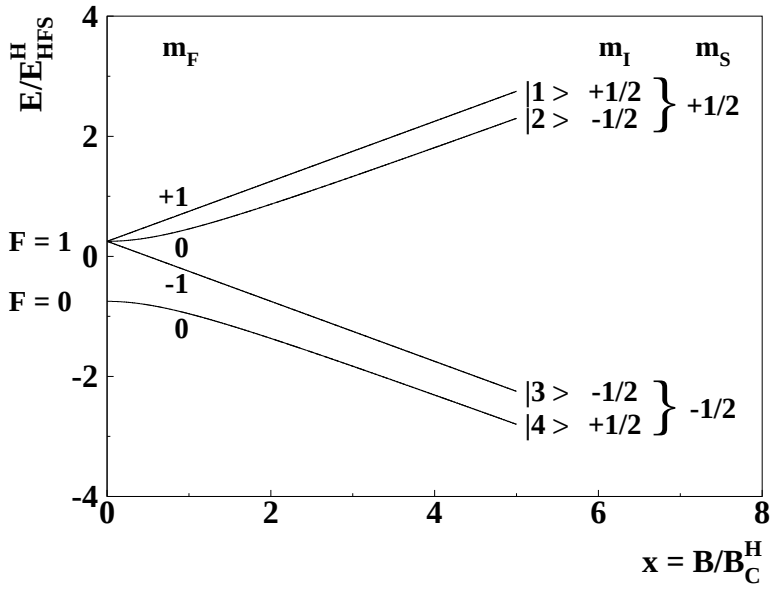


*Figure A.1: Hyperfine energy levels of hydrogen plotted as functions of the magnetic holding field (Breit-Rabi diagram). The energies are scaled to the hyperfine energy $E^H_{HFS}$ and the field values to the critical field $B^H_C$.*

where $E^H_{HFS} = A_H \hbar^2 = 5.87 \cdot 10^{-6}\,\mathrm{eV}$ represents the energy difference between the state with total spin $F = 1$ and the one with $F = 0$, if no external magnetic field is present ($x = 0$). The hydrogen hyperfine splitting is usually known in terms of the frequency $\nu^H_{HFS} = \frac{E^H_{HFS}}{2\pi\hbar} = 1420.4\,\mathrm{MHz}$. In figure A.1 the hydrogen hyperfine eigenenergies are plotted as functions of the variable $x$.
The new basis is composed by eigenstates of the operators $\mathbf{F}^2$ and $F_z = S_z + I_z$:

$$\begin{aligned} |1\rangle &= |\uparrow +\rangle & |3\rangle &= |\downarrow -\rangle \\ |2\rangle &= \cos\theta\,|\uparrow -\rangle + \sin\theta\,|\downarrow +\rangle & |4\rangle &= \sin\theta\,|\uparrow -\rangle - \cos\theta\,|\downarrow +\rangle \end{aligned} \tag{A.15}$$

**Polarization definitions**

The electron and nuclear polarizations ($P_e$ and $P_z$) of the state $|\,i\,\rangle$ are given by the expectation values of the operators $\frac{2}{\hbar}S_z$ and $\frac{2}{\hbar}I_z$ respectively. For a sample of atoms one has:

$$P_e = \sum_{i=1}^{4} n_i \langle\, i\,|\, \frac{2}{\hbar} S_z \,|\, i\,\rangle = n_1 - n_3 + (n_2 - n_4)\cos 2\theta \tag{A.16}$$

$$P_z = \sum_{i=1}^{4} n_i \langle\, i\,|\, \frac{2}{\hbar} I_z \,|\, i\,\rangle = n_1 - n_3 - (n_2 - n_4)\cos 2\theta \tag{A.17}$$

where $n_i$ is the relative population of state $|\,i\,\rangle$, undergoing the following normalization condition:

$$\sum_i n_i = 1 \tag{A.18}$$

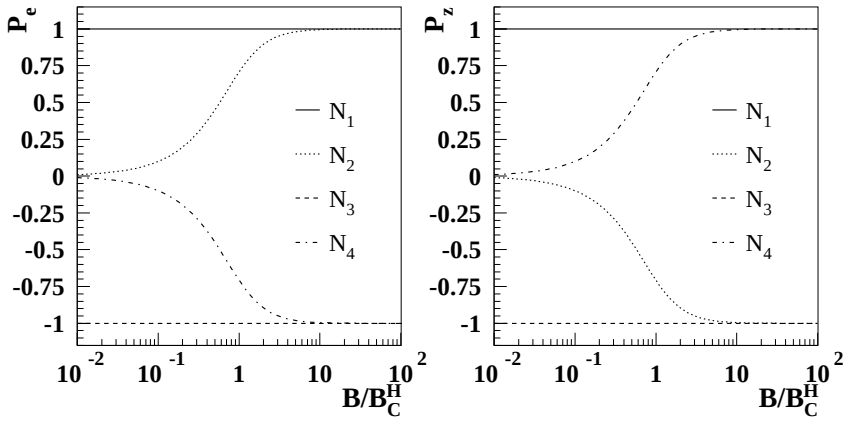


*Figure A.2: The electron (left) and nuclear polarizations of the four hydrogen hyperfine states plotted as functions of the external magnetic field. The field values are normalized to the critical field $B_C^H$.*

$P_e$ and $P_z$ for the different hydrogen hyperfine states are plotted in figure A.2 as function of the applied magnetic field.
The critical field $B_C^H$ marks the boundary between two field regions:

- $B \ll B_C^H \Longleftrightarrow \theta \to \frac{\pi}{4}$, Zeeman limit.
  The interaction with the external field can be treated perturbatively. A basis is given by the eigenstates of $|\,F, m_F\,\rangle$. The pure states $|\,1\,\rangle$ and $|\,3\,\rangle$ are polarized ($P_e = P_z = \pm 1$), whereas $|\,2\,\rangle$ and $|\,4\,\rangle$ are unpolarized ($P_e = P_z \simeq 0$):

$$\begin{aligned} |\,1\,\rangle &\simeq |\,F=1, m_F=+1\,\rangle &&= |\uparrow +\rangle \\ |\,2\,\rangle &\simeq |\,F=1, m_F=0\,\rangle &&= \frac{1}{\sqrt{2}}\left(|\uparrow -\rangle + |\downarrow +\rangle\right) \\ |\,3\,\rangle &\simeq |\,F=1, m_F=-1\,\rangle &&= |\downarrow -\rangle \\ |\,4\,\rangle &\simeq |\,F=0, m_F=0\,\rangle &&= \frac{1}{\sqrt{2}}\left(|\uparrow -\rangle - |\downarrow +\rangle\right) \end{aligned} \tag{A.19}$$

- $B_z >> B_C^H \Longleftrightarrow \theta \to 0$, Paschen-Back limit.
  The spin-spin interaction can be treated perturbatively. Now the eigenstates can be represented by the basis (A.3) where all the states are polarized.

### A.1.2 Deuterium

In case of deuterium the Hamiltonian (A.1) can be written as follows:

$$\mathcal{H} = A_D \hbar^2 \left[ \frac{\mathbf{S}\cdot\mathbf{I}}{\hbar^2} + \frac{3}{2}\frac{\mathbf{B}}{B_C^D}\left(\frac{\mathbf{S}}{\hbar} - \varepsilon_D \frac{\mathbf{I}}{\hbar}\right)\right] \tag{A.20}$$

where $B_C^D = \frac{3}{2}\frac{A_D\hbar^2}{g_S\mu_B} = 11.7\,\mathrm{mT}$ is the critical field, while $\varepsilon_D = \frac{g_I\mu_K}{g_S\mu_B} = 2.3\cdot 10^{-4} \ll 1$.
In the representation $|\,\mathbf{S}^2, \mathbf{I}^2; m_S, m_I\,\rangle$ (where $m_S$ and $m_I$ refer again to $S_z$ e $I_z$), a basis can be written as

$$|\uparrow 1\rangle \quad , \quad |\uparrow 0\rangle \quad , \quad |\uparrow -1\rangle \quad , \quad |\downarrow 1\rangle \quad , \quad |\downarrow 0\rangle \quad , \quad |\downarrow -1\rangle \tag{A.21}$$

where the arrow refers to the electron spin.
Following the same scheme applied for hydrogen, the spin-spin interaction term results:

$$\mathbf{S}\cdot\mathbf{I} = \frac{\hbar^2}{2}\begin{pmatrix} 1 & 0 & 0 & 0 & 0 & 0 \\ 0 & 0 & 0 & 0 & 0 & \sqrt{2} \\ 0 & 0 & -1 & 0 & \sqrt{2} & 0 \\ 0 & 0 & 0 & 1 & 0 & 0 \\ 0 & 0 & \sqrt{2} & 0 & 0 & 0 \\ 0 & \sqrt{2} & 0 & 0 & 0 & -1 \end{pmatrix} \tag{A.22}$$

while the external magnetic field interaction terms can be expressed by

$$\frac{3}{2}\frac{\mathbf{B}}{B_C^D}\cdot\mathbf{S} = \frac{3}{2}\frac{\hbar}{2}\begin{pmatrix} x & 0 & 0 & 0 & 0 & 0 \\ 0 & x & 0 & 0 & 0 & 0 \\ 0 & 0 & x & 0 & 0 & 0 \\ 0 & 0 & 0 & -x & 0 & 0 \\ 0 & 0 & 0 & 0 & -x & 0 \\ 0 & 0 & 0 & 0 & 0 & -x \end{pmatrix} \tag{A.23}$$

and

$$\frac{3}{2}\frac{\mathbf{B}}{B_C^D}\cdot\mathbf{I} = \frac{3}{2}\hbar\begin{pmatrix} x & 0 & 0 & 0 & 0 & 0 \\ 0 & 0 & 0 & 0 & 0 & 0 \\ 0 & 0 & -x & 0 & 0 & 0 \\ 0 & 0 & 0 & -x & 0 & 0 \\ 0 & 0 & 0 & 0 & 0 & 0 \\ 0 & 0 & 0 & 0 & 0 & x \end{pmatrix} \tag{A.24}$$

Finally, the matrix form of the Hamiltonian (A.20) is given by

$$\mathcal{H}_0^{st} = \frac{A_D\hbar^2}{2}\begin{pmatrix} 1+\frac{3}{2}x(1-2\varepsilon_D) & 0 & 0 & 0 & 0 & 0 \\ 0 & \frac{3}{2}x & 0 & 0 & 0 & \sqrt{2} \\ 0 & 0 & -1+\frac{3}{2}x(1+2\varepsilon_D) & 0 & \sqrt{2} & 0 \\ 0 & 0 & 0 & 1-\frac{3}{2}x(1-2\varepsilon_D) & 0 & 0 \\ 0 & 0 & \sqrt{2} & 0 & -\frac{3}{2}x & 0 \\ 0 & \sqrt{2} & 0 & 0 & 0 & -1-\frac{3}{2}x(1+2\varepsilon_D) \end{pmatrix} \tag{A.25}$$

The matrix (A.25) can be diagonalized by applying the orthogonal transformation (A.11), with $U_0$ now given by

$$U_0 = \begin{pmatrix} 1 & 0 & 0 & 0 & 0 & 0 \\ 0 & \cos\theta_+ & 0 & 0 & 0 & 0 \\ 0 & 0 & \cos\theta_- & 0 & -\sin\theta_+ & 0 \\ 0 & 0 & 0 & 1 & 0 & 0 \\ 0 & 0 & \sin\theta_- & 0 & \cos\theta_- & 0 \\ 0 & \sin\theta_+ & 0 & 0 & 0 & \cos\theta_+ \end{pmatrix} \tag{A.26}$$

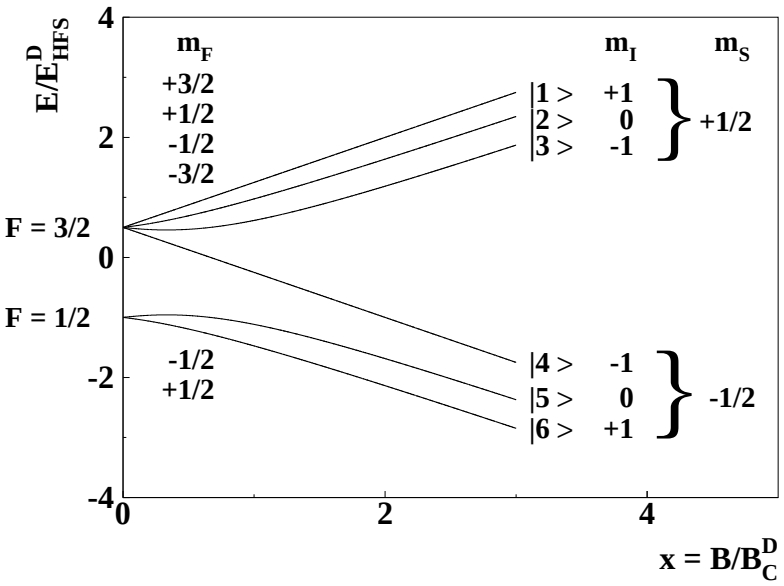


*Figure A.3:*
*Breit-Rabi diagram of deuterium. The energy and the magnetic field values are expressed as adimensional variables like in figure A.1.*

where

$$\begin{aligned} \cos\theta_\pm &= \sqrt{\tfrac{1}{2}(1+\cos 2\theta_\pm)} & \sin\theta_\pm &= \sqrt{\tfrac{1}{2}(1-\cos 2\theta_\pm)} \\ \cos 2\theta_\pm &= \tfrac{3x(1+2\varepsilon_D)\pm 1}{\sqrt{(3x(1+2\varepsilon_D)\pm 1)^2+8}} & \sin 2\theta_\pm &= \tfrac{\sqrt{8}}{\sqrt{(3x(1+2\varepsilon_D)\pm 1)^2+8}} \end{aligned} \tag{A.27}$$

are the relations from which one can derive the mixing angles $\theta_-$ e $\theta_+$.
The eigenenergies of the static Hamiltonian are:

$$\begin{aligned} E_1 &= \tfrac{E^D_{HFS}}{3}\big(1+\tfrac{3}{2}x(1-2\varepsilon_D)\big) \\ E_2 &= \tfrac{E^D_{HFS}}{6}\big(-1+\sqrt{9x^2(1+2\varepsilon_D)^2+6x(1+2\varepsilon_D)+9}\,\big) \\ E_3 &= \tfrac{E^D_{HFS}}{6}\big(-1+\sqrt{9x^2(1+2\varepsilon_D)^2-6x(1+2\varepsilon_D)+9}\,\big) \\ E_4 &= \tfrac{E^D_{HFS}}{3}\big(1-\tfrac{3}{2}x(1-2\varepsilon_D)\big) \\ E_5 &= \tfrac{E^D_{HFS}}{6}\big(-1-\sqrt{9x^2(1+2\varepsilon_D)^2-6x(1+2\varepsilon_D)+9}\,\big) \\ E_6 &= \tfrac{E^D_{HFS}}{6}\big(-1-\sqrt{9x^2(1+2\varepsilon_D)^2+6x(1+2\varepsilon_D)+9}\,\big) \end{aligned} \tag{A.28}$$

with $E^D_{HFS} = \frac{3}{2}A_D\hbar^2 = 1.35\cdot 10^{-6}\,\mathrm{eV}$, whereas the correspondent frequency is given by $\nu^D_{HFS} = 327.4\,\mathrm{MHz}$.
The deuterium energy levels are plotted in figure A.3 as functions of the external magnetic field. The interpretation of the critical field given for the hydrogen case is still valid.

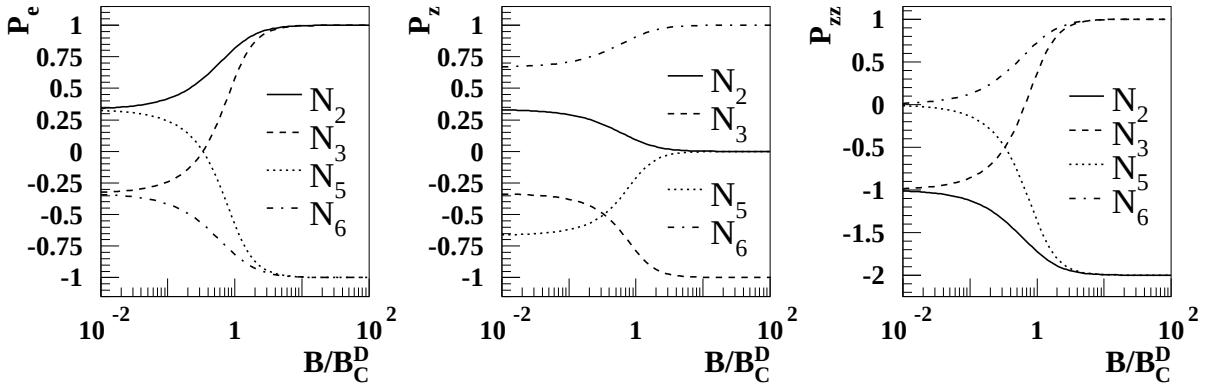


*Figure A.4: The electron (left), nuclear (center) and tensor polarizations of the four non-pure deuterium hyperfine states as functions of the external magnetic field. The polarizations of the pure states $|\,1\,\rangle$ and $|\,4\,\rangle$ do not depend on the strength of $B$.*

The basis of eigenstates correspondent to the eigenvalues (A.28) is:

$$\begin{aligned} |\,1\,\rangle &= |\uparrow +1\,\rangle & |\,4\,\rangle &= |\downarrow -1\,\rangle \\ |\,2\,\rangle &= \cos\theta_+\,|\uparrow 0\,\rangle + \sin\theta_+\,|\downarrow +1\,\rangle & |\,5\,\rangle &= \sin\theta_-\,|\uparrow -1\,\rangle - \cos\theta_-\,|\downarrow 0\,\rangle \\ |\,3\,\rangle &= \cos\theta_-\,|\uparrow -1\,\rangle + \sin\theta_-\,|\downarrow 0\,\rangle & |\,6\,\rangle &= \sin\theta_+\,|\uparrow 0\,\rangle - \cos\theta_+\,|\downarrow +1\,\rangle \end{aligned} \tag{A.29}$$

Only the first and the fourth are pure states (i.e. polarized). The polarization of the remaining states depends on the values of the mixing angles $\theta_+$ e $\theta_-$.

### Polarization definitions

The polarization of electrons $P_e$ and nuclei $P_z$ are given by

$$P_e = \sum_{i=1}^{6} n_i \,\langle\, i \,|\, \frac{2}{\hbar} S_z \,|\, i \,\rangle = n_1 - n_4 + (n_2 - n_6)\cos 2\theta_+ + (n_3 - n_5)\cos 2\theta_- \tag{A.30}$$

$$P_z = \sum_{i=1}^{6} n_i \,\langle\, i \,|\, \frac{1}{\hbar} I_z \,|\, i \,\rangle = n_1 + n_6 - n_3 - n_4 + (n_2 - n_6)\sin^2\theta_+ + (n_3 - n_5)\sin^2\theta_-$$

As the deuteron has spin $I = 1$, $m_I = 0, \pm 1$, the *vector polarization* $P_z$ alone does not entirely describe its spin state. In order to complete the nuclear spin representation of deuterium one usually employs the *tensor polarization* $P_{zz}$, defined as the z-z component of the tensor operator $I_{ij} = \frac{3}{2}(I_i I_j + I_j I_i) - 2\delta_{ij}$ [1]. The tensor polarization of the deuteron is then given by:

$$P_{zz} = \langle\, I_{zz} \,\rangle = \left\langle\, 3I_z^2 - 2 \,\right\rangle \tag{A.31}$$

and hence:

$$P_{zz} = n_1 + n_4 - \frac{1}{2}(n_2 + n_3 + n_5 + n_6) - \frac{3}{2}(n_2 - n_6)\cos 2\theta_+ + \frac{3}{2}(n_3 - n_5)\cos 2\theta_- \tag{A.32}$$

The polarizations for the different deuterium hyperfine states are plotted in figure A.4 as functions of the applied magnetic field.

## A.2 Hyperfine transitions

Let us consider once more the Hamilton operator (A.1) applying the Schrödinger equation to one of its eigenstates $\Psi$:

$$i\hbar\frac{\partial}{\partial t}\Psi = \mathcal{H}\Psi \tag{A.33}$$

If one multiplies from the left the orthonormal operator $U_0$ (see eq. A.12 or A.26), one has:

$$i\hbar\left(\frac{\partial}{\partial t}U_0^T\Psi + U_0^T\frac{\partial}{\partial t}\Psi\right) = \left(U_0^T\mathcal{H} + i\hbar\frac{\partial}{\partial t}U_0^T\right)\Psi \tag{A.34}$$

Applying $U_0^T U_0 = \mathbf{1}$ in the second member of (A.34), one obtains:

$$i\hbar\left(\frac{\partial}{\partial t}U_0^T\Psi + U_0^T\frac{\partial}{\partial t}\Psi\right) = \left(U_0^T\mathcal{H}U_0 + i\hbar\frac{\partial}{\partial t}U_0^T U_0\right)U_0^T\Psi \tag{A.35}$$

Finally, changing basis by means of the transformation $\Phi = U^T\Psi$, one has:

$$i\hbar\frac{\partial}{\partial t}\Phi = \left(\mathcal{H}_1^{st} + i\hbar\frac{\partial}{\partial t}U_0^T U_0\right)\Phi \tag{A.36}$$

where $\mathcal{H}_1^{st}$ represents the diagonal static Hamiltonian, already encountered in the previous section.
The term $i\hbar\frac{\partial}{\partial t}U_0^T U_0$ is non-zero if the external magnetic field is time dependent. In such a case, the resulting distortion of the eigenstates may originate transitions between pairs of hyperfine states.
Each transition is characterized by a defined frequency $\nu_{ab}$ related to the energy difference between the two hyperfine states:

$$\nu_{ab} = \frac{|E_a - E_b|}{2\pi\hbar} \tag{A.37}$$

The holding field dependence of the energy levels (see eq. (A.14) and (A.28)) is of course transferred to the transition frequencies.
Hyperfine transitions can be classified depending on the relative orientations of the static holding field $\mathbf{B}^{st}$ and the time dependent one $\mathbf{B}(t)$. Transitions caused by the component of $\mathbf{B}(t)$ parallel to the static one are called $\sigma$, whereas transitions generated by the perpendicular component of $\mathbf{B}(t)$ are called $\pi$.
A further possible classification of hyperfine transitions will be discussed in section A.2.4.

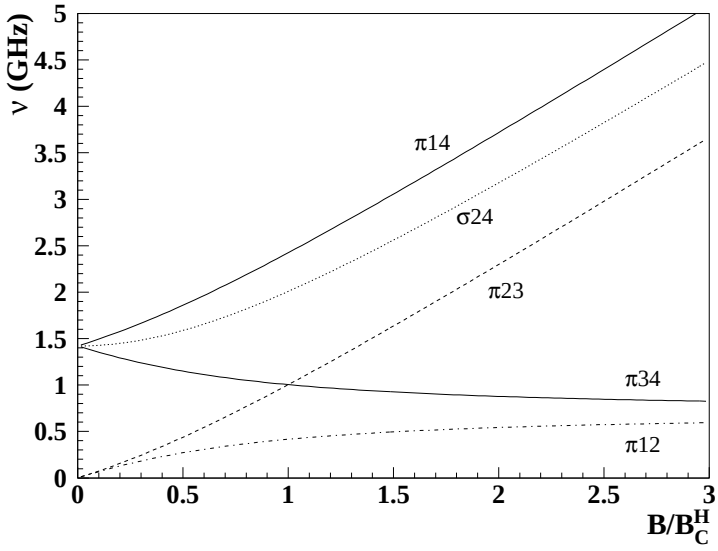


*Figure A.5:*
*Frequencies of hydrogen hyperfine transitions plotted as functions of the holding field. The field values are normalized to the critical field $B_C^H$.*

### A.2.1 Hydrogen

Let us consider an external magnetic field having the following form:

$$\mathbf{B} = (0, 0, B^{st} + b(t)) \tag{A.38}$$

so that the static component of the field $B^{st}$ and the time dependent one $b(t)$ are parallel. Choosing $b(t) = b_{\|} \cos \nu t$, the time dependent part of the hydrogen Hamiltonian contained in (A.36) becomes

$$\mathcal{H}_1^{\sigma} = i\hbar \begin{pmatrix} 0 & 0 & 0 & 0 \\ 0 & s\dot{s} + c\dot{c} & 0 & -s\dot{c} + c\dot{s} \\ 0 & 0 & 0 & 0 \\ 0 & s\dot{c} - c\dot{s} & 0 & s\dot{s} + c\dot{c} \end{pmatrix} = \frac{i\hbar\nu}{2} y_{\sigma} \sin \nu t \begin{pmatrix} 0 & 0 & 0 & 0 \\ 0 & 0 & 0 & \sin^2\theta \\ 0 & 0 & 0 & 0 \\ 0 & -\sin^2\theta & 0 & 0 \end{pmatrix} \tag{A.39}$$

where $c = \cos\theta$, $s = \sin\theta$, $y_{\sigma} = \frac{b_{\|}}{B_C^H}$ and the constant $\varepsilon_H \ll 1$ has been neglected.
Hence, the superposition of a time dependent magnetic field parallel to the holding field results in the connection of hyperfine states $|\,2\,\rangle$ and $|\,4\,\rangle$ of hydrogen. This leads to the possible transition

$$\sigma\,|\,2\,\rangle \leftrightarrow |\,4\,\rangle \qquad\qquad (\Delta F = \pm 1, \Delta m_F = 0)$$

Let us choose now the time-dependent component of the field to be perpendicular to the holding field so that $b(t)$ is either directed along $x$ or along $y$. In order to describe this scenario, one has to rewrite the matrix form of the Hamilton operator (A.2) in the following way:

$$\mathcal{H}_0 = \mathcal{H}_0^{st} + \mathcal{H}_0^{\pi} \tag{A.40}$$

where $\mathcal{H}_0^{st}$ designates the static part of the Hamiltonian and the index 0 denotes the representation given by the basis (A.3).
By applying the orthogonal transformation (A.12) to $\mathcal{H}_0^{\pi}$, one finds:

$$\mathcal{H}_1^{\pi} = U_0^T \mathcal{H}_0^{\pi} U_0 \tag{A.41}$$

If one aligns the time dependent field along $x^1$, so that

$$\mathbf{B} = (b(t), 0, B_z^{st}) \tag{A.42}$$

defining $b(t) = b_{\perp}\cos(\nu t)$ and neglecting the constant $\varepsilon_H \ll 1$, one finds

$$\mathcal{H}_1^{\pi} \simeq i\frac{E_{HFS}^H}{2} y_{\pi} \cos\nu t \begin{pmatrix} 0 & \sin\theta & 0 & -\cos\theta \\ \sin\theta & 0 & -\cos\theta & 0 \\ 0 & \cos\theta & 0 & -\sin\theta \\ \cos\theta & 0 & -\sin\theta & 0 \end{pmatrix} \tag{A.43}$$

where $y_{\pi} = \frac{b_{\perp}}{B_C^H}$ .
Thus, from the (A.43) one can conclude that the presence of a time dependent field perpendicular to the static one connects the four pairs of hyperfine states, leading to the following possible transitions:

$$\begin{aligned} \pi\,|\,1\,\rangle &\leftrightarrow |\,2\,\rangle \qquad (\Delta F = 0, \Delta m_F = \pm 1) \\ \pi\,|\,2\,\rangle &\leftrightarrow |\,3\,\rangle \qquad (\Delta F = 0, \Delta m_F = \pm 1) \\ \pi\,|\,1\,\rangle &\leftrightarrow |\,4\,\rangle \qquad (\Delta F = \pm 1, \Delta m_F = \pm 1) \\ \pi\,|\,3\,\rangle &\leftrightarrow |\,4\,\rangle \qquad (\Delta F = \pm 1, \Delta m_F = \pm 1) \end{aligned}$$

In figure A.5 the resonance frequencies of all hydrogen transitions are plotted as function of the holding field.

### A.2.2 Deuterium

By choosing the time dependent field $b(t) = b_{\parallel}\cos\nu t$ to be parallel to the static one and neglecting the constant $\varepsilon_D \ll 1$, one gets:

$$\mathcal{H}_1^{\sigma} = i\hbar \begin{pmatrix} 0 & 0 & 0 & 0 & 0 & 0 \\ 0 & s_+\dot{s}_+ + c_+\dot{c}_+ & 0 & 0 & 0 & -s_+\dot{c}_+ + c_+\dot{s}_+ \\ 0 & 0 & s_+\dot{s}_- + c_+\dot{c}_- & 0 & -s_-\dot{c}_- + c_-\dot{s}_- & 0 \\ 0 & 0 & 0 & 0 & 0 & 0 \\ 0 & 0 & s_-\dot{c}_- - c_-\dot{s}_- & 0 & s_+\dot{s}_- + c_+\dot{c}_- & 0 \\ 0 & s_+\dot{c}_+ - c_+\dot{s}_+ & 0 & 0 & 0 & s_+\dot{s}_- + c_+\dot{c}_- \end{pmatrix} =$$

[1] Selecting $b(t)$ along $y$ would lead to the same conclusions.

$$= \frac{3i\hbar\nu}{4\sqrt{2}} y_\sigma \sin\nu t \begin{pmatrix} 0 & 0 & 0 & 0 & 0 & 0 \\ 0 & 0 & 0 & 0 & 0 & \sin^2 2\theta \\ 0 & 0 & 0 & 0 & \sin^2 2\theta & 0 \\ 0 & 0 & 0 & 0 & 0 & 0 \\ 0 & 0 & -\sin^2 2\theta & 0 & 0 & 0 \\ 0 & -\sin^2 2\theta & 0 & 0 & 0 & 0 \end{pmatrix} \tag{A.44}$$

where $c_\pm = \cos\theta_\pm$ and $s_\pm = \sin\theta_\pm$.
Thus, in case of deuterium there are two possible $\sigma$ transitions:

$$\begin{aligned} |\,2\,\rangle &\leftrightarrow |\,6\,\rangle \qquad (\Delta F = \pm 1, \Delta m_F = 0) \\ |\,3\,\rangle &\leftrightarrow |\,5\,\rangle \qquad (\Delta F = \pm 1, \Delta m_F = 0) \end{aligned}$$

The effect of the superposition of a time dependent field $b(t) = b_\perp \cos\nu t$ perpendicular to the static one can be analyzed like in the hydrogen case. Neglecting again $\varepsilon_D \ll 1$, one finds:

$$\mathcal{H}_1^\pi = i\frac{E_{HFS}^2}{2} y_\pi \cos\nu t \begin{pmatrix} 0 & -s_+ & 0 & 0 & 0 & -c_- \\ s_+ & 0 & -s_- c_+ & 0 & -c_- c_+ & 0 \\ 0 & s_- c_+ & 0 & -c_- & 0 & -s_- s_+ \\ 0 & 0 & c_- & 0 & -s_- & 0 \\ 0 & c_- c_+ & 0 & s_- & 0 & -s_+ c_- \\ c_+ & 0 & s_- s_+ & 0 & s_+ c_- & 0 \end{pmatrix} \tag{A.45}$$

where again the shortcuts $s_\pm = \sin\theta_\pm$ e $c_\pm = \cos\theta_\pm$ have been applied.
Eight $\pi$ transitions are thus allowed in case of deuterium:

$$\begin{aligned} |\,1\,\rangle &\leftrightarrow |\,2\,\rangle \qquad (\Delta F = 0, \Delta m_F = \pm 1) \\ |\,2\,\rangle &\leftrightarrow |\,3\,\rangle \qquad (\Delta F = 0, \Delta m_F = \pm 1) \\ |\,3\,\rangle &\leftrightarrow |\,4\,\rangle \qquad (\Delta F = 0, \Delta m_F = \pm 1) \\ |\,5\,\rangle &\leftrightarrow |\,6\,\rangle \qquad (\Delta F = 0, \Delta m_F = \pm 1) \\ |\,1\,\rangle &\leftrightarrow |\,6\,\rangle \qquad (\Delta F = \pm 1, \Delta m_F = \pm 1) \\ |\,2\,\rangle &\leftrightarrow |\,5\,\rangle \qquad (\Delta F = \pm 1, \Delta m_F = \pm 1) \\ |\,3\,\rangle &\leftrightarrow |\,6\,\rangle \qquad (\Delta F = \pm 1, \Delta m_F = \pm 1) \\ |\,4\,\rangle &\leftrightarrow |\,5\,\rangle \qquad (\Delta F = \pm 1, \Delta m_F = \pm 1) \end{aligned}$$

The holding field dependence of the deuterium hyperfine transitions is shown in figure A.6.

### A.2.3 Transition probability

If the strength of the time dependent field is small compared to the intensity of the static holding field, then the additional potential can be treated perturbatively. In such a case,

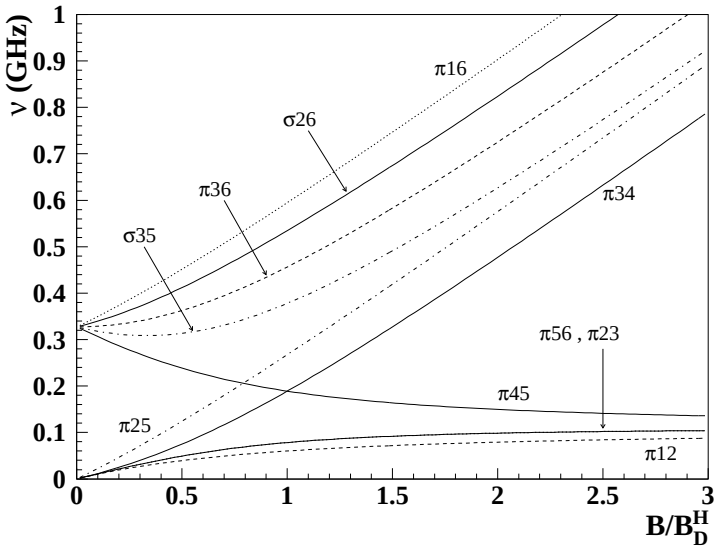


*Figure A.6:*
*Frequencies of deuterium hyperfine transitions plotted as functions of the holding field. The field values are normalized to the critical field $B_D^H$.*

for a fixed interaction time $\tau$, the transition probability between states $|\,a\,\rangle$ and $|\,b\,\rangle$ for an atom is given at the first perturbative order by [2, 3]:

$$W_{ab} \simeq \Big(\frac{y_{\pi,\sigma} E_{HFS}}{\hbar}\Big)^2 |V_{ab}|^2 f(\nu - \nu_{ab}, \tau) \tag{A.46}$$

where the matrix element $V_{ab}$ is defined like

$$V_{ab} = \frac{\langle\, i \,|\, \mathcal{H}_1^{\pi,\sigma} \,|\, n \,\rangle}{\bar{y}_{\pi,\sigma} E_{HFS}} \tag{A.47}$$

with $\bar{y}_{\pi,\sigma} = \frac{b_{(t)}}{B_C}$.
For a periodic field $b(t) = b_{\parallel,\perp} \cos \nu t$, the function $f(\nu - \nu_{ab}, \tau)$ is given by:

$$f(\nu - \nu_{ab}, \tau) = 4 \frac{\sin^2 \frac{(\nu - \nu_{ab})\tau}{2}}{(\nu - \nu_{ab})^2} \tag{A.48}$$

Figure A.7 shows the behavior of (A.48) for a fixed time $\tau$. The function is basically zero outside the range $|\nu - \nu_{ab}| \leq \frac{2\pi}{\tau}$, whereas it reaches its maximum value $\tau^2$ at the *resonance condition*

$$\lim_{\nu \to \nu_{ab}} f(\nu - \nu_{ab}, \tau) = \tau^2 \tag{A.49}$$

If (A.49) holds, the transition probability becomes

$$W_{ab} \simeq \nu_{HFS}^2 y_{\pi,\sigma}^2 |V_{ab}|^2 \tau^2 \tag{A.50}$$

Through the relations $\nu_{HFS} = \frac{E_{HFS}}{\hbar}$, $y_{\pi,\sigma} = \frac{b_{x,y}}{B_C}$ (where $b_{x,y}$ represents the amplitude of the oscillating field) and $B_C = \frac{E_{HFS}}{g_S \mu_B}$, the (A.50) can be written like the following:

$$W_{ab} \simeq \left(\frac{\mu_B}{\hbar}\right) b_{x,y}^2 |V_{ab}|^2 g_S^2 \tau^2 \tag{A.51}$$

One can now conclude that, at the resonance condition, the transition probability between two hyperfine states $|\, a \,\rangle$ and $|\, b \,\rangle$ due to the presence of an oscillating magnetic field depends quadratically on:

- the amplitude of the time dependent oscillating magnetic field;
- the matrix element $|V_{ab}|$, function of the static holding field;
- the time $\tau$ during which the atom experiences the oscillating field.

The quantity $|V_{ab}|^2 g_s^2$ for hydrogen and deuterium hyperfine transitions is shown in figure A.8 as function of the static holding field.

### A.2.4 Adiabatic high frequency transitions

In the last section it has been shown that an atom in hyperfine state $|\, a \,\rangle$ experiencing a periodic magnetic field with frequency $\nu \simeq \nu_{ab}$ can undergo a transition toward the hyperfine state $|\, b \rangle$. If the interaction time $\tau$ is long ($\tau >> \frac{1}{\nu}$), the atom oscillates between the two energy levels with a period $t = \pi/\nu$. It follows that, among an ensemble of atoms, the exchange between two hyperfine states is possible only by fixing the interaction time of each atom, a condition not possible to fulfill within a jet of particle with thermal velocity

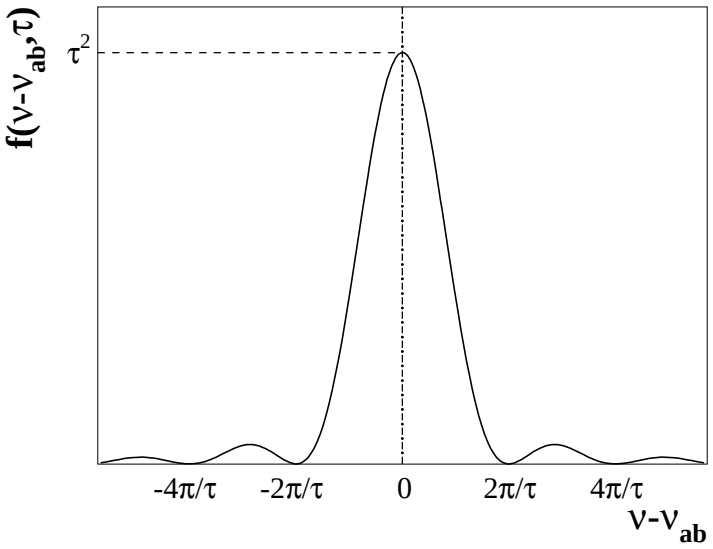


*Figure A.7:*
*The function $f(\nu - \nu_{ab}, \tau)$ at fixed $\tau$. The expression $\nu - \nu_{ab} = \frac{2\pi}{\tau} n$ $(n = \pm 1, \pm 2, ...)$ defines the zeros of the function. At the resonant condition $\nu = \nu_{ab}$, $f(\nu - \nu_{ab}, \tau) = \tau^2$.*

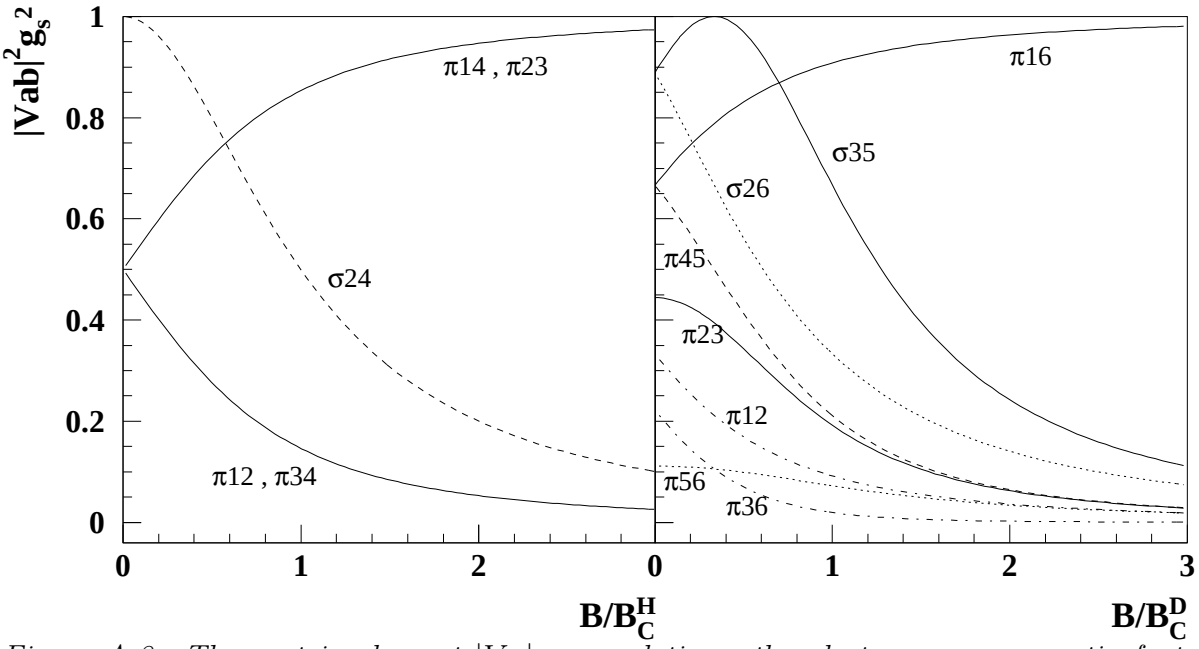


*Figure A.8: The matrix element $|V_{ab}|$ squared times the electron gyro-magnetic factor $g_S$ squared for hydrogen (left) and deuterium hyperfine transitions (transitions $\pi 26$ and $\pi 34$ are not shown because very close to the $\pi 16$ curve). At any given holding field, this quantity expresses the relative probability of the different transitions.*

distribution[2].

An efficient exchange between two hyperfine states can be performed by means of a so-called *adiabatic high frequency transition* (HFT) [4, 5, 6, 7], where a gradient field along the axis of the atomic beam ensures that the resonance condition is met only at one particular position for each atom. A detailed calculation of the adiabatic Hamiltonian and its diagonalization can be found in [27]. With this method, transition efficiencies very close to 100 % can be reached with a resonant region of a few cm length.

Adiabatic high frequency transitions are usually distinguished between strong field transitions (SFTs), with $\Delta m_F = 1$, and medium or weak field transitions (MFTs/WFTs), with $\Delta m_F = 0$ [8, 6, 9, 10]. In order to fill the energy gap between two different Zeeman multiplets, SFTs have to run at frequencies in the order of $\nu_{HFS} = E_{HFS}/2\pi\hbar$ or higher. This condition is usually realized by means of resonator cavities. MFTs/WFTs exchange hyperfine states within the same multiplet, so that the required frequency is approximately proportional to the applied static magnetic field. Therefore, high frequency coils are usually adequate to achieve MFT/WFT transition units.

In order to describe the hyperfine population exchange between two given states $|\,a\,\rangle$ and $|\,b\,\rangle$ undergone by an atomic beam when passing through a HFT, one can use the efficiency

[2]This is the case inside the atomic beam source and the atomic polarimeter of the HERMES target, as it will be shown in chapter 1.

matrix $T_{ab}$:

$$N_a = \sum_b T_{ab} N_b \tag{A.52}$$

where $N_b$ and $N_a$ are the populations vectors $N_i = (N_1, N_2, ...)^T$ before and after the HFT.
In case of a transition SFT 2-4 the matrix $T_{24}$ can be written as follows:

$$T_{24} = \begin{pmatrix} 1 & 0 & 0 & 0 \\ 0 & 1-\varepsilon_{42} & 0 & \varepsilon_{42} \\ 0 & 0 & 1 & 0 \\ 0 & \varepsilon_{24} & 0 & 1-\varepsilon_{24} \end{pmatrix} \tag{A.53}$$

where $\varepsilon_{24} = \varepsilon_{42}$ is the efficiency of the transition unit.
While SFTs are always single step transitions, MFTs/WFTs are usually employed as multiple transitions. Depending on the strength and gradient of the static field, a MFT/WFT unit can be tuned in order to perform subsequent transitions within the same resonant region[3]. For example, the deuterium transition unit MFT 1-4 with negative gradient can

[3]The difference between the two kind of transitions is that MFTs are operated at higher frequency where it is possible to distinguish and separate each step. On the contrary, WFTs are multi-photon transitions.

| Orientation | $\sigma/\pi$ | Type | $\Delta m_F$ | $\Delta F$ | $\Delta m_I$ | $\Delta m_S$ | Hydrogen | Deuterium |
|---|---|---|---|---|---|---|---|---|
| $B(t)\|B^{st}$ | $\sigma$ | SFT | 0 | $\pm1$ | $\pm1$ | $\pm1$ | $2 \leftrightarrow 4$ | $2 \leftrightarrow 6$ |
| $B(t)\|B^{st}$ | $\sigma$ | SFT | 0 | $\pm1$ | $\pm1$ | $\pm1$ | | $3 \leftrightarrow 5$ |
| $B(t)\perp B^{st}$ | $\pi$ | SFT | $\pm1$ | $\pm1$ | 0 | $\pm1$ | $1 \leftrightarrow 4$ | $1 \leftrightarrow 6$ |
| $B(t)\perp B^{st}$ | $\pi$ | SFT | $\pm1$ | $\pm1$ | 0 | $\pm1$ | | $2 \leftrightarrow 5$ |
| $B(t)\perp B^{st}$ | $\pi$ | SFT | $\pm1$ | $\pm1$ | $\pm2$ | $\pm1$ | | $3 \leftrightarrow 6$ |
| $B(t)\perp B^{st}$ | $\pi$ | SFT | $\pm1$ | $\pm1$ | $\pm1$ | 0 | $3 \leftrightarrow 4$ | $4 \leftrightarrow 5$ |
| $B(t)\perp B^{st}$ | $\pi$ | MFT | $\pm1$ | 0 | $\pm1$ | 0 | $1 \leftrightarrow 2$ | $1 \leftrightarrow 2$ |
| $B(t)\perp B^{st}$ | $\pi$ | MFT | $\pm1$ | 0 | $\pm1$ | 0 | | $2 \leftrightarrow 3$ |
| $B(t)\perp B^{st}$ | $\pi$ | MFT | $\pm1$ | 0 | $\pm1$ | 0 | | $5 \leftrightarrow 6$ |
| $B(t)\perp B^{st}$ | $\pi$ | MFT | $\pm1$ | 0 | 0 | $\pm1$ | $2 \leftrightarrow 3$ | |
| $B(t)\perp B^{st}$ | $\pi$ | MFT | $\pm1$ | 0 | 0 | $\pm1$ | | $3 \leftrightarrow 4$ |

*Table A.1: Hyperfine transitions of hydrogen and deuterium and their features. The values $\Delta m_I$ and $\Delta m_S$ are valid in the high holding field regime, where the eigenstates of the static Hamiltonian can be approximated by (A.3) for hydrogen and (A.21) for deuterium.*

be represented, in the ideal case of 100 % efficiency, in the following way:

$$\begin{pmatrix} N_1 \\ N_2 \\ N_3 \\ N_4 \\ N_5 \\ N_6 \end{pmatrix} \xrightarrow{1\leftrightarrow 2} \begin{pmatrix} N_2 \\ N_1 \\ N_3 \\ N_4 \\ N_5 \\ N_6 \end{pmatrix} \xrightarrow{2\leftrightarrow 3} \begin{pmatrix} N_2 \\ N_3 \\ N_1 \\ N_4 \\ N_5 \\ N_6 \end{pmatrix} \xrightarrow{3\leftrightarrow 4} \begin{pmatrix} N_2 \\ N_3 \\ N_4 \\ N_1 \\ N_5 \\ N_6 \end{pmatrix} \tag{A.54}$$

The result does not correspond to the population exchange of states $|\,1\,\rangle$ and $|\,4\,\rangle$, but rather to the rotation of the first four states[4].
The efficiency matrix of a multi step transition unit can be described by the product of the single transitions matrices. In case of the MFT 1-4 with negative gradient one has:

$$T_{14}^{neg} = T_{34}T_{23}T_{12} \tag{A.55}$$

In table A.1 all the possible single step hyperfine transitions for the hydrogen and deuterium cases are summarized.

## A.3 Spin separation in permanent sextupole magnets

An atom with a magnetic dipole moment passing through a magnetic gradient field undergoes the Stern-Gerlach force [11]. Moreover, in case of hydrogen or deuterium, the hyperfine eigenenrgies are modified by the presence of the field as discussed in section A.1. The Lagrange function for an atom in hyperfine state $|\,a\,\rangle$ is then given by:

$$\mathcal{L} = \frac{m}{2}(\dot{x}^2 + \dot{y}^2 + \dot{z}^2) - E_{|\,a\,\rangle}(|\mathbf{B}|) \tag{A.56}$$

In case of a permanent sextupole magnet, the field strength presents a radial quadratimathcal dependence [40]:

$$B(r) = B_{\rho t}\Big(\frac{r}{r_{\rho t}}\Big)^2 \tag{A.57}$$

with the radius $r = \sqrt{x^2 + y^2}$ and $B_{\rho t}$ given by

$$B_{\rho t} = \frac{3}{2}\frac{J \cdot \sin(4\pi\varepsilon/M)}{4\pi\varepsilon/M}\Big(1 - \frac{r_{\rho t}^2}{r_o}\Big) \tag{A.58}$$

being $J$ the magnetization of the sextupole material, $M$ the number of segments, $r_o$ the outer and $r_{\rho t}$ the inner radius of the magnet, while the *filling factor* $\varepsilon$ describes the relative amount of magnetized material in the magnet ($0 < \varepsilon < 1$).

[4]By choosing a positive gradient one would obtain a rotation in the opposite direction.

Thus, the equations of motion can be written as

$$m\,\ddot{x} = -\mu_{|\,a\,\rangle}\frac{2B_{\rho t}}{r_{\rho t}^2}x \tag{A.59}$$

$$m\,\ddot{y} = -\mu_{|\,a\,\rangle}\frac{2B_{\rho t}}{r_{\rho t}^2}y \tag{A.60}$$

$$m\,\ddot{z} = 0 \tag{A.61}$$

where $\mu_{|\,a\,\rangle}$ is the magnetic moment of the atom in hyperfine state $|\,a\,\rangle$ defined by:

$$\mu_{|\,a\,\rangle} = \frac{dE_{|\,a\,\rangle}}{dB} = \frac{dE_{|\,a\,\rangle}}{dx}\frac{1}{B_C} \tag{A.62}$$

and shown in table A.2 for hydrogen and deuterium cases.
Hence, atoms with positive magnetic moment ($m_s = \frac{1}{2}$) are focused toward the axis of the magnet, while atoms with negative magnetic moments ($m_s = -\frac{1}{2}$) are defocused toward the pole tips. Moreover, as the magnetic moments of mixed hyperfine states is field dependent, the intensity the Stern-Gerlach force differs for each state. This difference can be made very small in a high field regime, where the magnetic moments of the mixed states can be approximated to the ones of the correspondent pure state.

| Hydrogen | Deuterium |
|---|---|
| $\mu_1^H = \frac{1}{2}g_s\mu_B$ | $\mu_1^D = \frac{1}{2}g_s\mu_B$ |
| $\mu_2^H = \frac{1}{2}g_s\mu_B\cos(2\theta)$ | $\mu_2^D = \frac{1}{2}g_s\mu_B\cos(2\theta+)$ |
| $\mu_3^H = -\frac{1}{2}g_s\mu_B$ | $\mu_3^D = \frac{1}{2}g_s\mu_B\cos(2\theta-)$ |
| $\mu_4^H = -\frac{1}{2}g_s\mu_B\cos(2\theta)$ | $\mu_4^D = -\frac{1}{2}g_s\mu_B$ |
| | $\mu_5^D = -\frac{1}{2}g_s\mu_B\cos(2\theta-)$ |
| | $\mu_6^D = -\frac{1}{2}g_s\mu_B\cos(2\theta+)$ |

*Table A.2:*
*Magnetic moments of hydrogen and deuterium hyperfine states. During the calculation, the eigenenergies (A.14) and (A.28) have been approximated by setting* $\varepsilon_H \simeq \varepsilon_D \simeq 0$.

# Acknowledgments

I had the honor to present, for the last time, data collected in more than 10 years of polarized target at HERMES. I had the opportunity to use a complex device, such the HERMES target is, with almost no problem to perform a measurement never done, in that region of temperature, on the spin - exchange collision cross - section. For this I should thanks a lot of people that I never met but that worked hardly to design, build up and running the HERMES target, and in these cases all the thanks go to their bosses, professors P. F. Dalpiaz and E. Steffens.
When I arrived in Hamburg I found a very special person that introduce me to the secret of the HERMES target. Think to Davide as a colleague is restrictive, we shared the office for two years, we shared the free week - end, we shared the problems of the target and mostly we shared a lot of gossip!
To spend two years in a foreign country you need mostly two thinks: money and friends. I have to thanks all Ferrara group that was always able to arrange "something" for me, in particular Peppone and Paolo. From the other point of view, it will be not easy forget the first time that I discovered the DOM, the Italian dinners, the gastronomy challenges organized by region and all the social discovery that we did together (nocino with the Notkestrasse walnut, the jet water propulsion racket, the first indoor fly of an airship and the distillation of wine). For this I have to thank, Erika, Paolo, Pasquale, Davide, Elisa (when you are not in the Erika's dream!), Lara, Luigi, Marco Contalb e MarcoS.
More than once my mind was under the control of Riccardo and for this I spent many hour in Reeperbahn, where he showed my another face of Hamburg. Togheter with Bob, Devis, Freddy, Yves and Pat we try to have some distraction by the oppressive and complex physics world, but then I met Rita and after was impossible to drink a pepperoni vodka during a Datscha Party.
Also thanks to my family that, every time that I went home, always remember to me how it is nice the life in Hamburg.

Infine un ringraziamento particolare va ad Adriano, L. Toni, A. Shevchenko, A. Mutu, J. Zanetti (il capitano) la squadra dell'INTER e la FIFA che piu' di una volta mi hanno dato una valida motivazione per andare in ufficio.

# List of Figures

# List of Tables

# Bibliography


[1] D. Fick; Einfuhrung in die Kernphysik mit polarisierten Teilchen, BI-Hochschulskripte Bd. **755a**, Mannheim (1971).

[2] A. Messiah; Quantum Mechanics volume II, North-Holland Publishing Company, Amsterdam, 1961.

[3] C. Cohen-Tannoudji, B. Diu, F. Laloe; Quantum Mechanics, Wiley-Interscience Publication (1977)

[4] A. Abragam, J. M. Winter; *Phys. Rev. Lett. Vol 1*, **10 (1958)**, 374.

[5] W. Haeberli; *Ann. Rev. Nucl. Sci.*, **17 (1967)**, 373.

[6] S. Oh; *Instrum. and Meth. A*,**82 (1970)**, 189

[7] R. J. Philpott; *Nucl. Instrum. and Meth. A*, **259 (1987)**,317.

[8] U. Holm, H. Ebinghaus; *Nucl. Instrum. and Meth.*, **95 (1971)**, 39.

[9] W. Drewes *et al.; Phys Rev. Lett.*, **50 (1983)**, 1759

[10] A. D. Roberts *et al.; Nucl. Instrum and Meth. A*, **322 (1992)**, 6.

[11] W. Gerlach, O. Stern; *Z. Physik*, **8 (1921)**, 110.

[12] HERMES Technical Design Report, DESY-PRC 93/06, 1993.

[13] K. Rith; *Progr. Part. Nucl. Phys* **49**, (2002), 245.

[14] A. A. Sokolov and I. M. Ternov, *Sov. Phys*, Doklady 8 (1964), 1203.

[15] D. P. Barber et al., Phys. Lett. B 343 (1995), 436.

[16] K. Ackerstaff et al.; *Nucl. Instr. Meth. A* **417**, (1998) 230.

[17] E. Steffens and W. Haeberli *Rep. Prog. Phys.* **66**, (2003) 1887.

[18] D. De Schepper et al.; *Nucl. Instrum Meth. A* **419**, (1998) 16.

[19] A. Nass, et al.; *Nucl. Inst. and Meth. A* **505**, (2003) 633.

[20] C. Baumgarten, et al.; *Nucl. Inst. and Meth. A* **496**, (2003) 277.

[21] C. Baumgarten, et al., *Nucl. Inst. and Meth A* **508**, (2003) 268.

[22] C. Baumgarten et al.; *Nucl. Inst. and Meth. A* **482**, (2002) 606.

[23] C. Baumgarten, et al.; *Nucl. Inst. and Meth A* **496**, (2003) 263.

[24] K. Ackerstaff, et al.; *Phys. Rev. Lett.* **82**, (1999) 1164.

[25] A. Airapetian et al., *Eur. Phys. J. D.* **29**, (2004) 21.

[26] C. Baumgarten et al.; *Eur. Phys. J. D* **18**, (2002) 37.

[27] C. Baumgarten, Ph. D. Thesis, University of Munich, Germany, DESY-THESIS-2000-038 (2000).

[28] B. Braun, Ph. D. Thesis, University of Munich, Germany, MPI H - V 25 - 1995 (1995).

[29] M. Dueren; A Luminosity Monitor for the HERMES Experiment, DESY-HERMES 5/90.

[30] T. Benisch; Diploma Thesis, Friedrich-Alexander-Universitaet Erlangen-Nuernberg, 1994.

[31] T. Benisch; Ph.D. Thesis, Friedrich-Alexander-Universitaet Erlangen-Nuernberg, 1998.

[32] C. Weiskopf; Diploma Thesis, Friedrich-Alexander-Universitaet Erlangen-Nuernberg, 1998.

[33] S. Potashov; HERMES Internal Report 31, 1998.

[34] G. E. Thomas et al.; *Nucl.Instrum. and Meth. A* **257**, (1987) 32.

[35] M. A. Bouchiat; *J. Phys. Radium***24**, (1963) 379.

[36] M. A. Bouchiat; *J. Phys. Radium***24**, (1963) 611.

[37] M. A. Bouchiat and J. Brossel; *Phys. Rev.***147**, (1965) 41.

[38] P. W. Anderson in *Magnetism vol. I*; G. T. Radio and H. Suhl (Edts.); Academic Press N. Y. (1963).

[39] N. Koch and E. Steffens *Rev. Sci. Instrum.* **70**, (1999) 1631.

[40] K. Halbach *Nucl.Instrum. and Meth. A* **169**, (1980) 213.

[41] D.Reggiani, Ph. D. thesis, University of Ferrara, Italy, DESY-THESIS-2003-001 (2003).

[42] S. Holloway; *Surf. Sci.***299/300**, (1994) 656.

[43] T. Engel and G. Ertl; *J. Chem. Phys.***69**, (1978) 1267.

[44] H. Conrad, G. Ertl and J. Küppers; *Surf. Sci.* **76**, (1978) 323.

[45] E. W. Kuipers et al.; *Phys. Rev. Lett.***66**, (1991) 116.

[46] C. T. Rettner; *Phys. Rev. Lett.***69**, (1992) 383.

[47] B. Braun Ph. D thesis MPIH - V25, Ludwig Maximilians-University, Munich, Germany (1995).

[48] J. S. Price and W. Haeberli; *Nucl. Instr. Meth. A***326**, (1993) 416.

[49] J. S. Price and W. Haeberli; *Nucl. Instr. Meth. A***349**, (1994) 321.

[50] H. Kolster Ph. D. thesis, Ludwig Maximilians-University, Munich, Germany (1998).

[51] J. F. J. van den Brand et al.; *Phys. Rev. Lett.* **78**, (1997) 1235.

[52] T. Wise et al.; *Phys. Rev. Lett.* **87**, (2001) 042701.

[53] A. Airapetian et al.; *Phys. Lett. B* **442**, (1998) 484.

[54] C. Weiskopf, Proceedings of the IX International Conference on Deep Inelastic Scattering and QCD (DIS 2001), Bologna - Italy, 2001.

[55] M. Contalbrigo, Proceedings of XV International Spin Physics Symposium (SPIN 2002), Brookhaven National Laboratory - NY (USA), 2002

[56] K. Ackerstaff et al., *Phys. Lett. B* **464**, (1999) 123.

[57] A. Airapetian et al., *Phys. Rev. Lett.* **92**, (2004) 012005.

[58] A. Airapetian et al., *Phys. Rev. Lett.* **84**, (2000) 4047.

[59] A. Airapetian et al., *Phys. Rev. B.* **562**, (2003) 182.

[60] R. Seidl, Proceedings of the XII International Conference on Deep Inelastic Scattering and QCD (DIS 2004), Strbske Pleso - Slovakia, 2004.

[61] A. Airapetian et al., *Phys. Rev. Lett.* **84**, (2000) 2584.

[62] M. Henock; *The average HERMES target density in 2000*, **Internal Report 02-029**, 2002

[63] N. F. Mott and H. S. W. Massey; *The theory of atomic collision*, **Oxford at the clarendon press**, 1949

[64] A. Dalgarno and M. R. H. Rudge; *Proc. Roy. Soc.*, **A286 (1965)**, 519.

[65] H. S. W. Massey and C. B. O. Mohr; *Proc. Roy. Soc*, **A144 (1934)**, 188.

[66] E. M. Purcell and G.B. Fields; *Astrophys. J.***124**, (1956) 542.

[67] J. O. Hirschefelder, C. F. Curtiss, R. B. Bird; *Molecular Theory of Gases and Liquids*, **New york: John Wiley & Sons**, 1954.

[68] A. C. Allison *Phys. Rev. A***5**, (1972) 2695.

[69] W. Kołos and L. Wolniewicz, *J. Chem. Phys.***43**, (1965) 2429.

[70] D. R. Swenson, D. Tupa and L. W. Anderson; *J. Phys. B: At. Mol. Phys.*, **18 (1995)**, 4433.

[71] T. E. Sharp, *At. Data***2**, (1971) 119-69.

[72] J. P. Wittke and R. H. Dicke; *Phys. Rev.*, **103 (1956)**, 620.

[73] M. Desainfuscien and C. Auodoin; *Phys. Rev. A***13**, (1976) 2070.

[74] R. J. Knize, Z. Wu and W. Happer; *Adv. in At and Mol Phys.*, Vol. 24; Acedemic Press N. Y. (1991)

[75] M. Desaintfuscien and C. Audoin; *Phys. Rev.*, **A13 (1976)**, 2070.

[76] A. Roth; *Vacuum Technology*, **Amsterdam Horth-Holland**, 1990.

[77] J. F. O'Hanlon; *A user's guide to vacuum technology*, **John Wiley & Sons**, 1989.

[78] R. Kersevan; *Molfflow User's Guide*, **Sincrotrone di Trieste ST/M-91/17**, 1991.

[79] D. H. Davis; *J. Appl. Phy.*, **31 (1960)**, 1169.